Product state distribution and reaction dynamics of $O(^1D) + N_2O \rightarrow NO + NO$

by

Shinnosuke Kawai

Submitted to the Department of Chemistry

in Partial Fulfillment of the Requirements

for the Degree of Doctor of Science

at

Kyoto University

December, 2005

Contents

Chapter 1

Introduction

It is natural for human beings to hold an interest in things surrounding us and seek for understanding of what is going on in this world. In ancient times, this question attracted Greek philosophers[1] such as Thales, Anaximenes, Pythagoras, Heraclitus, Parmenides, Empedocles, *etc.* Among them, Democritus and his successor Epicurus arrived in the notion of *atom*, which was the unit of the world and could not be divided into smaller parts. Whereas their notion was only a philosophically invented idea, it was brought into modern natural science by Dalton in order to explain experimental results of gas-phase chemical reactions in the early 19th century. Dalton's theory of atoms was successively modified by Avogadro, who introduced the concept of *molecule*, which consists of atoms and is the smallest unit of compounds. The theory of atoms and molecules was further pursued through the research of the kinetic theory of gas, the Brownian motion, *etc.* In the early 20th century, it was discovered that the atom is in fact not an undivided particle, but consists of smaller particles called nucleus and electron. Then the birth of quantum mechanics[2] revealed the structure of the atom and the rules governing their behaviors. Since then, all the phenomena of the atomic and molecular levels have become an application of the Schrödinger's equation,[2] and the Hamiltonian equation of motion[3] as its classical approximation. Simply put, the motion of electrons and hydrogen nuclei experiences a large amount of quantum effect whereas that of the nuclei in the second and lower rows of the periodic table can well be approximated by classical mechanics.

The establishment of the fundamental rules might appear a final solution of the atomic and molecular problems. Indeed, calculations based on quantum mechanics have now complete accuracy in reproducing experimental results of simple chemical reactions such as $H + H_2$.[4,5] However, there are two things we must keep in mind.

First, the Schrödinger's equation is analytically solvable only for simple systems such as one-dimensional oscillator, the hydrogen atom, *etc.* The three-body problem has no exact

solution neither classically nor quantum mechanically. In contrast, even simplest systems of chemical interest often contain tens of electrons and three or more nuclei. Therefore, only approximate calculation is available for such systems and the quality of the approximation must be tested by comparing the result with experiment. In the experimental viewpoint, the dynamics of gas-phase chemical reactions have been studied mainly through the rovibrational and angular distribution of reaction products, because the motion of the reaction products reflects the motion during the reaction. Compared to the intermediate stage of the reaction, which is often difficult to detect directly, the reaction product can be more easily detected before the following collision with another molecule, because under a 100 mTorr background pressure the typical time scale between collisions is the order of 100 ns, which is accessible with the time resolution of today's laser technology. Examples of the study of product state distributions can be found in textbooks.[6,7]

Second and more important, *understanding* is something far beyond the mere reproduction of the nature. It aims for the extraction of the essential part of the natural phenomenon and the elucidation of what is really effective in giving rise to such phenomenon. For example, Polanyi[8] examined the effect of the barrier localtion in the model three-atomic reaction

$$\mathrm{A} + \mathrm{BC} \rightarrow \mathrm{AB} + \mathrm{C}. \tag{1.1}$$

Regarding the reaction process as a three-body motion of nuclei with the potential energy given by the expression of London-Eyring-Polanyi-Sato potential,[9] he simulated numerically the trajectories of the reaction. He found that, if the barrier is in the entrance region of the reaction, the translational energy of A is effective for causing the reaction to occur and the energy is largely distributed into the vibration of AB in the product. On the other hand, if the barrier is located in the exit region, the vibration of BC is effective in causing the reaction and the energy is distributed in the translation of the product. It is such kind of explanation that the scientific research should aim for.

Compared to the reaction with a barrier, little is known of the reaction system with a well on the potential energy surface (PES). Wolfrum[10] made a benchmark research by simulating the reaction of O atom with CN molecule:

$$\mathrm{O}(^3\mathrm{P}) + \mathrm{CN}(\mathrm{X}^2\Sigma^+) \rightarrow \mathrm{CO}(\mathrm{X}^1\Sigma^+) + \mathrm{N}(^4\mathrm{S}), \tag{1.2}$$

$$\rightarrow \mathrm{CO}(\mathrm{X}^1\Sigma^+) + \mathrm{N}(^2\mathrm{D}). \tag{1.3}$$

This reaction system has two potential energy surfaces corresponding to two electronic states. One ($^2\Sigma^-$) correlates with the electronic ground state $\mathrm{X}^2\Pi$ of the NCO radical and leads to the

production of the electronically excited nitrogen atom N(^{2}D). The region of NCO intermediate forms a deep well on the PES. The other surface ($^4\Sigma^-$) connects the reactant directly to the ground state of the nitrogen atom N(^{4}S). This surface makes a simply exothermic reaction without a barrier or a well. For the surface with a deep well, the intermediate complex NCO was formed in the course of the reaction and the system was trapped for a long time in the well. The vibrational distribution of the product CO molecule decreased as the vibrational quantum number v' increased. This result can be interpreted that the trapping for a long time period enabled energy randomization and resulted in a statistical trend of the product distribution. On the other hand, the direct-type surface resulted in highly excited vibration of CO with an inverted distribution. The interpretation can be provided in a similar way; if there is no significant well on the PES, the lifetime of the intermediate is likely to be short and the energy is distributed in only a part of the rovibrational modes of the products. Since then, the concept that the product state distribution is closely related to the stability of the reaction intermediate, that is, the depth of the well, has been generally accepted in the study of the reaction with a well. However, contradictory experimental results were found for a four-atomic reaction system.

Suppose a reaction involving four atoms:

$$\mathrm{A} + \mathrm{BCD} \rightarrow \mathrm{AB} + \mathrm{CD}. \tag{1.4}$$

In the process, one chemical bond (B-C) dissociates and one (A-B) is newly formed through the reaction. In the meantime, one bond (C-D) exists both in the reactant and in the product. The atoms C and D remain connected throughout the reaction process and thus this bond is apparently not involved in the "reaction." Such a bond appears first for four-atomic reaction, whereas in three-atomic reaction [See Eq. (1.1)] there are only a dissociating bond (B-C) and a newly formed bond (A-B). This fact makes a qualitative change in going from the three-atomic to the four-atomic reaction system in addition to the mere quantitative increase of the degrees of freedom. Since the reaction starts with an infinitely large A-B bond length, the available energy can be regarded as initially localized in the vibration of the A-B bond. The energy localized in the new bond (A-B) may or may not be transferred to the C-D bond through the interaction between these two bonds in the course of the reaction. If we follow the argument in the previous paragraph, the excitation of the C-D vibration requires a long lifetime, that is, a deep well in the PES compared to the product. In a reaction without a significant well below the product, the "old" bond C-D is not likely to be excited. Now we test the applicability of this argument with one example of the four-atomic reaction.

The reaction of $O(^1D)$ with N_2O is one of four-atomic reactions.

$$O(^1D) + N_2O \rightarrow NO + NO \qquad \Delta H_f^\circ(0) = -341 \text{ kJ/mol}, \tag{1.5}$$

$$O(^1D) + N_2O \rightarrow N_2 + O_2 \qquad \Delta H_f^\circ(0) = -520 \text{ kJ/mol}. \tag{1.6}$$

The channel (1.5) is known as the major source of stratospheric NO, which is involved in the ozone destruction process.[11,12] Many experimental studies[13–22] have been done by measuring the product state distributions and the vector properties for channel (1.5). The two NO products should be distinguished from the dynamical viewpoint. Hereafter we use prime symbols for this purpose and express the reaction as follows:

$$O(^1D) + NN'O' \rightarrow NO + N'O'. \tag{1.7}$$

The newly formed NO originating from $O(^1D)$ is called a "new" NO and the $N'O'$ which already exists in the reactant N_2O is called an "old" NO. The new NO corresponds to the newly formed molecule AB in Eq. (1.4) and the old NO ($N'O'$) corresponds to the old C-D bonds in the same equation. Akagi *et al.*[17,18] distinguished these two kinds of NO by using isotopically labeled $^{18}O(^1D)$, and measured the individual vibrational state distributions for $v' \leq 17$. The sum of the distribution of the new and old NO products decreased monotonically as the vibrational quantum number increased and was very close to the statistical distribution up to $v' \approx 10$ and became smaller than the statistical one for higher v'. The statistical nature of the vibrational distribution was further confirmed by the measurement with FTIR spectrometer.[16,21] Furthermore, although the vibrational distribution of the new NO is more excited than that of the old NO, the populations of both types of the products in each vibrational level are not significantly different.[17,18] This nearly equal energy partitioning between the two kinds of NO is surprising because neither experiment[23,24] nor calculation[25–29] has found any deeper well for this reaction than the *cis*-planar NO dimer, whose binding energy 8.3 kJ/mol[24] relative to NO + NO is very small compared to the exothermicity of 341 kJ/mol. This result forms a sharp contrast to the $O(^1D) + H_2O$ reaction, whose two types of OH products show entirely different vibrational distributions[30,31] although the reaction is considered to proceed with stable H_2O_2 intermediate.[32]

The vibrational distribution is, however, not enough to describe the whole product state distribution, since the product molecules have also the rotational degrees of freedom. Given the statistical trend of the vibrational distribution explained above, it is of interest to what extent the rotational distribution has a statistical nature. Significant excitation of the NO

products was first suggested by Goldstein *et al.*[33] They observed congested rotational lines in the $\Delta v = 0$ region of the NO A $^2\Sigma^+$–X $^2\Pi$ transition but did not make any quantitative analysis. Tsurumaki *et al.*[19] found that the rotational distribution of NO($v' = 0$) was much more excited and estimated the rotational temperature to be $T_{\rm rot} > 10000$ K, which is also close to the statistical distribution. The near-statistical rotational distribution observed by Tsurumaki *et al.*[19] is also indicative of efficient energy transfer within the intermediate. However, one cannot conclude that the rotational distribution of NO($v' = 0$) is really near-statistical since their measurement is limited to $j' < 50$, which covers only the half of the rotational populations in $v' = 0$ level if the statistical or the Boltzmann distribution continues for all the higher rotational levels. The reason for this limitation is the overlap of the transitions from high-j' levels of (0, 0) band with (1, 1) and (2, 2) bands of the A–X transition. Due to the widely spread rovibrational distribution of NO products, such overlap makes the spectral assignment severely difficult. In Chapter 2 of this thesis, we fully determine the rotational state distributions of NO($v' = 0, 1, 2$) products by measuring the wide range of LIF spectra (up to $j' \approx 100$) and by carefully assigning the large number of rotational lines. We confirm the measurement of Tsurumaki *et al.* in the low rotational levels, and it is found out that the overall trend of each rotational state distribution is close to statistical. However, the distribution decreases more rapidly as j' increases than the statistical distribution in high rotational levels $j' > 80$ for all these vibrational levels.[22]

Calculational work is also essential for the understanding of the system since the experimental information is limited. The validity of the calculation must be tested by comparing it with the experimental results. Once the agreement is obtained between the experiment and the calculation, then the calculation can provide much detailed information on the system. González *et al.*[26] have performed high-level *ab initio* calculations at the stationary points for the $O(^1D) + N_2O$ reaction and obtained the rate constants using transition state theory and quasiclassical trajectory (QCT) calculation on a fitted pseudotriatomic London–Eyring–Polanyi–Sato surface. Although they found relatively good agreement with the experimental results in the rate constants and branching ratios, their *ab initio* calculation was limited to the neighborhoods of the stationary points and was not adequate for dynamical studies on global PES. Takayanagi *et al.*[27–29] constructed a global PES by calculating *ab initio* energies at about 10,000 grid points of planar configuration and fitted them to an analytical form. Using this $^1A'$ ground surface, they performed QCT calculation with zero impact parameter[29] and quantum calculations.[28,34] They found qualitative agreement with the experimental results on vibrational

distribution and branching ratio. They also pointed out the existence of "scrambling" process:

$$O(^1D) + NN'O' \rightarrow NO' + N'O, \tag{1.8}$$

whose contribution was smaller than that of the normal NO channel (1.7) but not negligible. This PES of Takayanagi *et al.* will be involved in the Chapter 3 of this thesis. There, we construct a new global PES function by utilizing a part of Takayanagi *et al.*'s PES. With the PES obtained, we perform QCT calculation and obtain relatively good agreement with the experiment. Then we carry out further analyses with the purpose of clarifying the detailed reaction mechanism. We show that the reaction dynamics is clearly dependent on the initial condition and the reactive trajectories can be classified into four paths. One of the paths, which we call "Path 3," is found to have long lifetime, being trapped in a newly found well, whereas the other paths exhibit short lifetime. Contrary to the general notion, we find that the old NO vibration is highly excited along the short-lifetime paths rather than the long-lifetime one.[35]

The existence of four totally different pathways[35] for this reaction requires a set of separate analyses for each of the four mechanisms, because one general explanation for these four paths appears impossible. In Chapter 4 of this thesis, we select one path as the first step of our research and present a detailed description of that path. That path shows the largest excitation of old NO of the four paths, even though it has the shortest lifetime of the reaction intermediate. Therefore this path forms the clearest contrast to the traditional understanding. We adopt the normal form (NF) theory for analyses of the dynamics of this path. This theory has recently been introduced in molecular science[36–47] in the context of transition state theory. The NF theory is a perturbation theory in classical dynamics. It consists in starting with an integrable Hamiltonian as zeroth order and constructing a canonical transformation of the variables based on Lie transformation[48] to convert the Hamiltonian into a desirable form. It has recently been applied to dynamics in the vicinity of a rank-1 saddle point.[36–47] In harmonic approximation at a rank-1 saddle point, one normal mode direction has an imaginary frequency, which is called a reactive mode. The others have real frequencies, which are called bath modes. It was found that the coupling between the reactive and bath modes can be eliminated by transforming to a new set of coordinates, enabling the extraction of recrossing-free dividing hypersurface (transition state) and the reaction path in phase space which all reactive trajectories necessarily follow. These are based on the concept of the normally hyperbolic invariant manifold (NHIM) and its stable and unstable manifolds. This is due to the fact that the resonance condition, which causes divergence in perturbation expansion through the problem of small divisor, can never be met between real and imaginary frequencies. In Chapter 4, our aim is not only the

elimination of the coupling between the reactive and bath modes, but also the elimination of as many couplings as possible among the bath modes, since we are interested in the motions including the stretching vibrations of the two NO bonds. We wish to simplify the coupling terms as much as possible. Once the number of coupling terms becomes sufficiently small, we investigate the extent and effect of each term. In spite of the high energy, the dynamics of this path is shown to be regular with the normal mode picture well conserved with a small distortion. The energy exchange between the two NO groups is essentially a "beat" between the symmetric and antisymmetric normal modes, rather than chaotic coupling. Through this analysis of Chapter 4, it is shown that the NF process is a powerful tool for the analysis of dynamics, elucidating the coupling terms essential to the dynamics by making the Hamiltonian as simple as possible. With the number of terms significantly reduced, we can assess which coupling(s) play important roles in the dynamics. Thus, starting with the normal mode picture and assessing the effect of anharmonic coupling terms with the NF procedure, we can test whether the normal mode structure is conserved or not, and, if not, elucidate new phase space structures caused by the anharmonic couplings.

The energy partitioning in the reaction can be regarded as a negotiation of two factors: the rate of energy transfer among the vibrational modes of the reaction intermediate and the lifetime of the intermediate. The product state distribution is often argued only in the connection to the lifetime, or the depth of the well. Such argument assumes that the rate of energy transfer is more or less the same order for all the molecular systems. However, this simple consideration often fails to explain the actual observation of the product state distributions. One significant example is the reaction of $O(^1D) + N_2O$ discussed in this thesis. Other examples may be found in $O(^1D) + H_2O$,[30,31] $H + NO_2$,[49–51] $O(^1D) + HCl$,[52–54] for which the PES have deep wells but the product state distributions deviate significantly from the statistical trend. Therefore, more detailed consideration of the rate and then the mechanism of the energy transfer is necessary for the understanding of these processes. We suggest that there are two possible mechanisms for the energy transfer within the intermediate. One is energy randomization through chaotic motion, which may close to the traditional picutre of the deep-well case. The other is the motion that experiences only a part of the phase space but has similar projections to all the modes considered. The beat mechanism found in Chapter 4 of this thesis is included in the latter and responsible for the significant excitation of the old bond for, at least one path of, the reaction of $O(^1D) + N_2O$. For the purpose of clarifying the mechanism of the energy partitioning, the NF analysis[55] we introduce in this thesis can be a powerful method. In the future, it would be interesting to analyze other paths of this reaction and also other chemical reactions from this viewpoint.

Chapter 2

Exit interaction effect on nascent product state distribution of $O(^1D) + N_2O \rightarrow NO + NO$

2.1 INTRODUCTION

The reaction of $O(^1D)$ with N_2O has two major channels:

$$O(^1D) + N_2O \rightarrow NO + NO \qquad \Delta H_f^\circ(0) = -341 \text{ kJ/mol}, \tag{2.1}$$

$$O(^1D) + N_2O \rightarrow N_2 + O_2 \qquad \Delta H_f^\circ(0) = -520 \text{ kJ/mol}. \tag{2.2}$$

These two channels can be characterized by large exothermicity[56] and almost gas kinetic rate constants.[57] The branching ratio of the two channels was experimentally determined to be $k_1/k_2 = 1.6$ although there has been no observation which identifies the electronic state of the nascent O_2 products for channel (2.2). Most studies of this reaction were concerned with the channel (2.1) because of the ease of detection of NO products and its importance in atmospheric chemistry as a major source of stratospheric NO.

A peculiar feature of the dynamics of this reaction is the release of the large exothermicity without a deep potential well. For channel (2.1), NO dimer is the known stable species. There are large amount of spectroscopic study on the *cis*-planar dimer and its binding energy was determined to be about 8.5 kJ/mol,[23] which is very small compared to the exothermicity of 341 kJ/mol. *Ab initio* calculations[25–29] found no deeper well than the *cis*-planar ONNO and showed that this channel has almost no barrier. The very shallow well suggests that the lifetime of the intermediate of this reaction is short.

The dynamics of the channel (2.1) has been studied by measuring product state distributions and vector properties,[13–21] mostly based on the laser-induced fluorescence (LIF) technique.

The two NO molecules produced from this reaction should be distinguished from dynamical viewpoint. The newly formed NO originating from O(^{1}D) is called a "new" NO and the other NO which already exists in the reactant N_2O is called an "old" NO. Using isotopically labeled ^{18}O(^{1}D), Akagi *et al.*[17,18] measured the individual vibrational state distributions of the new and old NO products for $v' \leq 17$ in a condition where the nascent rotational distributions are relaxed by collisions after the reaction but vibrational relaxation is negligible. The distribution decreased monotonically as the vibrational quantum number increased and significant populations were found up to $v' \approx 10$. The sum of the distribution of the new and old NO products was very close to the statistical distribution up to $v' \approx 10$ and became smaller than the statistical one for higher v'. The vibrational distributions measured with FTIR spectrometer[16,21] showed better agreement with the statistical one for such high v' levels. Furthermore, although the vibrational distribution of the new NO is more excited than that of the old NO, the populations of both types of the products in each vibrational level are not significantly different.[17,18] This result forms a sharp contrast to the O(^{1}D)+H_2O reaction, whose two types of OH products show entirely different vibrational distributions[30,31] although the reaction is considered to proceed with stable H_2O_2 intermediate.[32] Akagi *et al.* compared the observed vibrational distribution with those for O(^{1}D)+H_2O and S(^{1}D)+N_2O.[58] From the analysis of vibrational couplings, they concluded that the existence of atoms with similar masses induced enhancement of the energy transfer, which compensated the short lifetime of the intermediate.

For rotational distribution, significant excitation of the NO products was first suggested by Goldstein *et al.*[33] They observed congested rotational lines in the $\Delta v = 0$ region of the NO A $^2\Sigma^+$–X $^2\Pi$ transition but did not make any quantitative analysis. As opposed to this observation, Brouard *et al.* reported a cold distribution of NO($v' = 0$) almost identical to a thermal distribution of 300 K.[14,15] They found high rotational excitation for NO($v' \geq 1$) and thus they suggested that NO($v' = 0$) was produced via stripping mechanism whereas NO($v' \geq 1$) was produced through a short-lived complex. On the other hand, Tsurumaki *et al.*[19] found that the rotational distribution of NO($v' = 0$) was much more excited and estimated the rotational temperature to be $T_{\rm rot} > 10000$ K, which is also close to the statistical distribution. They suggested the possibility that the thermalized residual NO contaminated the spectrum in the measurements of Brouard *et al.*[14,15] The near-statistical rotational distribution observed by Tsurumaki *et al.*[19] is also indicative of efficient energy transfer within the intermediate. However, one cannot conclude that the rotational distribution of NO($v' = 0$) is really near-statistical since their measurement is limited to $j' < 50$, which covers only the half of the rotational populations in $v' = 0$ level if the statistical or the Boltzmann distribution continues

for all the higher rotational levels. The reason for this limitation is the overlap of the transitions from high-j' levels of (0, 0) band with (1, 1) and (2, 2) bands of the A–X transition. Due to the widely spread rovibrational distribution of NO products, such overlap makes the spectral assignment severely difficult.

In theoretical works, it is only quite recent that this reaction was treated as a four-atomic system. González *et al.*[26] calculated the potential energies at the stationary points and obtained the rate constants using transition state theory and quasiclassical trajectory (QCT) calculation on a fitted pseudotriatomic London–Eyring–Polanyi–Sato surface. Although they found relatively good agreement with the experimental results in the rate constants and branching ratios, their pseudotriatomic surface was not adequate to calculate the product state distributions. Takayanagi *et al.*[27–29] calculated the potential energies at about 10000 grid points of planar configurations of this system and fitted them to an analytical form. Using this $^1A'$ ground surface, they performed QCT calculation with zero impact parameter[29] and quantum calculations.[28,34] They found qualitative agreement with the experimental results on vibrational distribution and branching ratio. However, the rotational distributions were not calculated.

In this chapter, we have fully determined the rotational state distributions of NO($v' = 0, 1, 2$) products by measuring the wide range of LIF spectra (up to $j' \approx 100$) and by carefully assigning the large number of rotational lines. It is found out that the overall trend of each rotational state distribution is close to statistical. However, the distribution decreases more rapidly as j' increases than the statistical distribution in high rotational levels $j' > 80$ for all these vibrational levels. Furthermore, we carry out QCT calculations on the *ab initio* PES calculated by Takayanagi *et al.* to predict rotational distributions in these vibrational levels. In addition to ordinary QCT calculations, we perform another type of calculation which consists of statistical distribution of the reaction intermediate and usual propagation to the products. This calculation enables us to separately extract the effects of the PES from the reactant to the intermediate and from the intermediate to the product, to provide us with deeper insight into the dynamics. The details of the dynamics of the reaction will be discussed based on the comparison between the experimental and theoretical results, especially in terms of the effect of the exit region from the intermediate to the product of the PES.

2.2 EXPERIMENT

The experiment was performed in flow condition at room temperature. Nitrous oxide (Showa Denko 99.999%) was used without further purification. The sample gas was introduced into

a stainless steel vacuum chamber and pumped with a rotary pump and a mechanical booster pump. The pressure was kept at 200 mTorr by controlling the flow rate with a stainless steel needle valve.

The electronically excited oxygen atom O(^{1}D) was produced from the photodissociation of N_2O with 193 nm light generated by an ArF excimer laser (Lambda Physik EMG 53 MSC). The product NO($v' = 0, 1, 2$) molecules were probed with LIF via the NO A $^2\Sigma^+$–X $^2\Pi$ (0, 0)(0, 1)(0, 2) transitions. To obtain the probe light, a tunable dye laser (Lambda Physik SCANmate 2E) pumped by a XeCl excimer laser (Lambda Physik COMPex 102) was utilized. The wavelength of the probe light was 213–248 nm and it was generated by using the laser dyes Stilbene 3 (213–216 nm, as the doubled output), Coumarin 120 (215–222 nm), Coumarin 2 (220–228 nm), Coumarin 47 (226–239 nm) and Coumarin 102 (239–248 nm) and by frequency doubling their output with BBO I (220–248 nm) and BBO II (213–221 nm) crystals. The delay time between the photolysis and the probe lights was set to be 100 ± 20 ns, which has been proved to be sufficient to neglect the effect of collisional quenching of the nascent distribution.[19] In order to minimize the saturation effect, the intensity of the probe laser light was kept about 7–8 μJ/pulse and the dependence of the LIF signal on the intensity of the probe light was measured in advance. The photolysis and the probe lights were counterpropagated with each other.

The LIF signal was collected by a synthetic silica lens and focused by another silica lens on a photomultiplier tube (Hamamatsu R928) mounted in the direction perpendicular to the laser axis. In order to reduce the strong scattered light and emission arising from the photolysis laser, a long-pass filter (Corning CS9-54) was placed in front of the photomultiplier tube. The detected signal was amplified by a fast preamplifier (Comlinear CLC100) and gated by a boxcar integrator (Stanford Research System SR250). The first 50 ns after the probe laser irradiation was not included in the integration to avoid the scattering of the probe light. The gate width was set to 100 ns in consideration of the fluorescence lifetime. The gated signal was digitized by an A/D converter (Stanford Research System SR245) and stored into a personal computer via a GPIB interface. The intensities of the photolysis and the probe lights were monitored with photodiodes (Hamamatsu 1336-5BQ) to normalize the detected LIF signals. The absolute intensities of the probe laser were also measured with laser power meter (Gentec ED-100A). The experimental system was operated with a repetition rate of 10 Hz.

As reported previously,[19] there exist thermalized residual NO molecules in the reaction chamber. The contribution of the residual NO to the LIF signal is considerable in the low j' levels only for $v' = 0$ level. In order to eliminate this background signal, we altered the

ON/OFF of the photolysis laser shot by shot and subtracted the signal without the photolysis laser from that with the photolysis laser.

Recent study of Adams *et al.* detected a spin-forbidden $N(^4S) + NO$ channel[59] although the yield was not expected to exceed 1%.[60] By examining the dependence of the LIF signal intensity on the delay time, we confirmed the negligible contribution of the photofragment NO, which would arise just after the photolysis.

Since $NO(A\ ^2\Sigma^+)$ is known to predissociate,[61] we checked the time profile of the fluorescence. The LIF signals of 16 rotational levels were recorded in a digital storage oscilloscope (Tektronix TDS30528).

2.3 QUASICLASSICAL TRAJECTORY CALCULATION

In order to understand the origin of observed rotational populations, we have preformed QCT calculations. We used the PES of Takayanagi *et al.*,[27–29] which is an analytically fitted surface of *ab initio* calculations of the lowest $^1A'$ PES. The details of the PES can be found in Refs. 27–29.

The classical equations of motion for the $O(^1D)+N_2O$ collision were numerically integrated by using Bulirsch-Stoer method.[62] Energy conservation up to the order of 0.01 cm^{-1} was confirmed. For the coordinate, three Jacobi vectors were employed; one connects the $O(^1D)$ atom and the center-of-mass(CM) of the N_2O molecule, another connects the terminal N atom and CM of NO moiety in N_2O, and the other connects the N and O atoms of NO in N_2O. Since the *ab initio* calculations were performed only for the planar structure of the $O(^1D)+N_2O$ system, the three Jacobi vectors were confined in two-dimensional (2D) collision plane. The calculated population of each rotational state was multiplied by the degeneracy factor $2j' + 1$ to convert the 2D results to 3D. This conversion is on the assumption that all the $2j' + 1$ states are populated equally. We consider this assumption valid because the anisotropy of the product rotational angular momentum in the CM frame was found to be small[19] and, as will be shown in Sec. 2.4.1, we have found only slight preference for one of the Λ-type doublet components to the other.

To obtain detailed insight into the dynamics, we have carried out two types of calculations. One is the conventional classical scattering calculation, which we call *full-collision* calculation. The other type is named *half-collision* calculations. In the latter calculation, we have assumed a statistical distribution in the reaction intermediate ONNO and then observed the resulting NO state distributions. More precisely, phase space points with fixed distance between the CM's of each NO were randomly sampled and trajectories were propagated en route to the

products. For this sampling, the distance between the CM's of two NO's was chosen equal to the experimentally determined value of NO dimer, *i.e.* 2.263 Å.[63]

For the full-collision calculation, collision energy was sampled according to the distribution of collision energy in the present experimental condition. The distribution was calculated from the convolution of the velocity distribution of $O(^1D)$ and that of thermal N_2O by taking account of the integration of the angle between these two velocity vectors.[64] For the velocity distribution of $O(^1D)$, experimentally determined translational energy distribution for the 193 nm photodissociation of N_2O (Ref. 65) was used. The mean collision energy $\langle E_{\rm col} \rangle$ thus obtained is 52 kJ/mol and the full width at half of maximum of the $E_{\rm col}$ distribution is 38 kJ/mol. The initial rotational energy of N_2O was sampled by classical Boltzmann distribution of 300 K and the vibrational energy was fixed to the zero point energy of the calculated PES. Impact parameters were sampled up to 6 Å, where the opacity function became negligibly small. For the half-collision calculation, the total energy of the system was set equal to the collision energy of $O(^1D)$ and N_2O plus the zero point energy of N_2O. About 200,000 trajectories were run for each of the two types of the calculation.

2.4 RESULTS AND DISCUSSIONS

2.4.1 Experimental results

The entire LIF spectrum measured in this study is exhibited in Fig. 2.1. The spectral regions of vibronic bands are shown with their vibrational quantum numbers. Due to the high excitation of NO products in rotational and vibrational motions, a large number of peaks appeared in the spectrum and some of them overlapped with each other. We carefully assigned all the peaks by using the spectroscopic constants found in Ref. 66. Only those peaks which do not overlap with other peaks were utilized to determine the vibrational and rotational distribution. In Fig. 2.1, peaks from wide range of j' were observed. Hence, in order to properly derive the population from the LIF spectrum, we had to carefully check the experimental conditions and correct the observed signals accordingly.

First, to examine the effect of saturation, we measured the dependence of the LIF signal on the dye laser power. Typical results are shown in Fig. 2.2. It is known that the intensity $I_{\rm LIF}$ of LIF signals is proportional to $P[1 - \exp[-(A + 2B\rho)\Delta t]$ when the rate equation for the two-state model is solved to take into account the saturation effect.[67] Here, P denotes the population in a specific quantum state, A and B are the Einstein coefficients, ρ expresses the radiation density, and Δt is the duration of the laser pulse assumed as rectangular. As shown in

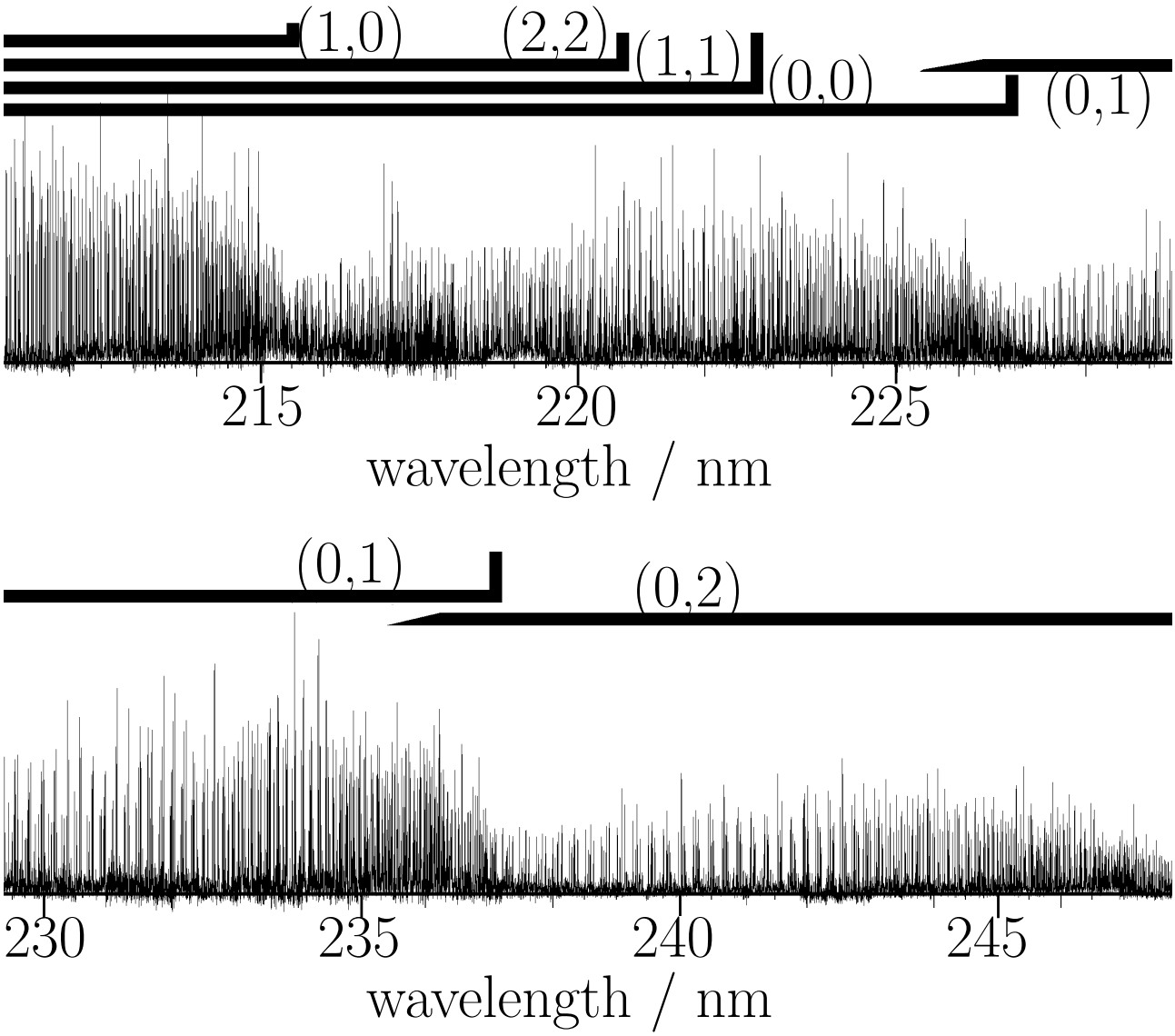

Figure 2.1: Observed LIF spectra of nascent NO($^2\Pi_{1/2,3/2}$). The spectral regions are roughly shown for each vibronic band with upper and lower state vibrational quantum numbers.

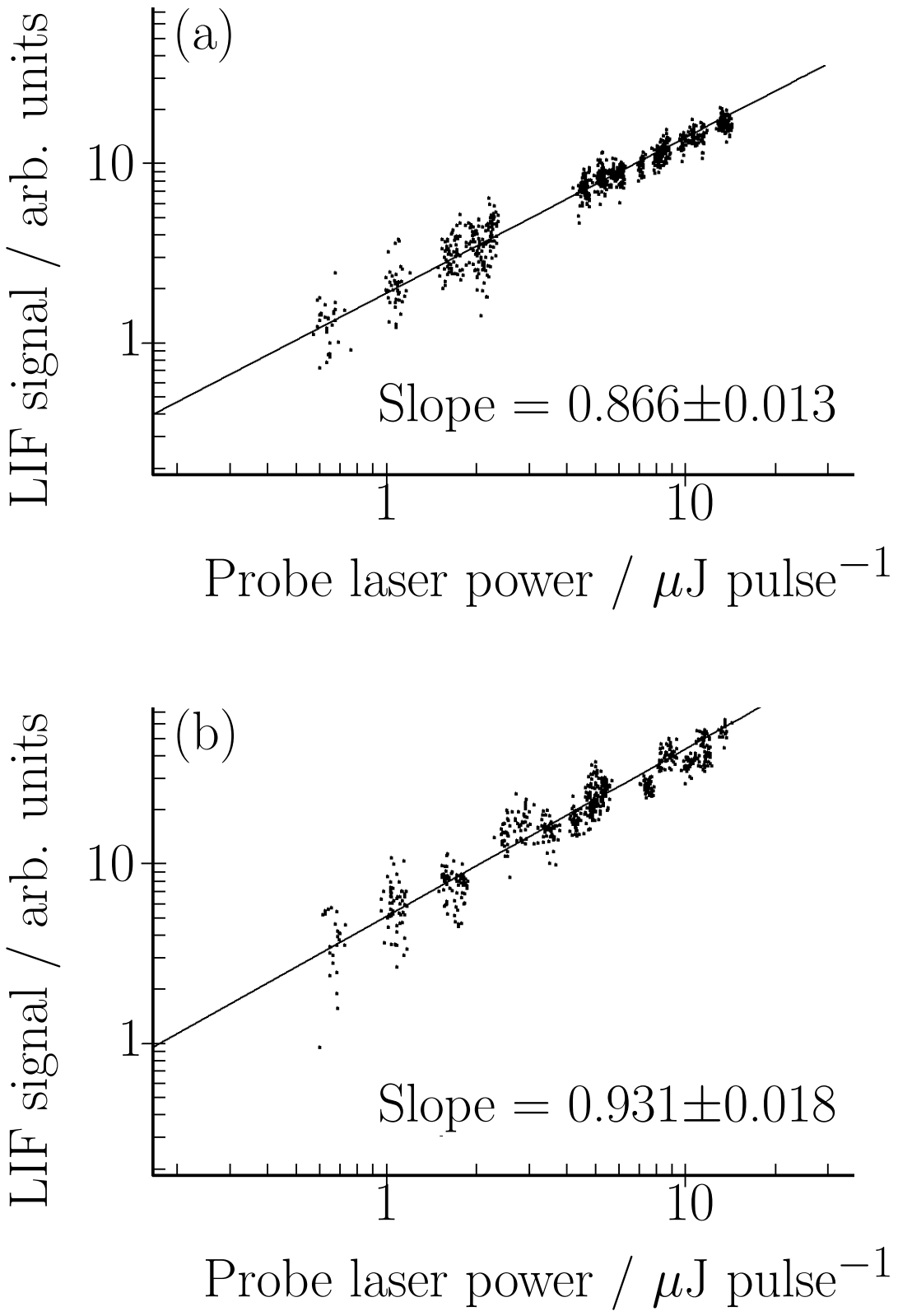

Figure 2.2: Dependence of the LIF signal intensities on the probe dye laser powers measured for (a) $Q_{11}(47.5)$ and (b) $Q_{22}(67.5)$ transitions of A–X(0, 0) band. The solid lines represent the results of least-squares fitting and their slopes are shown.

Fig. 2.2, this expression can be effectively approximated as $C(\rho S)^n P$ and we fitted I_{LIF} to this formula. Here, C and n are fitting parameters, and S denotes the line strength factor. We found n=0.8–1.0 by least-squares fitting and confirmed that the derived distribution did not change significantly in this range of n. We adopted n=0.9 for all the rotational lines to determine the population and Fig. 2.1 shows the spectrum after the correction against the probe laser intensities with this value. To derive rotational distributions, we divided the signal intensity in the spectrum by S^n, where S was calculated by taking into account the Hönl-London factors and the dependence of electronic transition moment on rotational levels.[68] The correction due to the electronic transition moment decreases the line strength factor for $j' \approx 100$ by at most 20% compared to that for $j' \approx 0$.

Second, signal intensity was corrected against the wavelength dependence of the detection efficiency since the difference of the wavelengths of the fluorescence from the low and high rotational levels was significant. We calculated the wavelength dependence of the detection efficiency from the curves of the filter transmission and the photomultiplier sensitivity, which were taken from their catalogs. With thus obtained efficiency curve, the correction factors for the LIF detection was determined by considering Franck-Condon factors[66] and Hönl-London factors. The resulting correction factors for NO(A, $v_{\mathrm{A}} = 0$, j_{A}) are shown in Fig. 2.3. The detection efficiency monotonically decreases with j_{A} and that of $j_{\mathrm{A}} = 0.5$ is 2.5 times higher than that of $j_{\mathrm{A}} \approx 100$.

Third, the rotational state dependence of the predissociation rate should be taken into account. NO (A, v_{A}) is known to predissociate in $v_{\mathrm{A}} > 3$ levels.[61] The threshold energy corresponds to $j_{\mathrm{A}} \approx 65$ for NO(A, $v_{\mathrm{A}} = 0$) although the dissociation rate has not been reported for such high rotational levels. To clarify the appropriate correction factor, we measured the time profiles of the LIF signals from NO(A, $v_{\mathrm{A}} = 0$, j_{A}). The time constants of the fluorescence decay were determined from least-squares fitting analysis of the recorded profiles with the assumption of single exponential decay. Figure 2.4 shows the lifetimes against the upper state rotational quantum number j_{A}. As recognized from the figure, clear dependences on j_{A} are not found although the lifetimes are scattered. Thus, no further correction due to the predissociation was made for determining the populations. Although this dependence is not a central topic of this chapter, it is notable that the effects of the rotational energy and vibrational energy are different for the predissociation of NO(A).

The observed lifetimes ranging from 80 to 100 ns are shorter than the collision-free radiative lifetime of NO(A) *i.e.* 200 ns.[61] This result indicates that the rate constant of electronic quenching is about (200 ns)$^{-1}$ with 200 mTorr of N_2O, which corresponds to $\approx 8 \times 10^{-10}$ cm^3

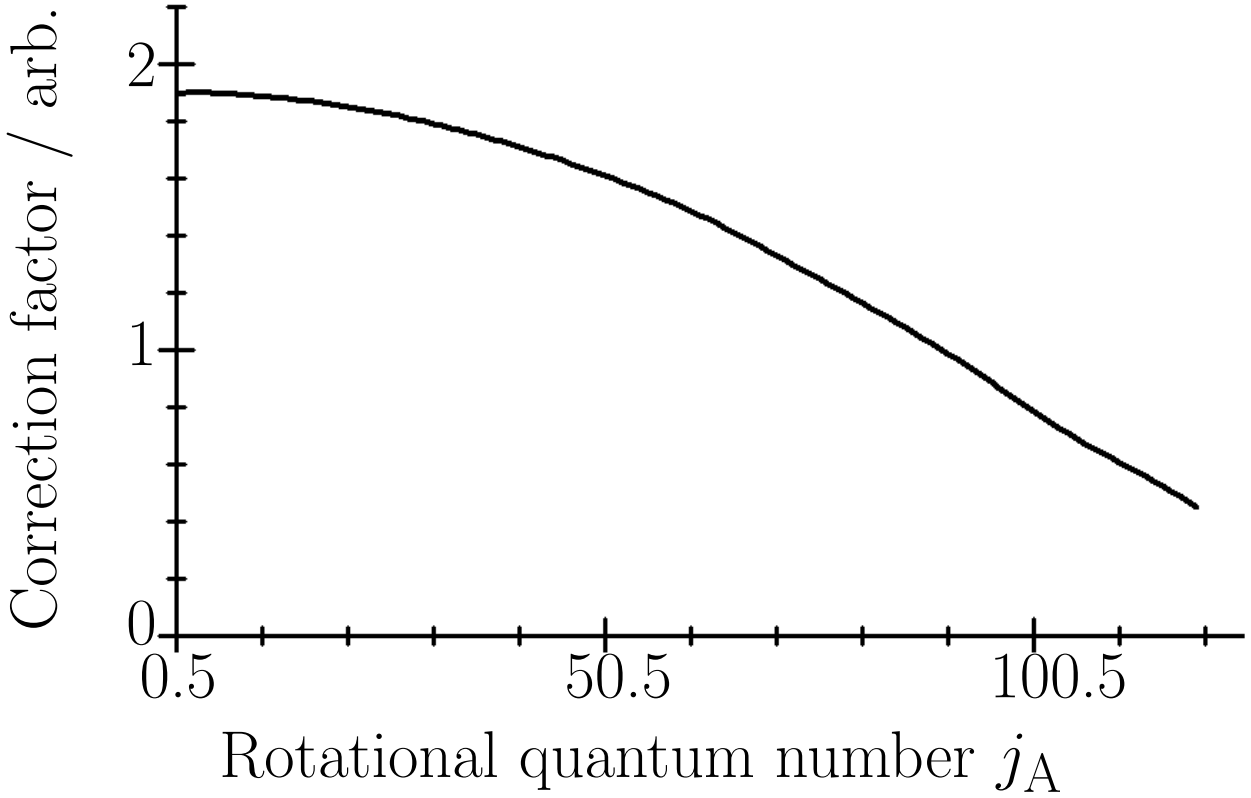

Figure 2.3: Correction factors for the LIF signal whose upper state is NO(A, $v_A = 0$, j_A) calculated from Franck-Condon factors, Hönl-London factors, filter transmission, and photomultiplier sensitivity.

molecule^{-1} s^{-1}. It may imply that the products can suffer collisions in the time scale of our pump-probe delay under the present pressure. However, the known rate constants of rotational relaxation of NO with diatomic and triatomic species[69] are smaller than the electronic quenching rate found here and even if we use this electronic quenching rate as the upper limit of the rotational quenching, at least 80% of NO(X, v', j') products generated during the 100 ns delay time is estimated to be free from collisions before the probe laser irradiation.

Figure 2.5 shows the rotational distributions of NO($v' = 0, 1, 2$) obtained after the corrections described above. The squares and circles in Fig. 2.5 show the rotational populations of each spin-orbit and Λ-type sublevels. For each sublevel, fine irregularities of the population against j' remain even after the averaging of several scans and we do not consider these structures physically meaningful. The populations were derived from the (0, 0), (0, 1) and (0, 2) bands, which cover all the rotational levels plotted in the figure. The validity of the correction procedure is confirmed by the fact that the populations derived from the (1, 0), (1, 1) and (2,

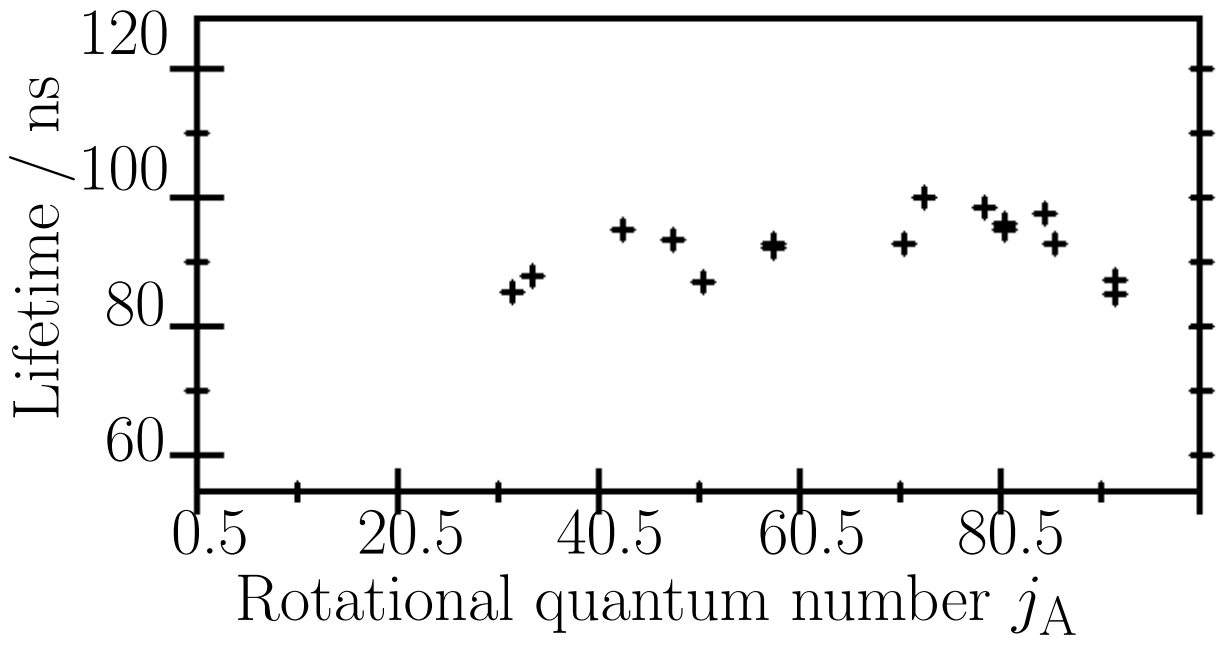

Figure 2.4: Fluorescence lifetime of NO(A $^2\Sigma^+$, $v_A = 0$, j_A) measured with 200 mTorr N_2O. No significant dependence on either j_A or spin-rotation sublevels was found.

2) bands are consistent with those shown in Fig. 2.5. The horizontal bars shown with arrows in the figure indicate the upper limits of the population of those levels for which we could not find any peak at the appropriate wavelengths. These limits were set to the largest undulation of the baseline. Thus the real populations might be lower than these limits. The total population of each vibrational state is normalized to appear in the same area by utilizing the Boltzmann fitting described below. In this study, the new and old NO products are not distinguished by isotopic labeling. The fractions of the old NO in the $v' = 0$, 1, and 2 levels are estimated to be 77%, 62%, and 50%, respectively.[18]

Figure 2.5 shows that the global features of the rotational distributions in the three vibrational levels are similar and broad peaks are located at around $j' \approx 60$. The populations calculated by the phase space theory (PST)[70,71] are also shown by dotted lines. The PST distribution was obtained with the mean collision energy in our experimental condition (52 kJ/mol) and by taking account of the centrifugal barrier in the exit region. In comparison with the PST distribution, the observed distribution can be characterized as follows. The distributions for the levels with low rotational quantum number ($j' < 50$) are well reproduced by the statistical theory. The levels with middle j' ($j' = 50$–80) are more populated than predicted by

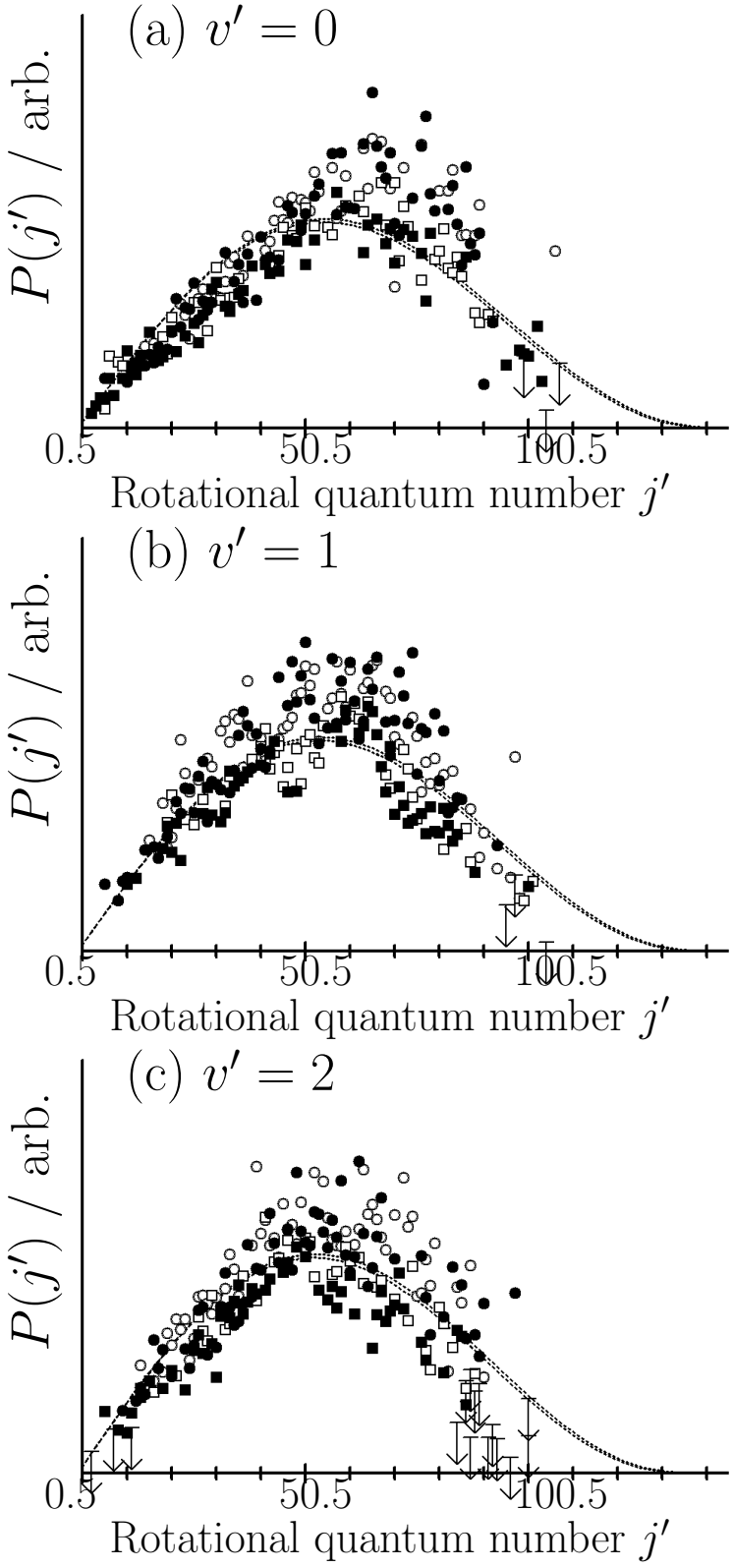

Figure 2.5: Rotational state distributions of NO($v' = 0, 1, 2$). Squares and Circles denote the observed populations (○,$^2\Pi_{1/2}$ A′; □,$^2\Pi_{1/2}$ A″; ●,$^2\Pi_{3/2}$ A′; ■,$^2\Pi_{3/2}$ A″). Downward arrows show upper limits estimated from noise level. Dotted lines are the rotational state distributions of $^2\Pi_{1/2}$ and $^2\Pi_{3/2}$ levels calculated by using PST.

the statistical theory and, in the high-j' region ($j' = 80$–100), the observed populations drops more rapidly as j' increases than the statistical ones. There is no population in $j' > 100$. The statistical distribution for NO($v' = 0$, $j' < 50$) was already observed by Tsurumaki *et al.*[19] However, the extended measurement of this study up to the higher j' levels reveals that the rotational distributions of NO($v' = 0, 1, 2$) gradually deviate from the statistical trend beyond $j' \approx 50$ and completely differ from the PST predictions in the high-j' region (j'=80–100). The possible dynamical reasons for the decrease of high-j' population will be discussed in the rest of the chapter.

Integrated populations and mean values of the observed distributions were calculated from simple analytical functions representing the distributions. Due to the sharp decrease in high-j' region, the distributions cannot be fitted to a single Boltzmann distribution function, nor a linear surprisal. Therefore, to fit the distributions, we adopted an effective functional form: two Boltzmann-type functions switched at a certain value j_c, *i.e.*

$$P(j') = \begin{cases} A_1(2j'+1)\exp(-E_{j'}/k_B T_1) & (j' < j_c) \\ A_2(2j'+1)\exp(-E_{j'}/k_B T_2) & (j' > j_c) \end{cases} \tag{2.3}$$

where $E_{j'}$ is the rotational energy and k_B is the Boltzmann constant. In the least-squares fitting procedure, A_i's and T_i's were determined for a given j_c. As an example, Fig. 2.6 shows the comparison of the observed and the fitted populations of NO ($v' = 0$, $^2\Pi_{3/2}$ A$'$). Note that the form of Eq. (2.3) has no physical meaning related to the reaction dynamics and the fitting parameters A_i's and T_i's are only utilized to find the average of the scattered data and to interpolate the populations of those levels for which isolated rotational lines were not observed.

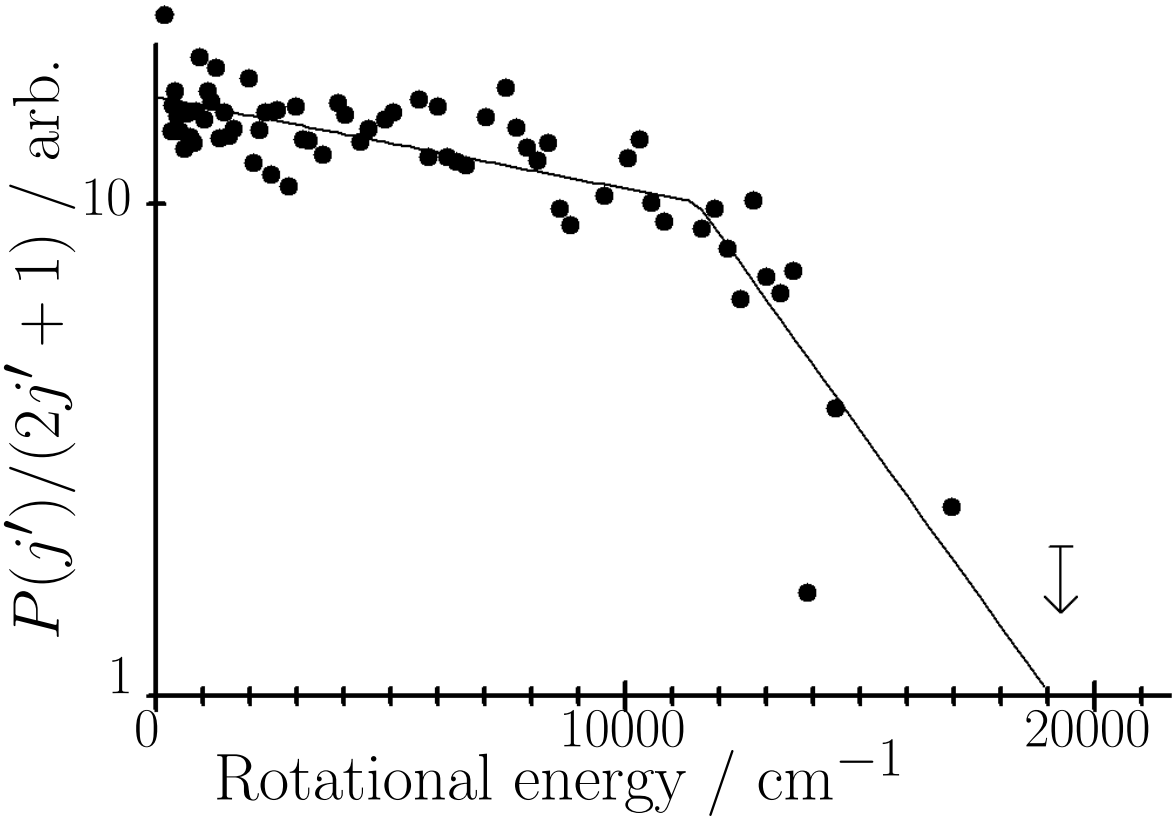

Figure 2.6: Boltzmann plot of the rotational state distributions of NO($v' = 0$, $^2\Pi_{3/2}$ A′). Filled circles denote the observed populations. Solid lines are least-squares fitted lines for the two Boltzmann-type functions switched at j_c (see text).

Table 2.1: Rotational temperatures, mean rotational energies and populations of NO.

	j_c [a]	T_1 / K [a]	T_2 / K [a]	$\langle E_{rot} \rangle$ / cm^{-1}	Population [b]
$v' = 0$, $^2\Pi_{1/2}$ A′	81.5	39000±7900 (10000[c])	11000±15100	8300	0.51
$v' = 0$, $^2\Pi_{1/2}$ A″	76.5	20000±3400	8400±3800	7000	0.40
$v' = 0$, $^2\Pi_{3/2}$ A′	86.5	34000±4400	4700±4600	7100	0.43
$v' = 0$, $^2\Pi_{3/2}$ A″	78.5	20000±1800	7200±3900	7300	0.38
$v' = 0$, total		28000±1900		7500 [7200[d]]	1.73 (1.35[e])
$v' = 1$, $^2\Pi_{1/2}$ A′	69.5	18000±1800	6500±1900	6000	0.28
$v' = 1$, $^2\Pi_{1/2}$ A″	65.5	18000±2800	7900±2900	6100	0.23
$v' = 1$, $^2\Pi_{3/2}$ A′	74.5	19000±1800	6700±2600	6600	0.28
$v' = 1$, $^2\Pi_{3/2}$ A″	66.5	22000±3100	8800±3300	6500	0.22
$v' = 1$, total		20000±1100		6300 (4000[f]) [6900[d]]	1.00
$v' = 2$, $^2\Pi_{1/2}$ A′	74.5	20000±1700	8300±5200	6500	0.22
$v' = 2$, $^2\Pi_{1/2}$ A″	62.5	20000±3700	8100±3100	6200	0.17
$v' = 2$, $^2\Pi_{3/2}$ A′	67.5	23000±3500	13300±6700	7700	0.21
$v' = 2$, $^2\Pi_{3/2}$ A″	67.5	14000±1900	8100±2300	6400	0.16
$v' = 2$, total		20000±1400		6800 [6500[d]]	0.76 (0.64[e], 0.80[g])

[a]The meanings of the fitting parameters are found in text.
[b]Normalized to $v' = 1$ population.
[c]Tsurumaki *et al.*[19]
[d]Calculated by PST
[e]Akagi *et al.*[17,18]
[f]Brouard *et al.*[14,15]
[g]Hancock *et al.*[21]

The results of the fitting are shown in Table 2.1. Using these fitted populations, we were able to determine the mean rotational energies and the vibrational distribution, which are also shown in Table 2.1. The vibrational distribution decreases with vibrational quantum number and the relative population agrees to the previous results shown by Akagi *et al.*[18] although a slight difference can be seen. The ratio of the populations of $v' = 1$ and 2 obtained in this work rather agrees with that obtained by the recent time-resolved FTIR measurement of Hancock *et al.*[21] The observed mean rotational energies are similar to those of PST, which may reflect the global statistical feature of the distribution.

It can be seen in Table 2.1 that the rotational excitation of the NO products found in this study is larger than those observed before. The main rotational temperature T_1=39000 K for NO($v' = 0$, $^2\Pi_{1/2}$ A′) is almost four times as high as the previous value for the same sublevel.[19] Main reason of this difference is that the previous study[19] estimated the rotational temperature as the lower limit rather than the least-squares fitted value since the highest rotational energy of $j' \approx 50$ ($E_{\rm rot} \approx 4000$ cm^{-1}) was insufficient to precisely determine the rotational temperature above 10000 K. Furthermore, the present data set have much better quality than the previous one and the latter scatters around the former. We therefore conclude that the present result is consistent with the previous one and is much more reliable. For NO($v' = 1$), the mean rotational energy is also 1.5 times higher than the previous reports.[14,15] This discrepancy will be attributed to the collisional relaxation or lack of high-j' data in the previous measurement. The mean rotational energies of NO($v' = 1, 2$) obtained in this work are about 1.5 times higher than those estimated as the lower limits under the condition where 50 times more collisions are expected.[21] As described above, the rotational distributions are close to the statistical distribution to some extent and the rotational temperature ≈20000 K is not extraordinarily high compared with the large exothermicity of this reaction.

As for the fine state dependence of the population, the difference between the two Λ-doublet states, Π(A′) and Π(A″), is discernible and a slight preference for Π(A′) can be seen in Table 2.1. As can be recognized from Fig. 2.5, this difference is not so obvious in low j' levels. Little preference for one of the Λ-type doublet components indicates that the motion of the intermediate is not restricted in a plane. This trend is consistent with the observation of the isotropic angular distribution of product rotational angular momentum relative to the scattering plane reported for $j' = 34.5$ by Tsurumaki *et al.*[19] However, the preference for Π(A′) in the high-j' products may indicate the dominance of the in-plane torque to generate highly rotating products. On the other hand, the difference between the two spin-orbit components, F_1 and F_2 levels, is not significant for any j' level.

As recognized from Figs. 2.5 and 2.6, the peculiar feature of the rotational population of all the observed vibrational levels is the sharp decrease of the population in the high-j' region ($j' = 80$–100). The possible factors giving rise to such distribution as an artifact are the predissociation above a threshold level and the neglect of the correction for detection efficiency. Since we carefully inspected such effects and made the proper correction as described above, we conclude that the sharp decrease of the population in the high-j' levels is the genuine one.

2.4.2 Half-collision calculation — modified statistical approach

The observed sharp cutoffs in the product state distribution may invoke the idea that a kinematic effect such as angular momentum conservation or truncation of the impact parameters limits the production of high-j' products. In order to check such effects, we performed the PST calculations with the maximum total angular momenta $J_{\max} = 100$, 220 and 330, where 100 is the minimum value estimated from the experimental rate constant, 220 corresponds to the impact parameter where the opacity function becomes negligible in our full-collision QCT result, and 330 is 1.5 times of that value. The calculated distributions did not change significantly with the maximum total angular momentum. Therefore we can state that the decrease of the high-j' populations is not due to this type of kinematic effect.

We adopted a statistical approach to reproduce the sharp decrease of the population in high-j' levels since the overall trends of the observed rotational distributions were close to those of the PST prediction. In this approach, Statistical Adiabatic Channel Model (SACM),[72] which is a modified version of PST, is a suggestive concept. It is well known that the population of high-j' products calculated by SACM tends to be depressed compared with that calculated by PST.[73] In short, this depression results from the difference of the potential of free products and reaction intermediate. It can be expected that this effect causes the observed sharp decrease in the high-j' products in the $O(^1D)+N_2O$ reaction. However, SACM assumes that the system remains on the same adiabatic potential curve as going from the intermediate to the product, which means that the product molecules need to have sufficiently small velocities. It is questionable whether this condition is satisfied in the $O(^1D)+N_2O$ reaction since the average departure velocity of the product NO is large due to the high exothermicity.[19]

Recently, Larregaray *et al.*[74] combined the statistical assumption for the intermediate and the interactions in the exit potential, to correct the statistical treatment. They analyzed the exit channel dynamics of unimolecular reaction of simple triatomic systems. Once they assumed the statistical ensemble at the transition state, they solved the equations of motion without any adiabatic assumption on an analytically modeled PES with a harmonic potential whose

curvature decreases exponentially with the distance between the products. Their result was that even if the statistical distribution was achieved at the reaction intermediate, the trajectories starting from this statistical intermediate resulted in less high-j' population at the products than the PST prediction. This high-j' depression is generated by the rotation-translation interaction in the exit region of PES. Although the ground for the statistical distribution at the intermediate in our system is not trivial and can be different from that in Larregaray *et al.*'s one, the concept of the exit region interaction modifying the statistical distribution to reduce high-j' populations may be applicable to the present case.

Stimulated by these statistical approaches, we performed a kind of QCT calculation which assumes statistical distribution at the intermediate and propagates the trajectory en route to the products on the *ab initio* surface calculated by Takayanagi *et al.*[27–29] We call this calculation "half-collision QCT calculation." The concept of this calculation may have a lot in common with SACM and Larregaray *et al.*'s work[74] concerning the exit region interaction, but it does not depend on adiabatic assumption or analytical model of the potential. The results of the half-collision calculations are shown by bold lines in Fig. 2.7. In the figure, the observed distributions are averaged for all the four sublevels of $^2\Pi$ states for clarity. The decrease of the high-j' population is well reproduced in the half-collision calculation. This indicates that the interaction in the exit region of PES indeed has an effect of yielding small high-j' populations as is pointed out in Ref. 74.

The effect of high-j' depression due to the exit region interaction can be understood by considering the trajectories in the phase space. Rather than the trajectories propagating from the intermediate to the products, time-reversed trajectories which start from the product NO's and enter into the intermediate are better for describing the exit interaction effect. The use of time-reversed trajectories is certificated by the fact that the classical equations of motion are symmetric with respect to the time reversal. Figure 2.8 schematically represents the phase space of the system where the horizontal axis denotes the distance R between the CM's of two NO moieties and the vertical axis represents the rotational degrees of freedom. Since the free rotational motion of NO's in $R = \infty$ correlates mostly to the bending and torsional vibrations for finite R, certain regions of the phase space are not accessible due to the bending and torsional potential energy which becomes higher as R decreases. Then we see that some of the trajectories are reflected due to this R-dependent vibrational potential. In other words, the product states corresponding to these trajectories cannot be produced by the reaction. If the product states have high rotational energy, the translational energy will be too small to surmount the vibrational potential and hence such trajectories have large probability to

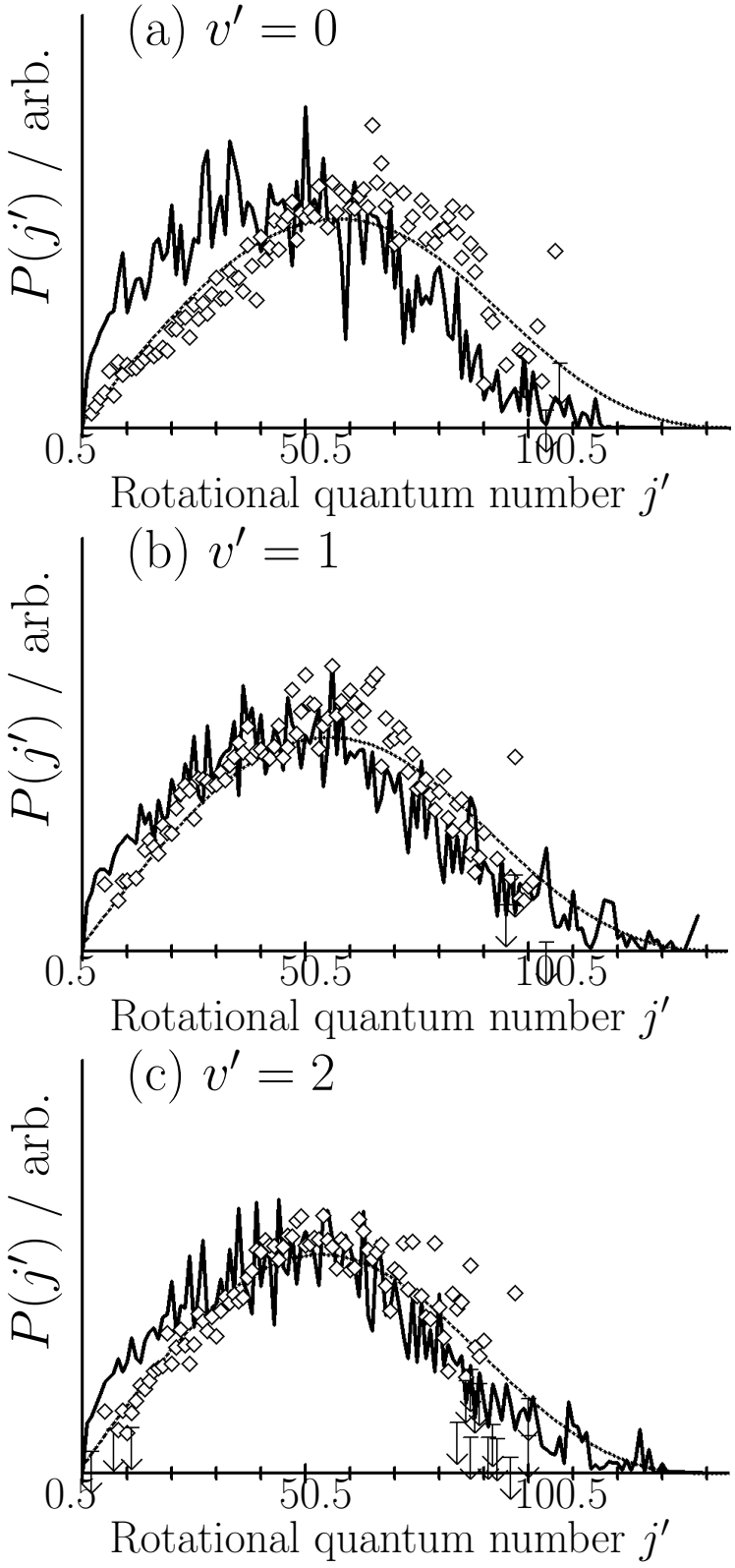

Figure 2.7: Comparison of observed and calculated rotational state distributions of NO($v' = 0, 1, 2$). Squares denote the observed population averaged for all the spin-orbit and Λ-type sublevels. Dotted, bold and dashed lines are calculated distributions of PST, half-collision QCT, and full-collision QCT (see text), respectively.

be reflected. This means that the statistical distribution at the intermediate corresponds to distribution with depressed high-j' populations when propagated to the products.

The essential point for the exit interaction effect of depressing the high-j' populations in the products is the difference between "the statistical distribution of the intermediate" and that of the products. In Fig. 2.8, the accessible region at the intermediate is rounded by dotted lines and that in the product by dashed lines. If the intermediate has the statistical distribution, all the phase space points within the dotted lines are equally populated. On the other hand, the statistical distribution of the products, which is calculated with the PST formalism, populates all the phase space points within the dashed lines. Since there exist reflected trajectories due to the vibrational potential, the statistical distribution at the intermediate does not yield statistical distribution in the products.

Despite the improvement of reproducing the sharp decrease in the half-collision calculation, the calculated distributions are a little biased to the low-j' region compared to the observed ones. This difference can be explained in terms of the following two factors, the accuracy of the PES and the validity of the statistical assumption at the intermediate. If the statistical assumption works well in describing the real distribution of the intermediate, the present PES is inaccurate and overestimates the depression of the rotational excitation of the products in the exit region. On the other hand, if the extent of the depression of the rotational excitation in the exit region of the present PES is correct, the statistical assumption is invalid. In this case, the real distribution of the intermediate is more biased toward the phase space points which produce high-j' products than the statistical one. These phase space points can be regarded as those with high bending and/or torsional vibrations since the NO rotation correlates approximately to the bending and torsional vibrations in the ONNO intermediate.

2.4.3 Reaction dynamics

The validity of the statistical assumption on the current PES can be discussed from the comparison between the results of the half-collision calculation and those of the full-collision calculation. The rotational distributions obtained by the full-collision calculations are shown in Fig. 2.7 as dashed lines. The distributions are too much rotationally excited for all the vibrational levels and the agreement with the experimental result is poor. From the failure of the full-collision calculation, we learn two things. First, the present global PES cannot be considered accurate enough to describe the product state distribution when it is used in full-collision calculations. Second, the reaction intermediate on this PES tends to be too much biased toward the phase space points yielding high-j' products. Although the accuracy of the current PES is not perfect,

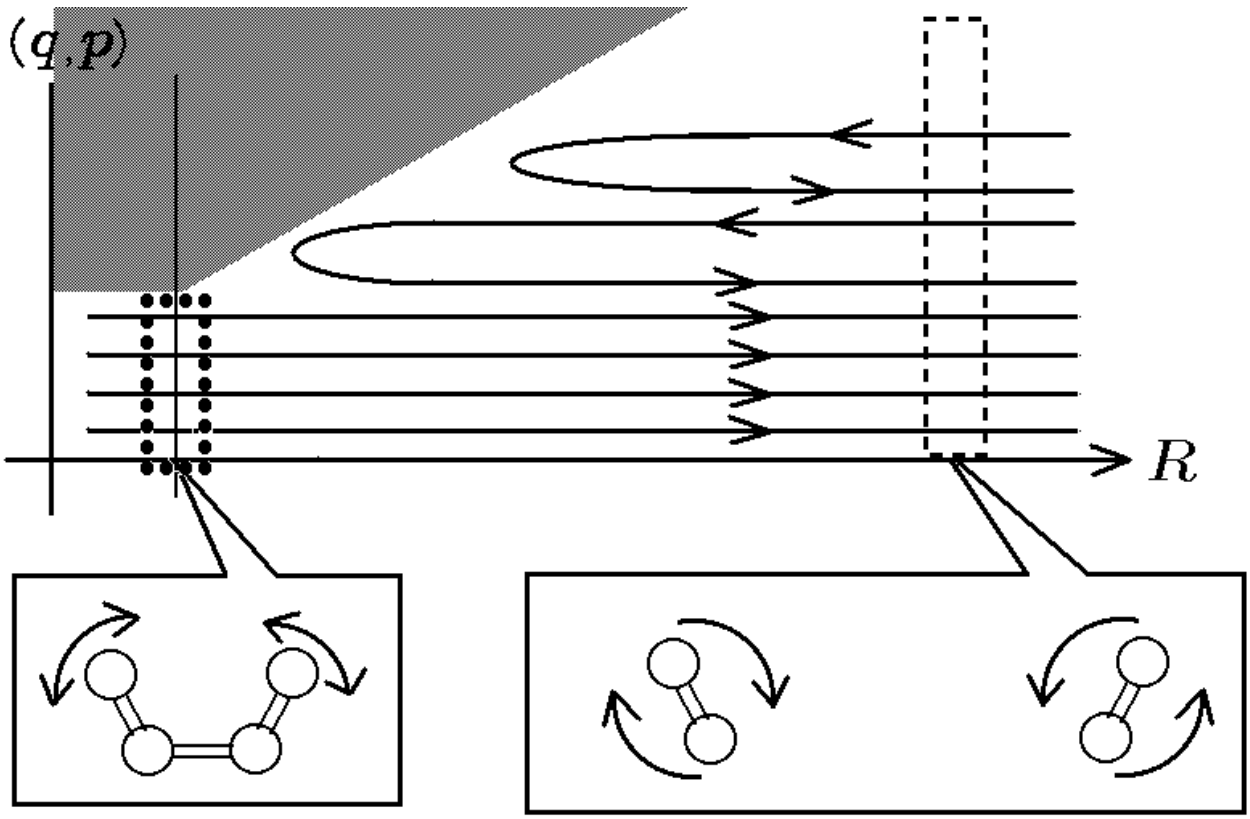

Figure 2.8: Schematic figure of the phase space of the reaction system. The horizontal axis represents the distance R between two NO's. The vertical axis represents the other degrees of freedom such as bending motions. The points in the gray area are not accessible with the available energy of the reaction due to the large vibrational potential energy. The inaccessible region becomes larger as R decreases and the rotational motions of product NO's change into bending and torsional vibrations in the intermediate. The "statistical distribution of the intermediate" populates all the phase space points rounded by the dotted lines equally, while the statistical distribution of the products such as PST distribution populates all the points within the dashed lines.

we consider that the success of the half-collision calculation still has its significance from the following reason. The half-collision calculation starts with the structure which is rather similar to the two independent NO fragments since the two NO's are quite distant at 2.263 Å. Furthermore, we found that only negligible amount of trajectories went back to shorter distance than the initial value. Thus, the trajectories in the half-collision calculation experience rather limited portion of the global PES than is imagined from the word "half," although we used this word for simplicity. Because there is only small anisotropy of the PES in the exit region except for the hard-core repulsion of the nuclei, we consider that the results of the half-collision calculation are not very sensitive to the details of the PES. Therefore, if the inaccuracy of the exit region of the present PES is not so severe, the success of the half-collision calculation indicates that the statistical assumption for the intermediate represent the real system to some extent.

As stated in Sec. 2.4.2, the near-statistical distribution with the sharp decrease of the high-j' populations can be explained by the balance between the distribution at the ONNO intermediate and the interaction in the exit region of the PES. Since no deep well exists in the PES of this reaction, it is plausible that the reaction intermediate does not have the completely statistical distribution. Although the full-collision calculation hardly reproduced the observed distributions, the calculated result indicates that the intermediate is biased toward the phase space points producing high-j' products. This trend is qualitatively consistent with the bias to make the half-collision result closer to the experimental one. Therefore, we suggest that the real dynamics of this reaction consists of the following two factors: (i) an ONNO intermediate with near-statistical distribution a little biased toward the phase space points correlating with high-j' products; (ii) the rotation-translation interaction in the exit region similar to the present PES, which makes this near-statistical intermediate distribution correspond to the experimentally observed high-j' depressed distribution of the products.

The occurrence of the near-statistical distribution in this highly exothermic reaction without a stable intermediate is not expected in the traditional understanding of gas-phase chemical reaction dynamics. As an important factor which causes the considerable energy randomization in the ONNO intermediate, Akagi *et al.*[58] suggested mass effects. According to their discussions, the presence of four heavy atoms in the system provides low frequency vibrations to increase the state density and also causes large momentum coupling among the local vibrational modes. These effects seem to occur even in the full-collision calculation on the current PES since the calculated vibrational and rotational state distributions of *new* and *old* NO's are very similar. However, the discrepancy between the full-collision calculation and experimental observation

should be attributed to the defect of the current PES since the full-collision calculation already includes the mass effects. It is found that the vibrational distribution obtained by the full-collision calculation is less excited than the experimentally observed one,[18] in contrast to the overestimate of the rotational excitation. We therefore consider that poorly reproduced couplings between the stretching motions and bending/torsional motions of the ONNO system are the possible defect of the current PES.

In closing this section, it should be emphasized that the comparison between the half-collision and the full-collision calculations is very helpful to deepen the understanding of what takes place on a PES during the reaction. This approach will be promising when a more accurate PES reproducing the product state distribution of this reaction is obtained.

2.5 SUMMARY AND CONCLUSIONS

We have determined the nascent product state distributions of NO(X $^2\Pi$, v'=0–2; j') produced from the reaction O(^{1}D)+N_2O up to $j' \approx 100$ where the distribution decayed under the noise level and no significant populations were found in higher rotational levels. All the rotational state distributions in these vibrational levels are similar and near statistical. However, the populations in high-j' levels decreased more rapidly than PST prediction. This behavior can be understood in view of the rotation-translation interaction in the exit region of the PES. The depression of the high-j' population was reproduced in half-collision QCT calculations with the assumption of statistical distribution at the intermediate. We concluded therefore that near-statistical distribution a little biased toward the high-j' products is generated at the intermediate and then this distribution is propagated to yield high-j' depressed product distribution due to the exit region interaction.

Chapter 3

Quasiclassical trajectory study of $O(^1D) + N_2O \rightarrow NO + NO$: Classification of reaction paths and vibrational distribution

3.1 INTRODUCTION

The nascent state distribution of reaction products is the major experimental information on reaction dynamics. Until today it has been generally believed[6] that the product state distribution is closely related to the stability of the reaction intermediate, that is, the depth of the well on the potential energy surface (PES) of the system. If the PES possesses a deep well, the system is expected to be trapped in it for sufficiently long period which enables energy randomization, resulting in a statistical distribution of the products. On the other hand, if there is no significant well on the PES, the lifetime of the intermediate is likely to be short and the energy is distributed in only a part of the rovibrational modes of the products.

However, contradictory experimental results[17,18] were found for the reaction of $O(^1D)$ with N_2O:

$$O(^1D) + N_2O \rightarrow NO + NO \qquad \Delta H_f^\circ(0) = -341 \text{ kJ/mol}, \tag{3.1}$$

$$O(^1D) + N_2O \rightarrow N_2 + O_2 \qquad \Delta H_f^\circ(0) = -520 \text{ kJ/mol}. \tag{3.2}$$

Many experimental studies[13–22] have been done by measuring product state distributions and vector properties for channel (3.1). The two NO products should be distinguished from dynamical viewpoint. Hereafter we use prime symbols for this purpose and express the reaction as follows:

$$O(^1D) + NN'O' \rightarrow NO + N'O'. \tag{3.3}$$

The newly formed NO originating from $O(^1D)$ is called a "new" NO and the N′O′ which already exists in the reactant N_2O is called an "old" NO. Akagi *et al.*[17,18] distinguished these two kinds of NO by using isotopically labeled $^{18}O(^1D)$, and measured the individual vibrational state distributions for $v' \leq 17$. The sum of the distribution of the new and old NO products decreased monotonically as the vibrational quantum number increased and was very close to the statistical distribution up to $v' \approx 10$ and became smaller than the statistical one for higher v'. The statistical nature of the vibrational distribution was further confirmed by the measurement with FTIR spectrometer. [16,21] Furthermore, although the vibrational distribution of the new NO is more excited than that of the old NO, the populations of both types of the products in each vibrational level are not significantly different.[17,18] This nearly equal energy partitioning between the two kinds of NO is surprising because neither experiment[23,24] nor calculation[25–29] has found any deeper well for this reaction than the *cis*-planar NO dimer, whose binding energy 8.3 kJ/mol[24] relative to NO + NO is very small compared to the exothermicity of 341 kJ/mol. This result forms a sharp contrast to the $O(^1D) + H_2O$ reaction, whose two types of OH products show entirely different vibrational distributions[30,31] although the reaction is considered to proceed with stable H_2O_2 intermediate.[32]

In theoretical works, González *et al.*[26] have performed high-level *ab initio* calculations at the stationary points for the $O(^1D) + N_2O$ reaction and obtained the rate constants using transition state theory and quasiclassical trajectory (QCT) calculation on a fitted pseudotriatomic London–Eyring–Polanyi–Sato surface. Although they found relatively good agreement with the experimental results in the rate constants and branching ratios, their *ab initio* calculation was limited to the neighborhoods of the stationary points and was not adequate for dynamical studies on global PES. Takayanagi *et al.*[27–29] constructed a global PES by calculating *ab initio* energies at about 10,000 grid points of planar configuration and fitted them to an analytical form. Using this $^1A'$ ground surface, they performed QCT calculation with zero impact parameter[29] and quantum calculations.[28,34] They found qualitative agreement with the experimental results on vibrational distribution and branching ratio. They also pointed out the existence of "scrambling" process:

$$O(^1D) + NN'O' \rightarrow NO' + N'O, \tag{3.4}$$

whose contribution was smaller than that of the normal NO channel (3.3) but not negligible. Recently, the authors used this PES to calculate the product rotational distribution and compared the results with experiment.[22] To elucidate the dynamics, we carried out two types of calculation, one of which utilized only exit region of the PES. Although we had relatively

good agreement with experiment by this type of calculation, the calculation using the full PES showed less satisfactory results.

In this chapter, our purpose is to clarify the detailed reaction mechanism based on the QCT analyses. In Sec. 3.2, we construct a new global PES function and characterize it with the minima and saddles. In Sec. 3.3, we perform the QCT calculations in order to investigate the dynamical features. We show that the reaction dynamics is clearly dependent on the initial condition and the reactive trajectories can be classified into four paths. One of the paths is found to have long lifetime, being trapped in a newly found well, whereas the other paths exhibit short lifetime. Contrary to the general notion, we find that the old NO vibration is highly excited along the short-lifetime paths rather than the long-lifetime one. Finally, we conclude in Sec. 3.4.

3.2 POTENTIAL ENERGY SURFACE

To construct the PES, we performed *ab initio* calculations for about 10,000 geometries in planar configuration. Here, we employed CASPT2($10_e, 8_o$)/cc-pVDZ, which is the same level as Takayanagi *et al.*[27–29] We also note that they showed that calculation of this level provided reasonable results.[29,34] These calculated points were fitted to the analytical form given in Sec. 3.5.

In order to reduce fitting errors, we divided the configuration space into seven regions and performed least-squares fitting procedure separately in each region. Thus the PES is expressed in the following form with fitted potential functions V_i and weighting functions w_i corresponding to each region i.

$$V = \frac{\sum_i w_i V_i}{\sum_i w_i}. \tag{3.5}$$

The functions V_i and w_i are expressed in analytical forms with nuclear distances (R_1, R_2, R_3, R_4, R_5, R_6)= ($R_{\mathrm{NN'}}$, R_{NO}, $R_{\mathrm{N'O}}$, $R_{\mathrm{N'O'}}$, $R_{\mathrm{NO'}}$, $R_{\mathrm{OO'}}$) shown in Fig. 3.1(a). Their detailed forms are shown in Sec. 3.5. The functions for the products ($NO + NO$ and $O_2 + N_2$) and reactant [$O(^1D) + N_2O$] regions are same as the Takayanagi PES. The root mean square of the fitting error is 4.096 kJ/mol and the maximum value of the error is 19.96 kJ/mol. In this chapter, we used the MOLPRO program for all the *ab inito* calculations.[75]

The iterative interpolation method devised by Collins and co-workers[76] might be helpful to construct an *ab initio* PES with fewer data points for this system, especially in the construction of non-planar PES. For instance, by utilizing their method, Castillo *et al.* constructed an

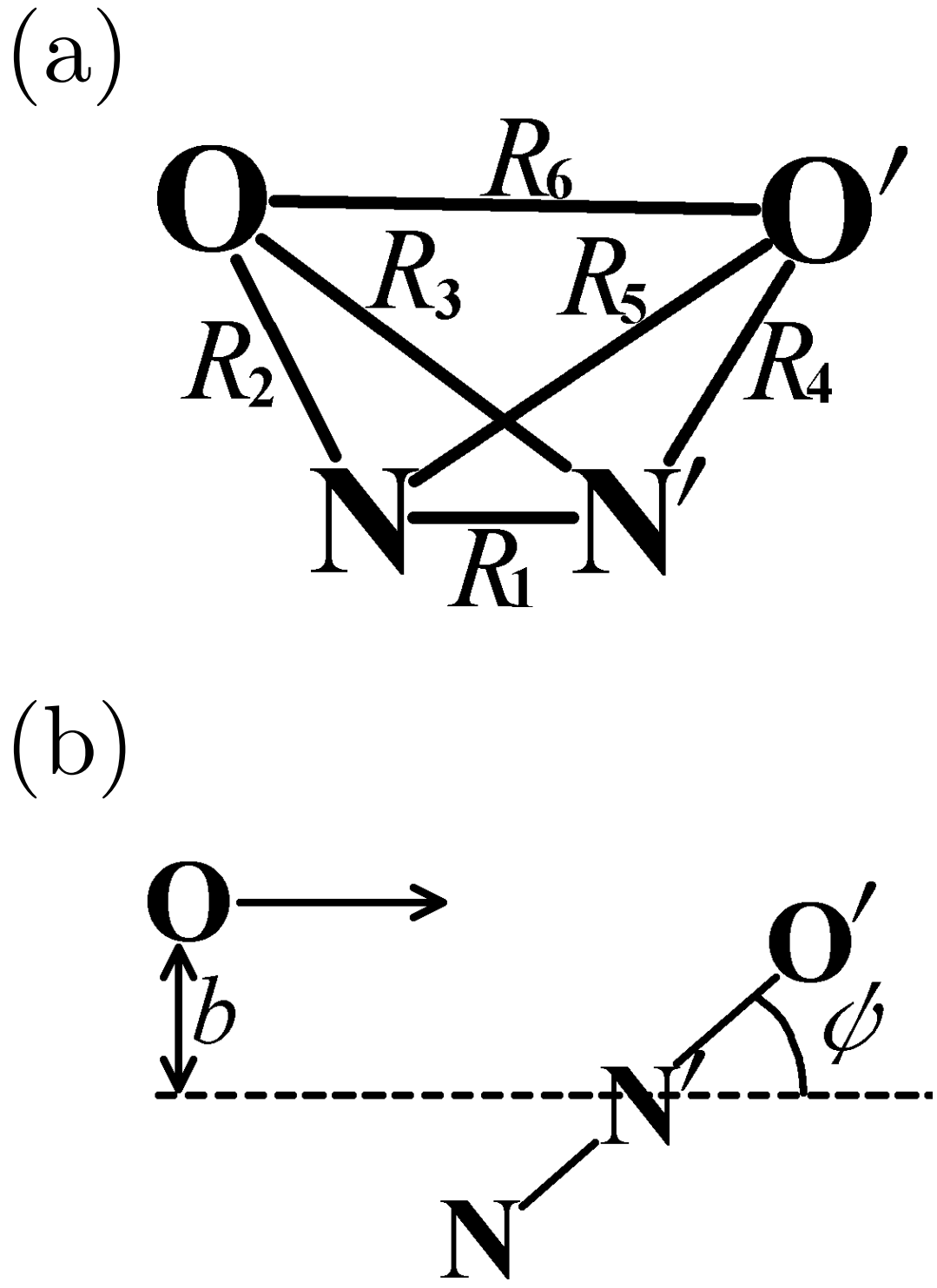

Figure 3.1: Definitions of parameters used in this paper. (a) Nuclear distances $(R_1, R_2, R_3, R_4, R_5, R_6) = (R_{\mathrm{NN'}}, R_{\mathrm{NO}}, R_{\mathrm{N'O}}, R_{\mathrm{N'O'}}, R_{\mathrm{NO'}}, R_{\mathrm{OO'}})$. (b) Impact parameter b and initial orientation angle ψ of N_2O.

ab initio PES for the $H + N_2O \rightarrow OH + N_2$ reaction with only 1400 data points in the six-dimensional space.[77] For the title reaction system, however, we consider that the application of this method would not reduce the required data points significantly in view of the following two aspects. Firstly, the CASPT2 gradient and Hessian are difficult to calculate analytically. In our experience, the interpolant moving least squares methods[78] increases the number of the required data points. Secondly, the large anharmonicity of the title reaction system also increases the required data points. Namely, the system has a complicated undulating PES, large exothermicity, and wide range of impact parameters leading to reactive collision, as seen in the following.

The energy profile with stationary points of the new PES are schematically shown in Fig. 3.2. The PES has several minima and saddle points rather than a single shallow well. The collinear saddle (Is), Y-shaped minimum (Ym), and L-shaped saddle (Ls) are newly found in this work. The imaginary mode at Is corresponds to the isomerization between two *trans*-shaped minima (Tm):

$$\begin{array}{l} O \\ \diagdown \\ N - N \\ \diagdown \\ O \end{array} \rightleftharpoons \begin{array}{l} \quad\quad O \\ \quad\quad \diagup \\ N - N \\ \diagup \\ O \end{array} \tag{3.6}$$

These two configurations are energetically equivalent and therefore only one of them is shown in Fig. 3.2, but they must be distinguished in configuration space. As will be shown later in Sec. 3.3.3, trajectories go downhill along a bath mode direction of Is and then falls into one of the *trans* minima following the reactive (imaginary) mode of Is. The Ym plays important roles, as seen in Sec. 3.3. Particularly, the scrambling process occurs in the Ym well, which can trap the trajectories for long time. From the additional *ab initio* calculations, we checked that the Ym has the real frequency of the out-of-plane vibration mode. Thus, we can consider that the Y-shaped minimum exists in the real $O(^1D) + N_2O$ system. This structure might be expected, by considering that the equilibrium geometry of NO_3 molecule is D_{3h}.[79] The electronic wave functions of both can be described by an single Slater determinant, although Eisfeld and Morokuma reveals that the insufficient dynamic and static correlations leads to the symmetry breaking problem for NO_3. It is worth noting that the previous density functional theory (DFT) calculation of this system predicted that the Y-shaped structure is a transition state but not minimum.[80] This fact also shows that DFT level calculation is not appropriate for this system as emphasized by González *et al.*[26]

Table 3.1 shows geometries and energies of stationary points found in our new PES with those found by González *et al.*[26] and experimental data.[24,63,81] At these points, we also calculate

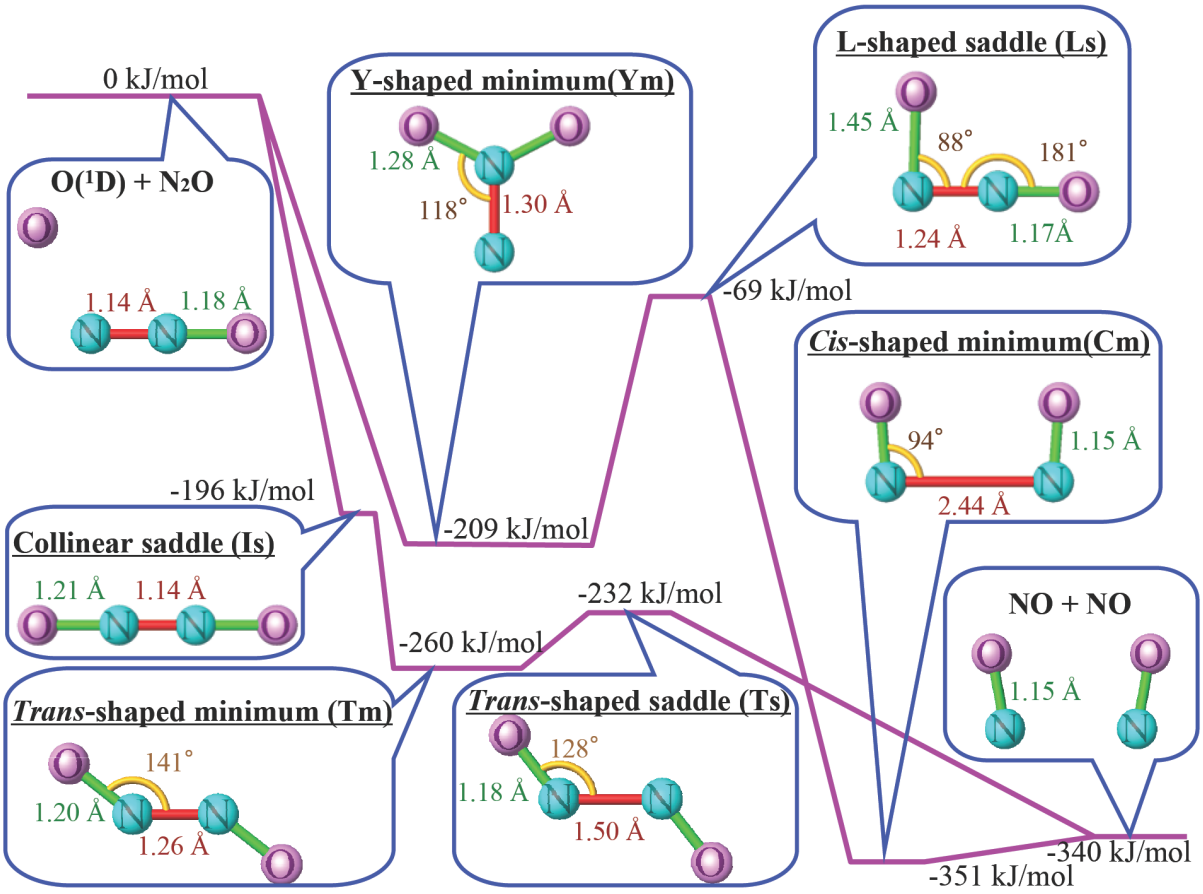

Figure 3.2: Schematic representation of the stationary points and energy profile of our new PES. Their names and geometries are shown in the insets.

the vibrational frequency of the planar normal modes, which are summarized in Table 3.2. Here we adopt the 14 and 16 AMU for the masses of nitrogen and oxygen, respectively, in order to compare them with the results of the former works.[26,81] The geometrical parameters and normal mode frequencies of reactant $[O(^1D) + N_2O]$ and products ($NO + NO$ and $O_2 + N_2$) are the same as Takayanagi PES[29] and agree with those of the experiments. The stationary points listed in Tables 3.1 and 3.2 can be considered to have large effects on dynamics, as explained in Sec. 3.3.2 and 3.3.3. González *et al.* found more stationary points through larger CASSCF(18,14) calculations,[26] although we consider that their contribution to the dynamics is minor to reproduce the product vibrational distribution. The *trans*-shaped minimum (Tm) and saddle (Ts) points can be considered to correspond to "MIN $B1$" and "TS $B1$" of González *et al.*, respectively. Our geometries for these points are in good agreement with those of González *et al.*, while the energies are slightly lower. The normal mode frequencies are in qualitative agreement, as seen in Table 3.2. The *cis*-shaped minimum (Cm) corresponds to "MIN $D1$" of González *et al.* and experimentally found NO dimer.[23,24,63,81] For this minimum point, we have obtained better agreement with experiment than González *et al.* In particular, the R_{NN} for our PES is considerably (by 0.63 Å) closer to the experimental one than that for the González *et al.*

Table 3.1: Geometies and energies of stationary points. Results of higher level calculation in Ref. 26 are shown in parentheses, when available. The available experimental data are shown in brackets.

Stationary point	R_{NN} / Å	R_{NO} / Å	∠NNO / deg.	Dihedral / deg.	Energy / kJ mol^{-1}
Is	1.1409	1.2120,1.2120	180.0,180.0	180	-196
Tm	1.2597	1.1971,1.1971	141.4,141.4	180	-260
	(1.2700)[a]	(1.2099,1.2099)[a]	(137.7,137.7)[a]	(180)[a]	(-277)[ae]
					(-174)[af]
Ts	1.5015	1.1814,1.1814	127.9,127.9	180	-232
	(1.4578)[b]	(1.1892,1.1892)[b]	(129.5,129.5)[b]	(180)[b]	(-258)[be]
					(-167)[bf]
Ym	1.2977	2.2056,1.2817	31.0,117.5	180	-209
Ls	1.2407	1.4540,1.1679	87.7,179.3	180	-69
Cm	2.4376	1.1527,1.1527	94.3,94.3	0	-351
	(3.0623)[c]	(1.1603,1.1603)[c]	(90.8,90.8)[c]	(0)[c]	(-345)[ce]
					(-329)[cf]
	[2.2630][d]	[1.1515,1.1515][d]	[97.2,97.2][d]	[0][d]	[-353][g]

[a] MIN $B1$ of Ref. 26.
[b] TS $B1$ of Ref. 26.
[c] MIN $D1$ of Ref. 26.
[d] Experimental data taken from Ref. 63.
[e] CASPT2//CASSCF(18,14) level calculation of Ref. 26.
[f] CASSCF(18,14) level calculation of Ref. 26.
[g] Experimental data derived from Ref. 24 and Ref. 81.

3.3 QUASICLASSICAL TRAJECTORY ANALYSES

In QCT calculations, the classical equations of motion for the $O(^1D) + N_2O$ collision were numerically integrated by fourth-order Runge-Kutta method with variable time step.[62] Energy conservation was confirmed up to 10 cm^{-1}. Since the *ab initio* PES is only available for planar configurations, the dynamics calculations were confined in two-dimensional collision plane. However, we can consider that this planar dynamics contains the essential features of this reaction because of the good agreement with the experimental results as we will see in Sec. 3.3.1. To compare our results with the experiments of Akagi *et al.*,[17,18] we employed the

Table 3.2: Harmonic vibrational frequencies (in cm^{-1}) of in-plane normal modes at the stationary points. The symmetries of the vibrational modes are given in parentheses. Results of higher level calculation in Ref. 26 are shown in parentheses, when available. The available experimental data are shown in brackets.

Stationary point	ω_1	ω_2	ω_3	ω_4	ω_5
Is	688.6i (π_g)	2658.0 (σ_g^+)	1258.2 (σ_u^+)	906.4 (σ_g^+)	316.2 (π_u)
Tm	2080.7 (a_g)	1486.9 (b_u)	858.1 (a_g)	622.2 (a_g)	485.3 (b_u)
	(1672.4)[a]	(1520.2)[a]	(810.2)[a]	(496.6)[a]	(401.8)[a]
Ts	750.9i (a_g)	1611.2 (a_g)	1538.1 (b_u)	442.8 (a_g)	415.8 (b_u)
	(561.4i)[b]	(1610.5)[b]	(1604.7)[b]	(398.4)[b]	(611.1)[b]
Ym	1907.7 (a_1)	1465.2 (b_2)	1324.9 (a_1)	692.6 (a_1)	254.1 (b_2)
Ls	661.0i (a')	2223.7 (a')	1195.4 (a')	689.0 (a')	368.8 (a')
Cm	1877.5 (a_1)	1862.8 (b_1)	460.7 (b_1)	214.3 (a_1)	156.1 (a_1)
	(1890.5)[c]	(1886.2)[c]	(113.2)[c]	(85.0)[c]	(31.2)[c]
	[1863.4][d]	[1776.3][d]	[242.9][d]	[299.3][d]	[175.4][d]

[a] MIN $B1$ of Ref. 26.
[b] TS $B1$ of Ref. 26.
[c] MIN $D1$ of Ref. 26.
[d] Experimental data taken from Ref. 81.

nuclear masses of $^{18}O + ^{14}N^{14}N^{16}O$ and the collision energy was fixed to 20.9 kJ/mol, which corresponds to the mean value under their experimental condition.

3.3.1 Product vibrational distribution

Figure 3.3(a) shows the calculated product vibrational distributions for $N^{18}O$ (new NO) and $N^{16}O$ (old NO) with the experimental ones of Akagi *et al.*[18] and Hancock *et al.*[21] The results of Hancock *et al.*, which do not distinguish the two NO's, appear mainly in the region between the two distributions of Akagi *et al.* In QCT calculation, we sampled about 200, 000 trajectories whose initial conditions are chosen according to the classical Boltzmann distribution of N_2O rotation at 300 K and the zero-point vibrational energy of the present PES. As mentioned above, there are two channels to NO+NO: the normal product channel (3.3) and the scrambled channel (3.4). The experiment of Akagi *et al.*[18] distinguished the two O atoms by using isotopically labeled $^{18}O(^1D)$ but not the N atoms. Thus, in order to make comparison with their experiment, we show in Fig. 3.3(a) the sum of the population of NO and N′O by downward open triangles, and that of N′O′ and NO′ by upward open triangles. The former corresponds to "new NO" of Ref. 18 and the latter to "old NO." The computational and experimental distributions agree well on their qualitative features in that both distributions decrease monotonically as

increasing product vibrational energy and the difference between the vibrational distributions of $N^{18}O$ and $N^{16}O$ is small, although the QCT underestimates vibrational excitation slightly. Taking into account the fact that our QCT calculations do not include the out-of-plane motion, the agreement between the measured and calculated results is so good that we can consider that our planar model includes the essential features of this reaction. We also calculated the product vibrational distributions for each channel. The results are shown in Fig. 3.3(b). The closed triangles show the vibrational distribution of the normal product channel (3.3), with downward triangles depicting "new NO"(NO) and upward ones "old NO"($N'O'$). The gray triangles show the distribution of the scrambled channel (3.4), with downward triangles depicting $N'O$ and upward ones NO'. The product vibrational distributions for the normal product channel are very similar to the total ones, while the contributions of the scrambled channel is minor, but not negligible.

For further investigation of the dynamics, we first examined the effect of initial rovibrational motion of the reactant N_2O, by performing additional QCT calculations where N_2O is initially fixed to its equilibrium configuration with zero rovibrational momenta. Fig. 3.3(c) shows the resulting product vibrational distributions. Comparing Fig. 3.3(c) with (b), we can see that the vibrational excitation is diminished probably due to the smaller amount of total energy. However, the qualitative features like the similarity between the two NO's are well conserved. Therefore we can consider that the effect of initial rovibrational motion is minor and most of the important dynamical features of this system are still contained in the dynamics with the zero rovibrational energy of initial N_2O. The reason of this is likely to be the large exothermicity of this reaction. The sum of zero-point energy and 300 K rotational energy of N_2O amounts to ca. 2000 cm^{-1}, which is less than 10 % of the exothermicity and therefore is not likely to affect the dynamics. This result allows us to investigate the dynamics with fixed initial condition of N_2O.

This simplification enables us to easily elucidate the initial condition dependence of the dynamics, because now we can specify the initial condition with only two parameters: impact parameter b and initial orientation angle ψ of N_2O as defined in Fig. 3.1(b). In Sec. 3.3.2 we will examine the reaction dynamics by analyzing the dependence on these two parameters.

3.3.2 Initial condition dependence of dynamics

We have seen in Sec. 3.3.1 that the initial condition of this reaction system can be specified with only two parameters. Here we analyze the dynamics by plotting various properties of trajectories on two-dimensional space of initial conditions parameterized by b and ψ. First, the

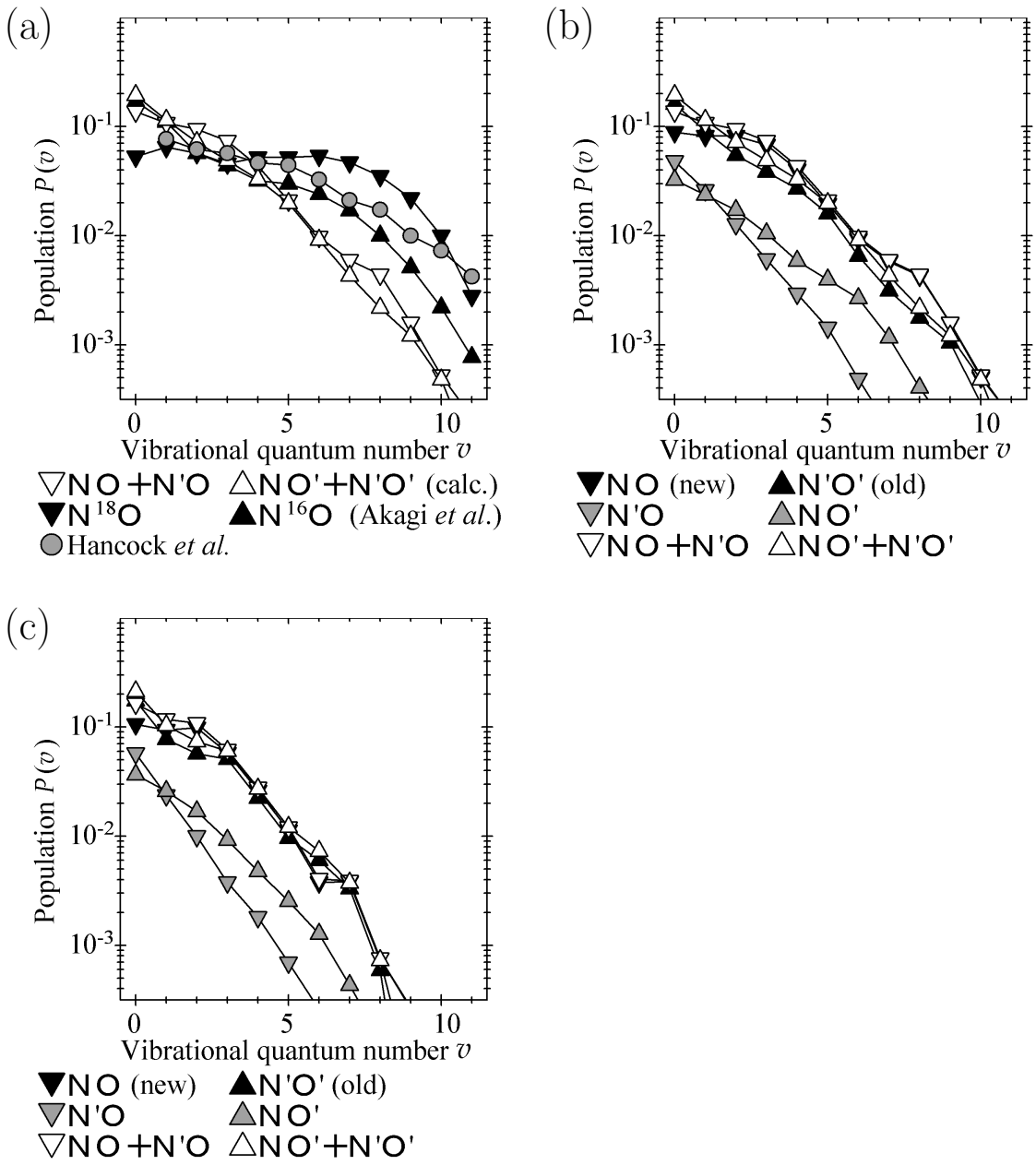

Figure 3.3: Vibrational distribution NO produced from $O(^1D) + N_2O$ obtained from experiment and calculation. (a) Comparison of the QCT and experimental results. Open triangles depict the results of QCT calculation. Closed triangles show experimental results of Akagi *et al.* [18] Gray circles show the results of Hancock *et al.* [21] (b) Results of QCT calculation of this work. Initial rovibrational state of N_2O is sampled by thermal rotational distribution and zero-point vibrational energy. Closed triangles denote the vibrational distribution of $O(^1D) + NN'O' \rightarrow NO + N'O'$ reaction channel. Gray triangles show those of $N'O + NO'$ channel. Sum of these two channels is shown by open triangles. (c) Same as (b) except that N_2O is initially fixed to its equilibrium geometry with zero rovibrational energy.

final product channels of trajectories are plotted in Fig. 3.4. For each combination of (b, ψ), the final product channel of the trajectories starting with that initial condition is shown by colors. White region means that no reaction occurs for that (b, ψ). The initial conditions leading to $O_2 + N_2$ channel are localized in the region with relatively large $|\psi|$, which corresponds to the approach of $O(^1D)$ to the O-end side of N_2O. For those leading to NO products, we need to distinguish the normal ($NO + N'O'$) and the scrambled ($NO' + N'O$) channels. The former is shown by yellow color and the latter by blue color in Fig. 3.4. In the figure, some regions are covered only by yellow color ($NO + N'O'$), while other regions have a mosaic pattern with yellow and blue ($NO' + N'O$). The other channels, atom exchange reactions like $NN'O + O'$, are minor and almost imperceptible in the figure. Although some parts of the initial condition space have mosaic pattern for the final channel, the mosaic pattern is localized in certain regions. The initial conditions leading to $O_2 + N_2$ and $NO + N'O'$ channel are also localized. Thus we can state that this system has a kind of regularity, in that the initial condition space may be divided into some regions which have different dynamical properties.

To obtain further insight into the dynamics, we calculated the following two quantities for each trajectory. One is the lifetime of the reaction intermediate. To estimate the lifetime, we needed to define the regions of "reactant," "product," and "reaction intermediate." By using the nuclear distances, geometries with R_{ON}, $R_{ON'}$, $R_{OO'} > 2$ Å were regarded as "reactant"($O + NN'O'$), those with $R_{NO'}$, $R_{ON'}$, $R_{NN'}$, $R_{OO'} > 2.5$ Å as "normal $NO + N'O'$ product", those with R_{NO}, $R_{O'N'}$, $R_{NN'}$, $R_{OO'} > 2.5$ Å as "scrambled $NO' + N'O$ product," and those with R_{ON}, $R_{O'N'}$, $R_{O'N}$, $R_{ON'} > 2$ Å as "$O_2 + N_2$ product." These values were determined by inspecting the PES and specifying the region where the interaction of the two molecules is negligible. If the system is in none of these four regions, it was regarded as "intermediate," and its "lifetime" τ is defined as the length of time during which the system has "intermediate" geometry. The "lifetime" τ thus defined can be interpreted as the "time delay" between the beginning of the interaction (entrance into the "intermediate" region) and the formation of the product (exit from the "intermediate" region). Martínez *et al.*[82] called a similar quantity "collision time," although they defined the intermediate region by using center-of-mass distances, not nuclear distances. With all this ambiguity of terminology, we will use the word "lifetime" for this quantity τ in all what follows, because we regard the word suitable for describing such concepts as "long-lived intermediate," *etc.* The other quantity is an abstract "distance" from the stationary points (shown in Fig. 3.2), which are meant to estimate how close to these points the system comes in the course of reaction. Here we use the nuclear distances $R_1, \ldots, R_6$ and

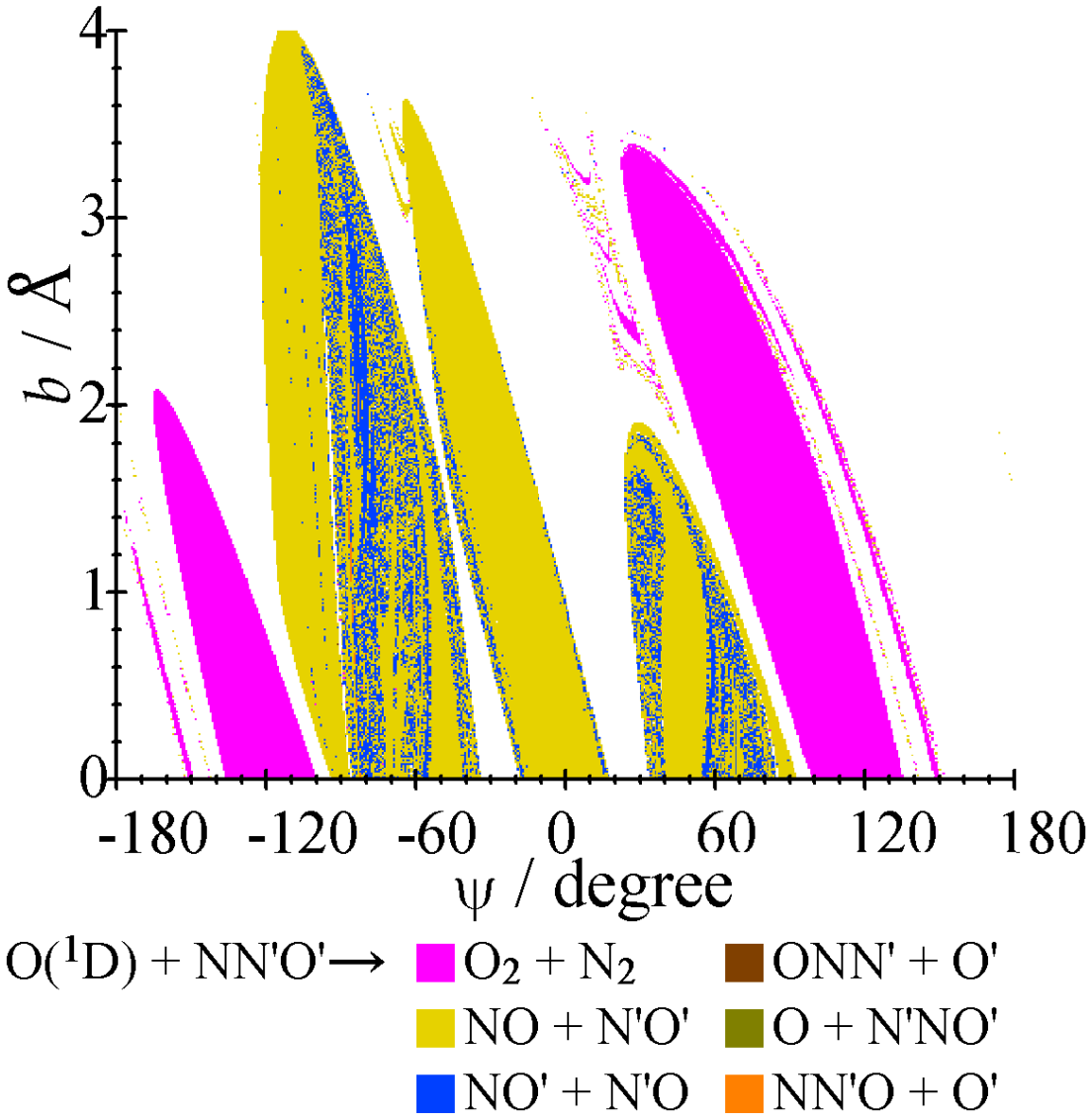

Figure 3.4: Final product channel of the reaction is plotted against the initial conditions b and ψ (see Fig. 3.1(b) for definition). Magenta, yellow, and blue colors mean that a trajectory starting with that initial condition leads to product channel $O_2 + N_2$, $NO + N'O'$, and $N'O + NO'$, respectively.

define an abstract distance D as

$$D \stackrel{\text{def}}{=} \left[\sum_{i=1}^{6} \left(R_i - R_i^0 \right)^2 \right]^{1/2}, \tag{3.7}$$

where R_i^0 is the value of the nuclear distances at the stationary points. Given one trajectory and one of the stationary points, we calculated the distance D for each time and its minimum value was taken to be plotted in the followings. Although the geometry of the system has only five degrees of freedom in the planar model, we use all six internuclear distances in the definition (3.7) of D, in order to give equal weight to all four atoms and to distinguish *cis* and *trans* geometries.

Figure 3.5 shows the initial condition dependence of the lifetime τ. In this figure we notice that the region with large τ value, which is shown in dark colors, and that with small value, which is shown by light colors, are clearly divided in the b-ψ plane. Figure 3.6(a) shows the initial condition dependence of the minimum value of distance D from the Y-shaped minimum point. Hereafter we refer to this value as $D_{\min}(\mathrm{Ym})$. In this figure again, we can see clear distinction of the region with large $D_{\min}(\mathrm{Ym})$ value, which is shown in light colors and that with small value, which is shown in dark colors. Distinction of the trajectories with large and small $D_{\min}(\mathrm{Ym})$ is clear also in the histogram plot of its distribution shown in Fig. 3.6(b). There we can see two components of the distribution with a gap at 0.8 Å.

3.3.3 Classification of trajectories and analysis of dynamics

The peculiar dependence on the initial condition shown in Sec. 3.3.2 implies that there are several classes of trajectories which have different reaction mechanisms. Thus we suggest here the following classification of the trajectories leading to NO products. By using $\psi, D_{\min}(\mathrm{Ym})$, and τ introduced above and referring to Figs. 3.5 and 3.6, we have set up four groups with the definitions listed below:

$$\begin{aligned}
&\text{Path 1} : D_{\min}(\mathrm{Ym}) > 0.8 \text{ Å}, \ -80^\circ < \psi < 20^\circ, \\
&\text{Path 2} : D_{\min}(\mathrm{Ym}) > 0.8 \text{ Å}, \ \psi < -80^\circ \text{ or } \psi > 20^\circ, \\
&\text{Path 3} : D_{\min}(\mathrm{Ym}) < 0.8 \text{ Å}, \ \tau > 160 \text{ fs}, \\
&\text{Path 4} : D_{\min}(\mathrm{Ym}) < 0.8 \text{ Å}, \ \tau < 160 \text{ fs}.
\end{aligned} \tag{3.8}$$

Distribution of these paths is shown in Fig. 3.7, where the colors indicate which path the initial condition belongs to. As can be predicted from the plots of $D_{\min}(\mathrm{Ym})$ and τ, there is a clear

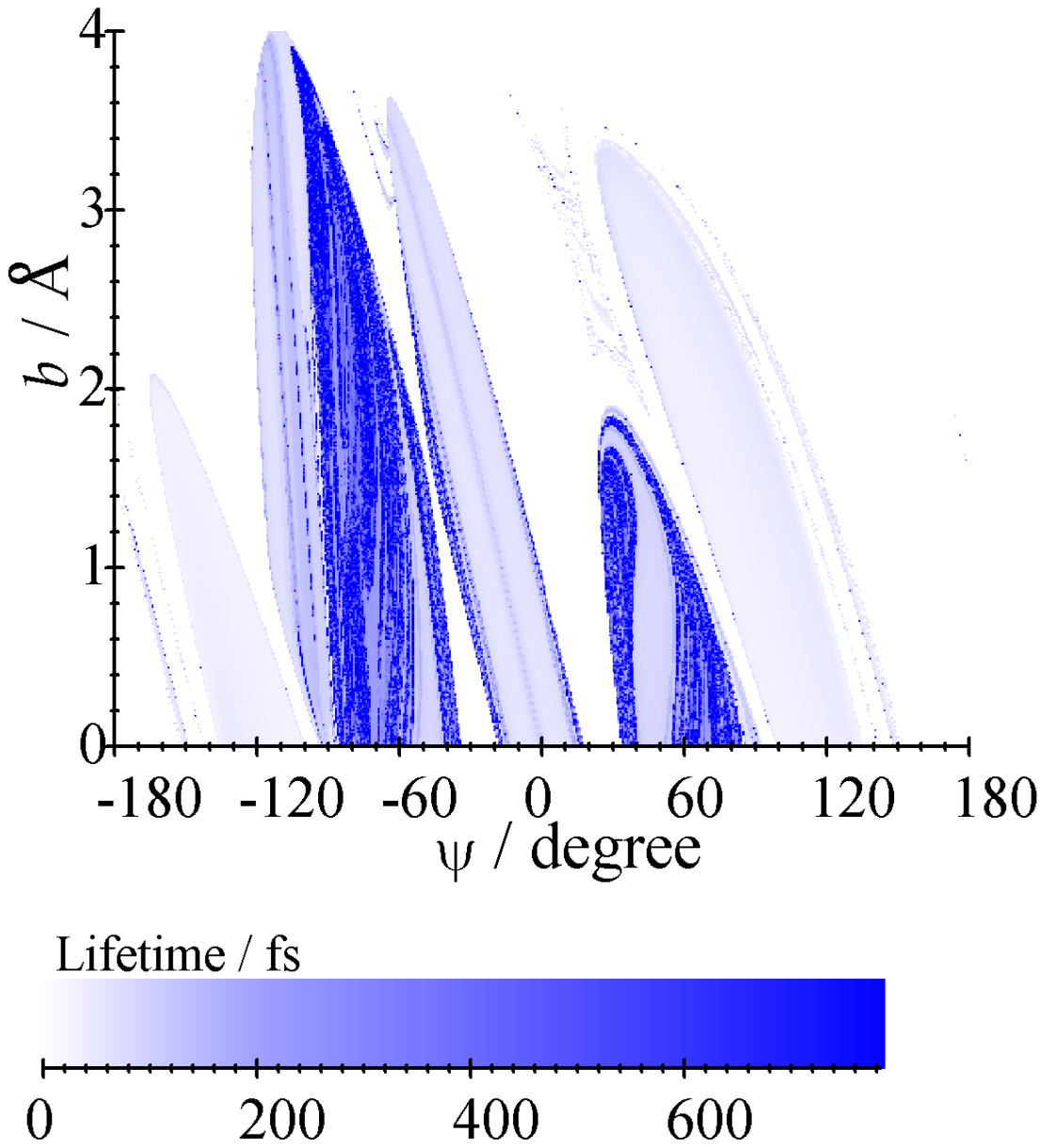

Figure 3.5: The lifetimes of the reaction intermediate (see text for definition) are plotted against the initial condition. Light and dark colors denote short and long lifetime, respectively.

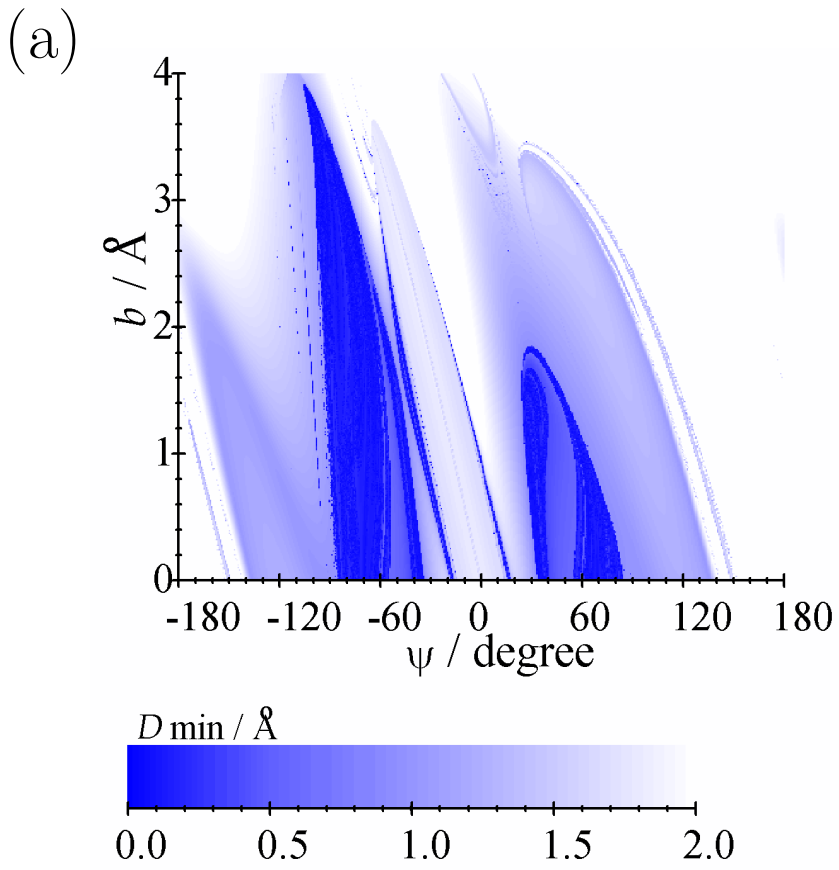

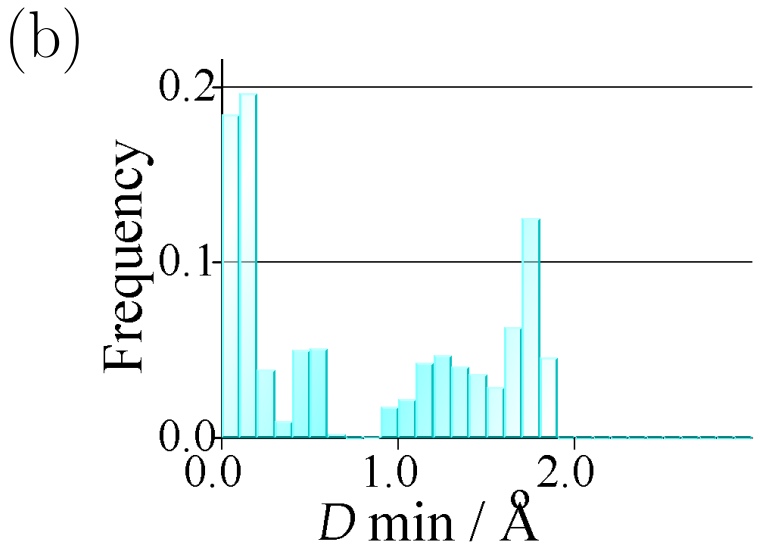

Figure 3.6: Initial condition dependence and the distribution of the minimum distance $D_{\min}(\mathrm{Ym})$ from the Y-shaped minimum point. (a) Value of $D_{\min}(\mathrm{Ym})$ is plotted against the initial condition. Light colors denote larger value and dark colors denote smaller value. (b) Histogram plot of the distribution of $D_{\min}(\mathrm{Ym})$. Note that there are two components with a gap at 0.8 Å.

distinction of these paths without any mosaic pattern. Trajectories of Path 3 and 4 come close to the Y-shaped minimum point while those of Path 1 and 2 do not. This distinction is well justified since there is a clear gap in the distribution of $D_{\min}(\mathrm{Ym})$, as seen in Fig. 3.6(b). The distinction of Path 1 and 2 can also be clearly seen in Fig. 3.7, because ψ for these paths are well separate from each other. On the contrary, the distinction of Path 3 and 4 might be artificial, since the distribution of the lifetime has no gap at $\tau = 160$ fs. Both of these paths go through the Y-shaped well and the regions of these paths in the initial condition space are next to each other. Yet, we can see that the short-lifetime component is clearly localized in a certain region of the initial condition space in Fig. 3.5, and this short-lifetime component yields only normal product channel ($\mathrm{NO} + \mathrm{N'O'}$) as can be seen in Fig. 3.4. Therefore we decided to analyze the short-lifetime component (Path 4) separately from the long-lifetime one.

As tabulated in Table 3.3, the Path 3 have the largest contribution of 43 %, which is 4 times as large as the contribution of Path 4. The contributions of Path 1 and 2 are about 20 %, respectively. Then, all four paths have non-negligible amount of contribution to the reaction. In what follows,we characterize these paths in more detail.

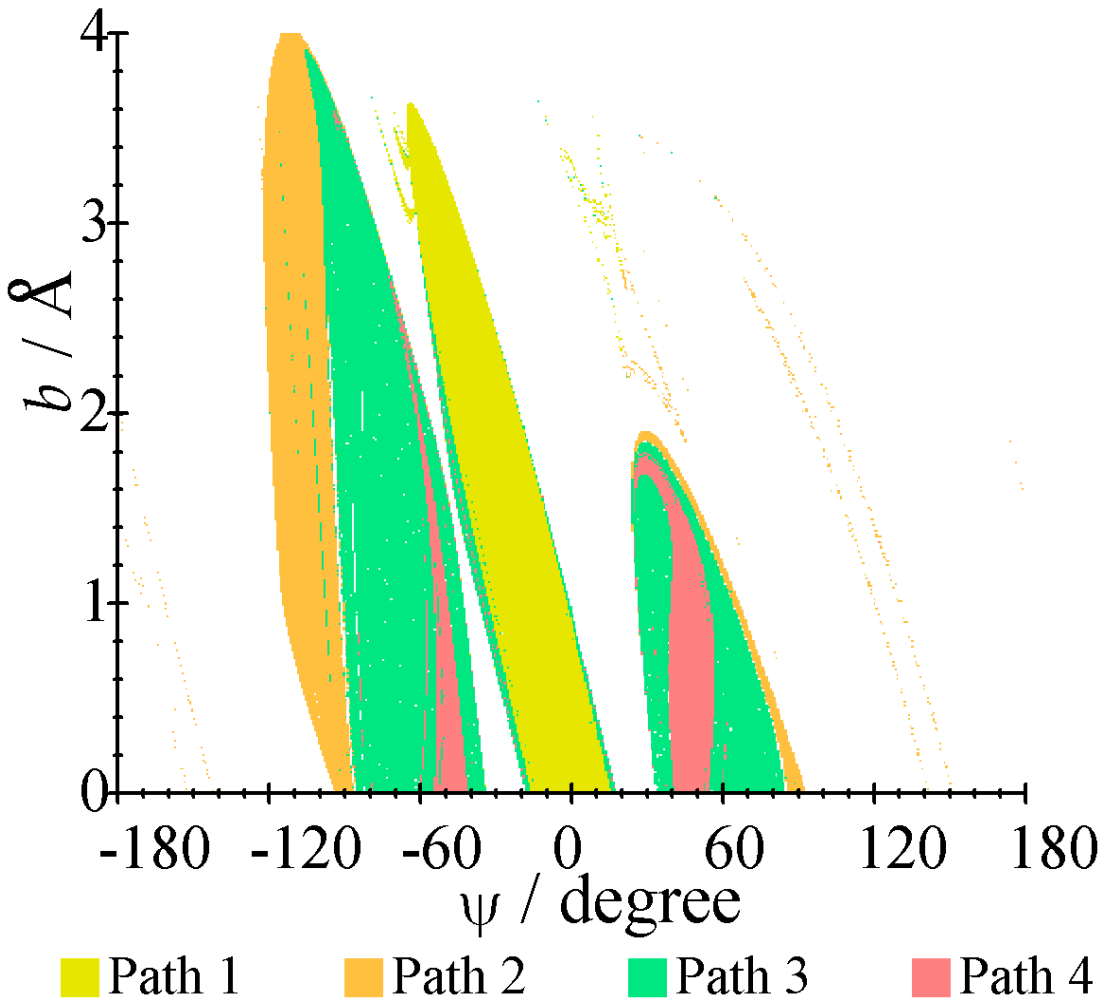

Figure 3.7: Classification of the reactive trajectories. Yellow, orange, green, and red colors show those regions where the initial conditions belong to Path 1, 2, 3, and 4, respectively. See text for the details of the definition for each path.

Table 3.3: Contribution, mean vibrational energies, and lifetime of each path.

	Path 1	Path 2	Path 3	Path 4	Total	
Contribution / %	24	23	43	10	100	
$\langle E_{\mathrm{vib}} \rangle$ / cm^{-1}						
NO	4600	2900	3200	4300	3600	3200 (7400[a])
N′O	—	—	1500	—	1500	
N′O′	6400	2100	1400	900	3000	3000 (3800[a])
NO′	—	—	3000	—	3000	
$\langle \tau \rangle$ / fs	80	140	1100	100		

[a] Calculated from experimental data of Ref. 18.

Path 1: Direct mechanism through collinear approach to *trans* minimum

As can be seen from the definition (3.8), Path 1 does not approach the Y-shaped minimum and has initial orientation of almost collinear O-N-N′-O′ structure. An example of the trajectory of this path is shown as snapshot pictures in Fig. 3.8. The initial conditions were taken to be $(b, \psi) = (0\ \text{Å}, 5^\circ)$. The figure shows that the system has indeed collinear approach and then goes to the *trans*-type structures associated with Tm. Figure 3.12(a) shows the lifetime distribution of Path 1. There we can see that the *trans*-shaped intermediate has a short lifetime probably because of the small height of *trans*-shaped saddle. Thus, reaction of Path 1 proceeds through almost "direct" mechanism with the lifetime less than 100 fs for most of the trajectories.

To investigate the contribution of this path to the vibrational distribution, we have separately calculate the vibrational distribution of only Path 1. A considerable excitation of old NO is observed in the result shown in Fig. 3.13(a). This indicates that large amount of energy flow from new NO to old NO has occurred in spite of the short lifetime. This result is contradictory to the conventional understanding of the reaction dynamics and it is implied that there is a need to consider strong coupling among the vibrational modes within ONNO intermediate, especially between the two stretching vibrations of NO bonds.

Path 2: Direct mechanism through bent approach to *trans* minimum

Trajectories of Path 2 as well as Path 1 do not approach the Y-shaped minimum. The difference from Path 1 is the direction of approach. Figure 3.9 shows an example of trajectory whose initial conditions are $(b, \psi) = (0\ \text{Å}, -90^\circ)$. There we can see that the O atom approaches the N-end of the NN′O′ through bent geometry. The system then takes L-shaped structure and bending motions are excited, causing *cis-trans* isomerization. The intermediate dissociates immediately to the products, as we have seen for Path 1.

The lifetime for Path 2, shown in Fig. 3.12(b) is a little longer than that for Path 1, but is still short (50-200 fs). In the vibrational distribution shown in Fig. 3.13(b), old NO is considerably excited, though the amount of excitation is a little less than that of Path 1. Broadly, Path 2 has a similar property to Path 1, and therefore indicates strong vibrational coupling in the intermediate stage of this reaction. A little less amount of old NO excitation of Path 2 than Path 1 implies somewhat weaker coupling in the bent structure than in the collinear one.

Path 3: Complex mechanism trapped in Y-shaped minimum

Figure 3.10 shows an example trajectory of Path 3 with $(b, \psi) = (0\ \text{Å}, -75^\circ)$. As can be seen from the definition (3.8), trajectories of this path form a long-lived Y-shaped complex. Figure 3.12(c) shows that the intermediate has long lifetime extending to ps order. This long lifetime is probably due to the large barrier height at the L-shaped saddle point relative to the Y-shaped minimum. In the geometry of the Y-shaped minimum shown in Fig. 3.2, the two O atoms are equivalent except for their masses. Therefore, once the system is equilibrated after being trapped in the well, it has almost equal probability to dissociate into both of NO + N′O′ and N′O + NO′ channels, because the isotopic labeling is not likely to affect the dynamics considerably. After passing over the barrier at the L-shaped saddle point, the system dissociates immediately to the product [Fig. 3.10(f)-(h)].

Figure 3.13(c) shows vibrational distribution of Path 3. The two product channels (NO + N′O′ and NO′ + N′O) have similar branching ratio and distribution. This is because of the equivalence of the two O atoms in the Y-shaped complex as was noted above. In each of the two channels, the two NO products have quite different vibrational energies. To be more precise, NO has larger vibrational energy than N′O′ in the normal product (NO + N′O′) channel, and NO′ has larger energy than N′O in the scrambled (NO′ + N′O) channel. In both channels, the product containing the N atom has larger vibrational energy than that containing the N′ atom. It should also be noted that the vibrational distributions of N-containing products (NO and

NO′) are very close, and those of N′-containing products (N′O′ and N′O) are also close. For the total distributions of $N^{18}O$ and $N^{16}O$, the difference between N-containing products and N′-containing products are canceled out through summing up the distributions of NO and N′O, and those of N′O′ and NO′, as shown by green symbols in Fig. 3.13(c).

The difference in the vibrational distribution of the two NO molecules produced in the same product channel in spite of the long lifetime can be understood by noting the high barrier at the L-shaped saddle. This saddle point is 0.71 eV below the reactant, and this amount of energy is likely to be equilibrated after a long lifetime in the Y-shaped reaction intermediate. However, almost 80 % of the total exothermicity is released *after* the system surmounts the barrier, Ls. As we have seen in Fig. 3.10, the system spends only short time in the exit region before dissociating to the product, and therefore the exothermicity released in the exit region of the PES has no reason to be equilibrated. At the L-shaped saddle, the NO (or NO′) bond length is longer than the equilibrium distance (1.15 Å) of isolated NO molecule, while the N′O′ (or N′O) bond has almost the same length as isolated NO. Therefore, the product molecule containing the N atom is likely to be vibrationally excited more than that containing the N′ atom. This explains the trend seen in Fig. 3.13(c).

Path 4: Direct mechanism through Y-shaped minimum

The snapshots of an example trajectory of Path 4 shown in Fig. 3.11 look much similar to those of Path 3, because it also goes through the Y-shaped well, surmounts the L-shaped saddle and then dissociates to the products. The marked difference from Path 3 is short lifetime, which can be seen from the definition (3.8) and Fig. 3.12(d). In spite of the large depth of the Y-shaped well, the system immediately reaches the L-shaped saddle point, after the O atom bounces back at the N′ atom. This path yields only normal product (NO + N′O′) and the resulting vibrational distribution [Fig. 3.13(d)] shows the largest difference between the two NO products in the four paths.

It is worth noting here that a deep well does not always ensure a long lifetime, nor yet energy randomization. Similar situation was also found in $O(^1D) + HCl$ reaction.[82] We should also note that this short-lifetime component of Y-shaped path is localized in the initial condition space (see Figs. 3.5 and 3.7). This implies that some sort of regular behavior appears in spite of the large energy above the minimum point.

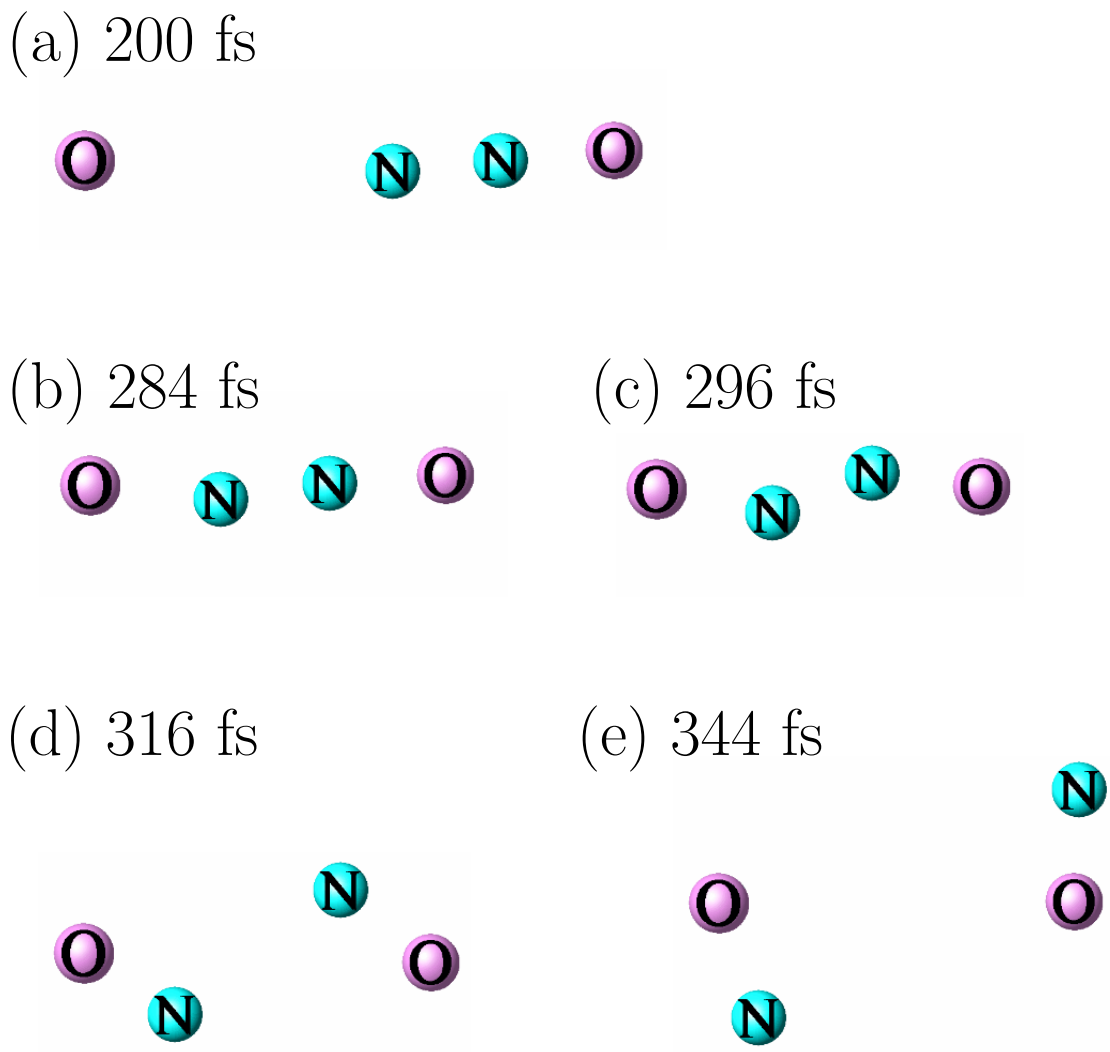

Figure 3.8: Snapshots of a trajectory which belongs to Path 1. The zero of the time is arbitrary. The initial condition is set to be $(b, \psi) = (0\ \text{Å}, 5°)$. The O atom makes a collinear approach to the N-end of the N_2O (a, b). Then the system takes a *trans*-type structure (c) and directly dissociates to the products (d, e).

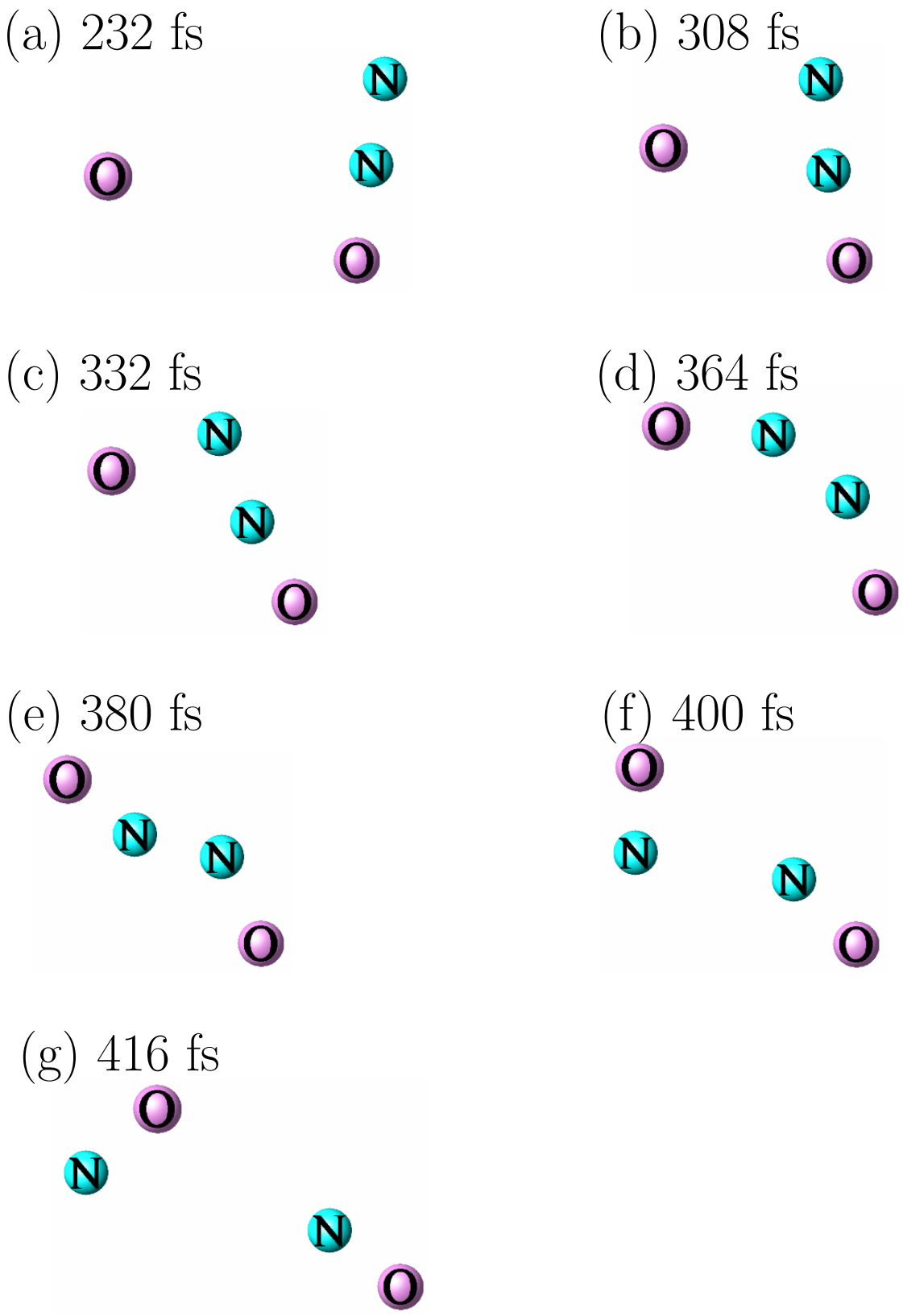

Figure 3.9: Snapshots of a trajectory which belongs to Path 2. The initial condition is set to be $(b, \psi) = (0\ \text{Å}, -90°)$. The O atom approaches the N-end of the NN′O′ making L-shaped structure (a-c). Then the O atom rotates around the N atom, causing *cis-trans* isomerization (d, e), and directly dissociates to the products (f, g).

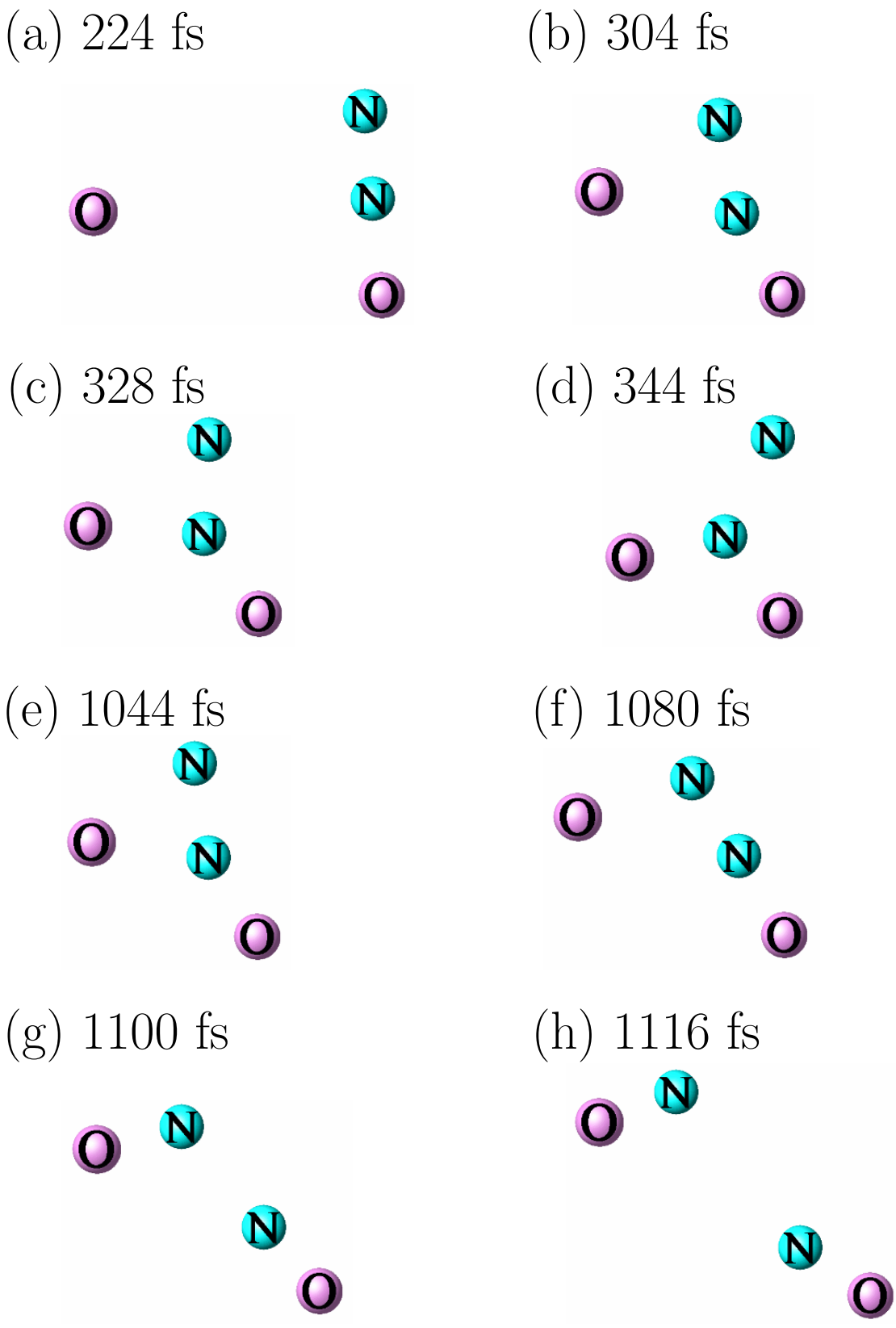

Figure 3.10: Snapshots of a trajectory which belongs to Path 3. The initial condition is set to be $(b, \psi) = (0\ \text{Å}, -75°)$. The O atom attacks the central N′ atom of the NN′O′ (a-c). Then the system is trapped in Y-shaped structure (d). After a long period about 1 ps, the central N′ atom inserts itself between N and O atom (e) and the system goes through the L-shaped saddle point (f). Then it immediately dissociates to the products (g, h).

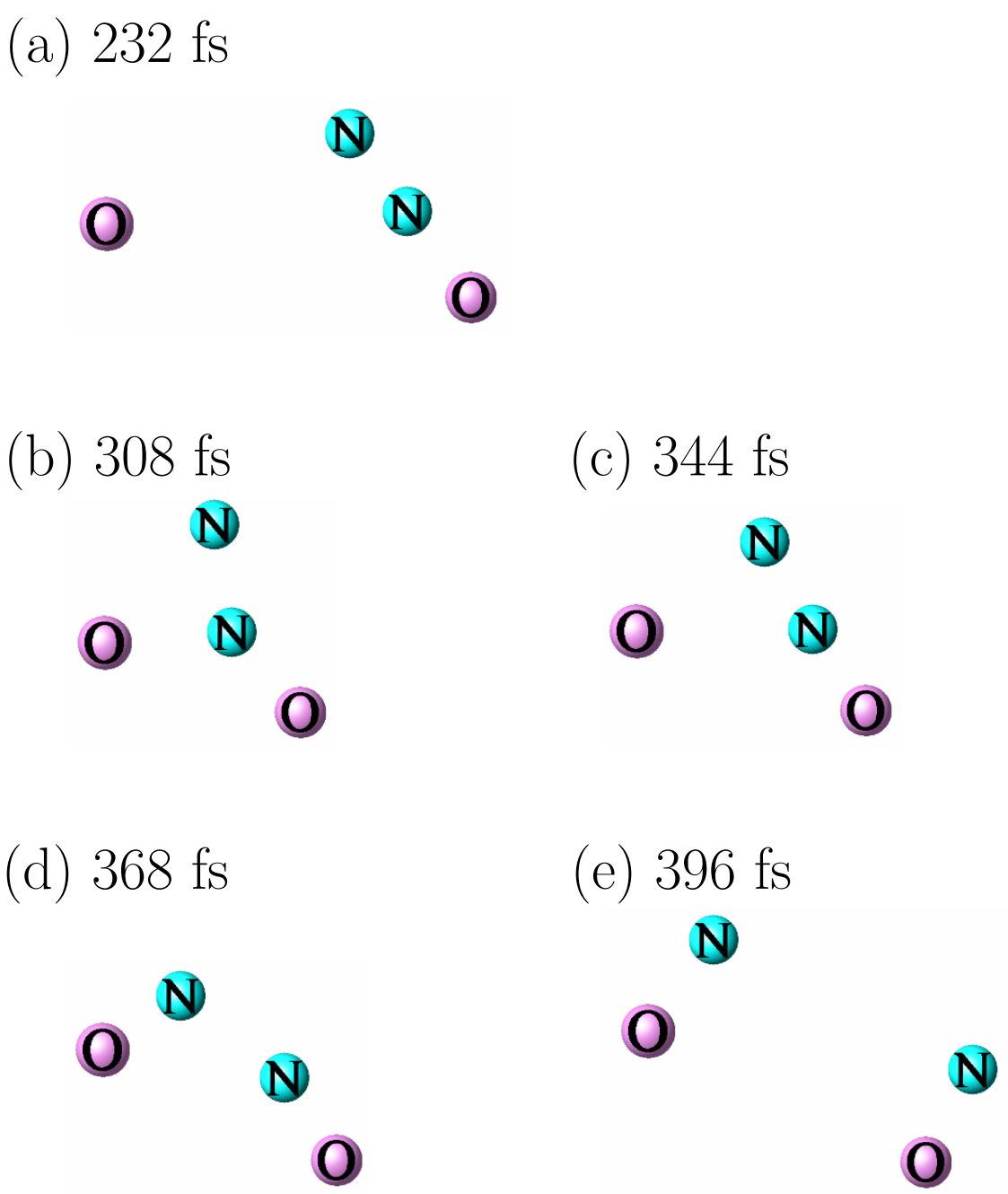

Figure 3.11: Snapshots of a trajectory which belongs to Path 4. The initial condition is set to be $(b, \psi) = (0\ \text{Å}, -45°)$. The O atom attacks the central N′ atom of the NN′O′ and forms Y-shaped structure (a, b). Without being trapped for a long time, the O atom bounces back at the N′ atom and L-shaped structure appears immediately (c, d), which then directly dissociates to the products (e).

3.3.4 Efficient energy exchange in the direct paths

In Sec. 3.3.1, we showed that our planar dynamics on the new PES reproduces the experimental results qualitatively. The QCT analyses showed that the trajectories of this reaction can be classified into four paths, which we named Path 1, 2, 3, and 4. The largest contribution comes from Path 3, in which the trajectories are trapped for long time in the Y-shaped well. However, Path 1 and 2, which have short lifetimes, are not negligible. In these paths, the N′O′ vibration are excited larger than that in Path 3, although the trajectories have short lifetimes (see Table 3.3). In order to characterize the energy distribution more qualitatively, we refer here to the ratio of the vibrational energies of the two NO products. In Path 3, NO′ has 2.0 times larger energy than N′O in the scrambled channel (N′O + NO′), and NO has 2.3 times larger vibrational energy than N′O′ in the normal product (NO + N′O′) channel. For Paths 1 and 2, which only form NO + N′O′ channel, the ratio takes much lower values of 0.7 and 1.4, respectively. This means that Paths 1 and 2 have larger excitation of the old NO in spite of their direct mechanisms.

One possible reason for the excitation of the old NO in these direct paths is the change of the equilibrium nuclear distance along the reaction path. If the N′O′ bond length changes largely along the reaction path, the force is exerted in the direction of N′O′ bond during the reaction, resulting in excitation of N′O′ vibration. From Fig. 3.2, we can see that the equilibrium length of N′O′ changes slightly in going through the reactants, *trans*-type geometries (Tm and Ts) and the products. However, we consider that it does not fully explain the similar amount of excitation of NO and N′O′, because the change of the N′O′ bond length is rather small compared to that of the new NO. Therefore, we must consider the coupled motion of the NO and N′O′ stretching modes, rather than independent excitation of these two which accidentally have the similar amount.

There are two possible scenarios for the coupled motion of the two NO stretching modes. First one is that fully chaotic motion is developed in a short period and results in near-statistical distribution of the product. Second possibility is that the motion is a regular type, but this regular motion has similar projections onto both of the two NO vibrations. This regular motion might be something like, for example, symmetric or antisymmetric stretching motion of two NO bonds, in which the two bonds vibrate with the same amplitude. At present, we consider that the latter is more probable, because we have found that the vibrational distribution of Path 1 has a non-Boltzmann type shape peaked at v = 2-3 [see Fig. 3.13(a)], which indicates incomplete randomization. For validating either of these two scenarios, it is necessary to further investigate the motion of the direct paths in terms of the geometrical structure of the phase space. Analyses in this direction will be shown in Chap. 4.

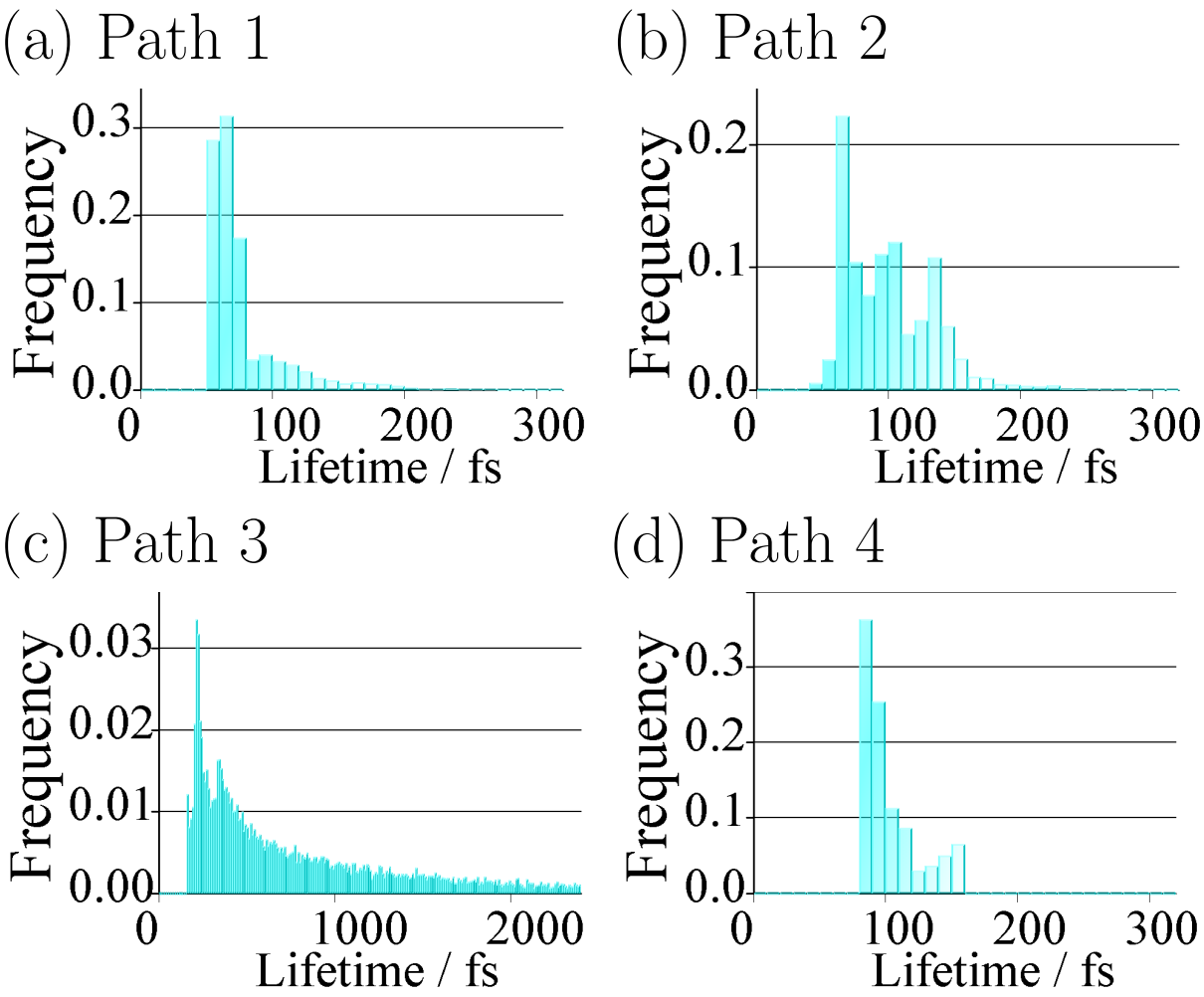

Figure 3.12: Lifetime distribution of each path. Note that the scale of the horizontal axis is different for Path 3, reflecting its long lifetime.

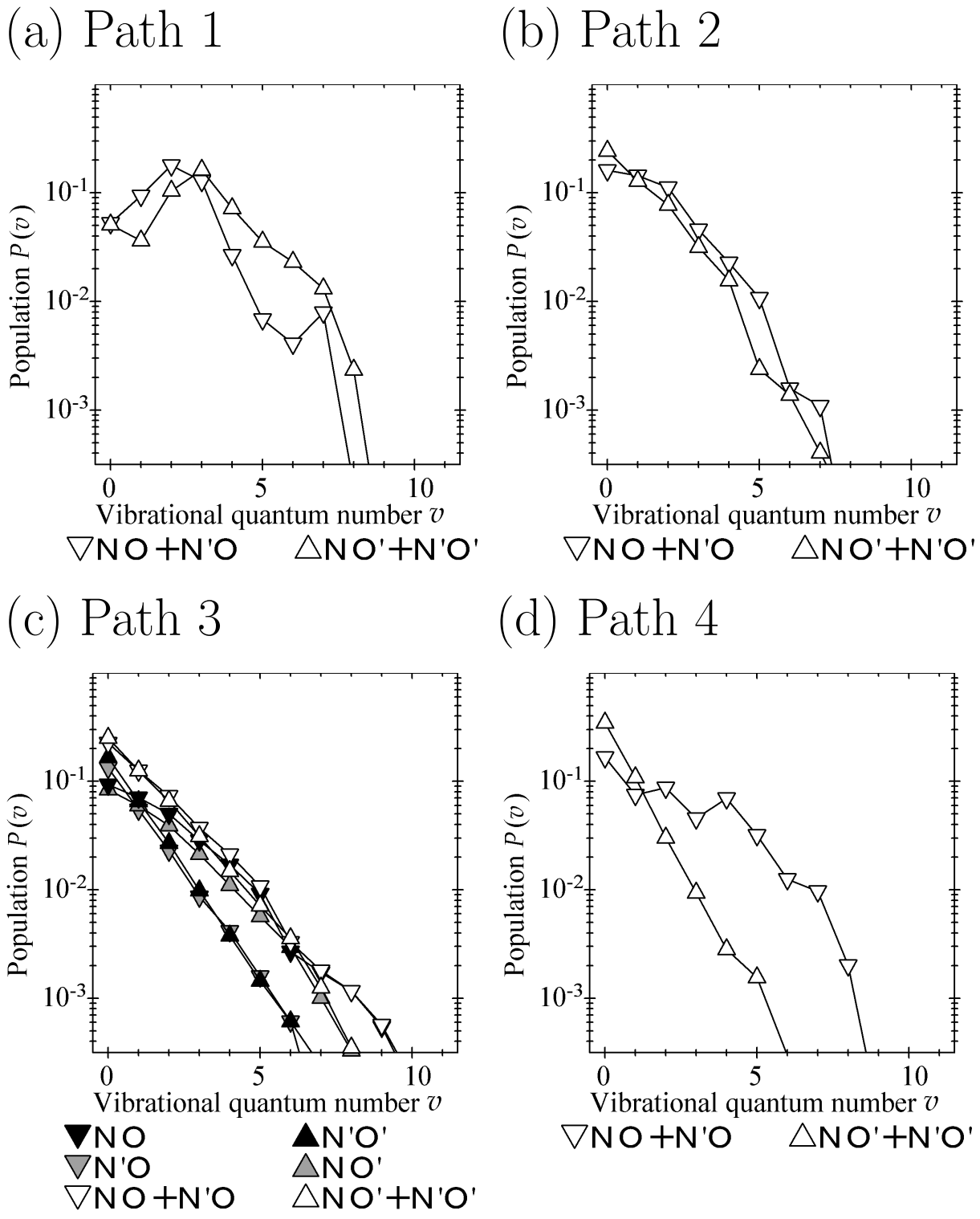

Figure 3.13: Product vibrational state distribution of each path. For Paths 1,2, and 4, only the sum of two channels is shown, because production of $N'O + NO'$ are negligible for these paths.

3.4 SUMMARY AND CONCLUSIONS

We have created a new PES for the reaction of $O(^1D) + N_2O$, using parts of the former surface of Takayanagi *et al.*,[27–29] and performed QCT calculation on the PES. The QCT calculation reproduced semi-quantitatively the experimental vibrational distribution, [17,18,21] especially the similar excitation of the two NO products.

It is newly found that the trajectories of this reaction can be classified into four paths, and the extent and mechanism of the vibrational excitation of the "old NO" are different for these paths. In Path 1 and 2, the reaction proceeds through *trans*-type geometry with direct mechanism. The difference of these two is the direction of approach of the $O(^1D)$ atom. In Path 1, the reactants approach in collinear geometry, while in Path 2 they approach through L-shaped geometry. In spite of the short lifetime, these two paths produce similar excitation of NO and N′O′. In Path 3 and 4, the system passes by the Y-shaped minimum structure, which is newly found in this work. Path 3 has a long lifetime in the Y-shaped well and produces almost equal amount of normal (NO + N′O′) and scrambled (NO′ + N′O) products. In spite of the long lifetime, the difference in vibrational energy of the two NO products is relatively large, because most of the exothermicity is released after the barrier. Path 4 exhibits a short lifetime in spite of the deep Y-shaped well, and yields only normal (NO + N′O′) channel products. This path has the largest difference in the distribution of the two NO's. Trajectories belonging to each of these four paths are localized in regularly shaped regions in the initial condition space. Especially, the regularity of the region of Path 4 implies that a deep well does not always ensure chaotic behavior.

The present work is the first recognition of the existence of more than one mechanism for this reaction. Although our calculation is an approximation with reduced dimension, it is sensible to consider that full-dimensional calculation will also exhibit several different paths. Thus, for true understanding of the dynamics of this system, separate analysis on each of the paths is inevitable. We have also shown for the first time the existence of the short lifetime paths (Path 1 and 2) with unexpectedly efficient energy exchange, whereas a short lifetime for this reaction has been only "expected" from the absence of low-energy intermediate. For further understanding of the mechanism for this efficient energy transfer, calculations like those dealing with mass effect would be desirable in the future. Also, full-dimensional calculation, although difficult, would be necessary for full understanding of the dynamics.

3.5 APPENDIX:Analytical expression of the potential energy surface

With the nuclear distances $(R_1, R_2, R_3, R_4, R_5, R_6)$ defined in Fig. 3.1(a), the potential $V(R_1,R_2, R_3,R_4,R_5,R_6)$ is expressed in the following form:

$$V(R_1, R_2, R_3, R_4, R_5, R_6) = \frac{w_0 V_0 + \sum_{i=1}^{6} \left[w_i V_i + \tilde{w}_i \tilde{V}_i \right]}{w_0 + \sum_{i=1}^{6} \left[w_i + \tilde{w}_i \right]}, \tag{3.9}$$

where $V_0 = V_0(R_1, R_2, R_3, R_4, R_5, R_6)$ is Takayanagi PES,[27–29] $V_i = V_i(R_1, R_2, R_3, R_4, R_5, R_6)$ for $i = 1, \ldots, 6$ are potential functions newly constructed in this work, $w_i = w_i(R_1,R_2,R_3,R_4,R_5,R_6)$ for $i = 0, 1, \ldots, 6$ are weighting functions, and tildes denote the permutation of nuclei:

$$\tilde{w}_i(R_1, R_2, R_3, R_4, R_5, R_6) = w_i(R_1, R_5, R_4, R_3, R_2, R_6), \tag{3.10}$$

$$\tilde{V}_i(R_1, R_2, R_3, R_4, R_5, R_6) = V_i(R_1, R_5, R_4, R_3, R_2, R_6). \tag{3.11}$$

Takayanagi PES V_0 is symmetric with respect to the four nuclear permutations:

$$\begin{aligned} &V_0(R_1, R_2, R_3, R_4, R_5, R_6) = V_0(R_1, R_4, R_5, R_2, R_3, R_6) \\ =&V_0(R_1, R_5, R_4, R_3, R_2, R_6) = V_0(R_1, R_3, R_2, R_5, R_4, R_6), \end{aligned} \tag{3.12}$$

and other functions V_i $(i = 1, \ldots, 6)$ are symmetric only under the exchange of NO and N′O′:

$$V_i(R_1, R_2, R_3, R_4, R_5, R_6) = V_i(R_1, R_4, R_5, R_2, R_3, R_6). \tag{3.13}$$

To define the weighting functions, we first introduce the following function S:

$$S(x; a, b) \stackrel{\text{def}}{=} \frac{e_1(x; a, b)}{e_1(x; a, b) + e_2(x; a, b)} \quad (a < b), \tag{3.14}$$

$$e_1(x; a, b) \stackrel{\text{def}}{=} \begin{cases} 0 & (x \le a) \\ \exp\left(-\frac{b-a}{x-a}\right) & (x > a) \end{cases}, \tag{3.15}$$

$$e_2(x; a, b) \stackrel{\text{def}}{=} \begin{cases} \exp\left(-\frac{b-a}{b-x}\right) & (x < b) \\ 0 & (x \ge b) \end{cases}. \tag{3.16}$$

This function S takes the value 0 for $x < a$ and 1 for $x > b$. By this function, the weighting functions are defined as follows:

$$\begin{aligned} w_1 =& S(R_2; 0.7, 0.8)\big\{1 - S(R_2; 1.5, 1.7)\big\} S(R_4; 0.7, 0.8)\big\{1 - S(R_4; 1.5, 1.7)\big\} \\ & S(R_1; 0.7, 0.8)\big\{1 - S(R_1; 7.0, 7.5)\big\} S(R_6; 0.7, 0.8)\big\{1 - S(R_6; 7.0, 7.5)\big\} \\ & \big\{1 - S(R_1; 1.4, 1.5)\big\} S(R_3; 1.4, 1.6) S(R_5; 1.4, 1.6) S(R_6; 1.6, 1.7) S(R_3 + R_5; 3.6, 3.65) \\ & \Big[1 - \big\{1 - S(R_3; 2.3, 2.5) S(R_5; 1.4, 1.6)\big\}\big\{1 - S(R_5; 2.3, 2.5) S(R_3; 1.4, 1.6)\big\} \\ & \quad \big\{1 - S(R_1 + R_6; 3.8, 4.0)\big\}\Big] \\ & S(R_3 - 6R_2; -7.3, -7.1) S(R_5 - 6R_4; -7.3, -7.1)\big\{1 - S(R_2 + R_4, 2.8, 2.9)\big\}, \end{aligned} \tag{3.17}$$

$$
\begin{aligned}
w_2 =& S(R_2;0.7,0.8)\big\{1-S(R_2;1.5,1.7)\big\}S(R_4;0.7,0.8)\big\{1-S(R_4;1.5,1.7)\big\}\\
& S(R_1;0.7,0.8)\big\{1-S(R_1;7.0,7.5)\big\}S(R_6;0.7,0.8)\big\{1-S(R_6;7.0,7.5)\big\}\\
& S(R_3+R_5;3.4,4.0)S(R_1+R_6;3.0,3.2)S(R_1;1.6,1.7)S(R_6;1.6,1.7)\\
& \Big[1-\big\{1-(1-S(R_3;1.7,1.85))\,S(R_3;1.05,1.15)\big\}\\
& \big\{1-(1-S(R_5;1.7,1.85))\,S(R_5;1.05,1.15)\big\}\Big], \qquad (3.18)
\end{aligned}
$$

$$
\begin{aligned}
w_3 =& S(R_2;0.7,0.8)\big\{1-S(R_2;1.5,1.7)\big\}S(R_4;0.7,0.8)\big\{1-S(R_4;1.5,1.7)\big\}\\
& S(R_1;0.7,0.8)\big\{1-S(R_1;7.0,7.5)\big\}S(R_6;0.7,0.8)\big\{1-S(R_6;7.0,7.5)\big\}\\
& S(R_1;1.6,1.7)S(R_3;1.7,1.8)S(R_5;1.7,1.8)\\
& \big\{1-S(R_6;2.1,2.2)\big\}S(R_1+R_6;3.4,3.8)S(R_3+R_5;3.8,4.0), \qquad (3.19)
\end{aligned}
$$

$$
\begin{aligned}
w_4 =& S(R_2;0.7,0.8)\big\{1-S(R_2;1.5,1.7)\big\}S(R_4;0.7,0.8)\big\{1-S(R_4;1.5,1.7)\big\}\\
& S(R_1;0.7,0.8)\big\{1-S(R_1;7.0,7.5)\big\}S(R_6;0.7,0.8)\big\{1-S(R_6;7.0,7.5)\big\}\\
& S(R_1;1.3,1.4)\big\{1-S(R_1;1.7,1.8)\big\}S(R_3;1.7,1.8)S(R_5;1.7,1.8)\\
& S(R_6;1.85,2.15)S(R_1+R_6,3.6,4.2)S(R_3+R_5,3.3,3.4), \qquad (3.20)
\end{aligned}
$$

$$
\begin{aligned}
w_5 =& S(R_2;0.7,0.8)\big\{1-S(R_2;1.5,1.7)\big\}S(R_4;0.7,0.8)\big\{1-S(R_4;1.5,1.7)\big\}\\
& S(R_1;0.7,0.8)\big\{1-S(R_1;7.0,7.5)\big\}S(R_6;0.7,0.8)\big\{1-S(R_6;7.0,7.5)\big\}\\
& S(R_1;1.6,1.7)S(R_3;1.6,1.7)S(R_5;1.6,1.7)\\
& S(R_6;1.9,2.1)\big\{1-S(R_6;3.1,3.2)\big\}\\
& S(R_1+R_6;3.6,4.2)S(R_3+R_5;3.0,3.4), \qquad (3.21)
\end{aligned}
$$

$$
\begin{aligned}
w_6 =& S(R_2;0.7,0.8)\big\{1-S(R_2;1.5,1.7)\big\}S(R_4;0.7,0.8)\big\{1-S(R_4;1.5,1.7)\big\}\\
& S(R_1;0.7,0.8)\big\{1-S(R_1;7.0,7.5)\big\}S(R_6;0.7,0.8)\big\{1-S(R_6;7.0,7.5)\big\}\\
& S(R_1;1.6,1.7)S(R_3;1.7,1.8)S(R_5;1.7,1.8)S(R_6;3.0,3.1)\\
& S(R_1+R_6;3.8,4.2)S(R_3+R_5;3.8,4.0), \qquad (3.22)
\end{aligned}
$$

$$
w_0 = \prod_{i=1}^{6}\left(1-w_i\right)\left(1-\tilde{w}_i\right), \qquad (3.23)
$$

where the unit of the nuclear distance is Å. Briefly, the function w_1 extracts the region with small NN′ distance, w_2 extracts O-N-O′-N′ or N-O-N′-O′-type structures, w_3 extracts N-O-O′-N′-type structures, w_4 extracts the region with medium NN′ distance, w_5 extracts the region

with large NN′ distance and relatively small OO′ distance, and w_6 extracts the region with large NN′ distance and relatively large OO′ distance.

As in Takayanagi PES, each part of potential function is expressed in the following form:

$$\begin{aligned} V_i(R_1,R_2,R_3,R_4,R_5,R_6) =& V_{\mathrm{NN}}(R_1)+V_{\mathrm{NO}}(R_2)+V_{\mathrm{NO}}(R_3)+V_{\mathrm{NO}}(R_4)+V_{\mathrm{NO}}(R_5)+V_{\mathrm{OO}}(R_6) \\ &+V_{\mathrm{NNO}}(R_1,R_2,R_3)+V_{\mathrm{NNO}}(R_1,R_4,R_5) \\ &+V_{\mathrm{NOO}}(R_2,R_6,R_5)+V_{\mathrm{NOO}}(R_3,R_6,R_4) \\ &+V_i^{(4)}(R_1,R_2,R_3,R_4,R_5,R_6), \end{aligned} \tag{3.24}$$

$$V_i^{(4)}(R_1,R_2,R_3,R_4,R_5,R_6) = \sum_k c_{i,k}{\rho_1}^{k_1}{\rho_2}^{k_2}{\rho_3}^{k_3}{\rho_4}^{k_4}{\rho_5}^{k_5}{\rho_6}^{k_6}, \tag{3.25}$$

$$\rho_j = R_j \exp\left(-\alpha_j(R_j-R_j^0)\right). \tag{3.26}$$

Chapter 4

Dynamics of near-collinear reaction path of $O(^1D) + N_2O \rightarrow NO + NO$ studied by normal form theory

4.1 INTRODUCTION

The investigation of geometrical structure of multidimensional phase space provides crucial information to solve various problems in general physics ranging from chemical reactions to planet motions. For a system with 2 degrees-of-freedom (DOF), it is well known that its phase space structure can easily be visualized by Poincaré surface of section (SOS). However, it becomes difficult to capture the essence of dynamics in higher dimensional systems because the increase of the SOS dimension makes the visualizations of the SOS impossible. Hence it would be desirable to introduce a low-dimensional model which may effectively describe the essential dynamics of the systems in question. For the problems of characterizing molecular vibrations around an equilibrium point, 2-DOF models with some of the bond lengths and/or angles fixed in advance have been often used to study the phase space structure below the dissociation energy [83–92]. It has been shown that the simple description by normal modes becomes invalid as the energy increases, and that new types of periodic orbits (POs) emerge through bifurcation then. The new types of POs have been characterized as local modes [83–86], precessional modes [88], dissociation modes [90, 91], and so forth, according to the energy and the types of couplings. Such effective 2-DOF models have been constructed based on empirical intuitions. In contrast to vibrations of bound molecules, dimensions of reacting systems involving bond-forming and breaking cannot be reduced by those intuitions. An appropriate theory without any empirical intuitions is needed to extract a small essential subspace from the multiple-DOF phase space.

In this respect, the Normal Form (NF) theory is a powerful tool for such dimension reduction. This theory provides considerable information on phase space geometry around stationary points by simplifying the form of Hamiltonian as much as possible. It has been applied to many systems to characterize the dynamics around rank-1 saddles as phase space structures [36–45, 47, 93, 94]. At a rank-1 saddle point, that is, an equilibrium point with one negative Hessian eigenvalue, one reactive mode and the other non-reactive bath modes have one imaginary and multiple real frequencies, respectively. It was found [36–44, 93] that up to a certain high energy, the reactive mode defined in the phase space could be separated from all the bath DOF by the application of the NF theory, even when the nonlinear couplings wash out all the constants of motion in the bath space. In other words, the reactive and bath spaces can be investigated independently if the NF theory is utilized. The dynamics in the bath space in the vicinity of a saddle can be mathematically referred to the motion in the normally hyperbolic invariant manifold (NHIM) [95, 96], which generalizes PO dividing surface in 2-DOF systems. Recently, Li *et al.* [47, 94] applied this method to a 3-DOF model Hamiltonian regarded as a prototype of isomerization reaction. The dynamics in NHIM was easily examined by SOS because the system is reduced to 2-DOF after the separation of the reactive mode. However, for systems with more DOF than three, we can no longer carry out the SOS analysis to investigate the dynamics in NHIM, because the NHIM has still more than three DOF.

In this paper, we present a dimension reduction scheme to look into the phase space geometry of the internal structure of high-dimensional NHIM. In addition to the separation of the reactive mode, we eliminate as many couplings as possible among the bath modes. By simplifying the bath mode couplings, we can construct a subsystem which describes the essential aspects of the process. We apply our dimension reduction method to the most characteristic path, named Path 1 in Capter 3 and Ref. 35, of the planar reaction of $O(^1D)$ with N_2O:

$$O(^1D) + NN'O' \rightarrow NO + N'O', \tag{4.1}$$

where prime symbols are used to distinguish the two NO products. Due to the high dimensionality of this system, it is crucial to look into the possibility to reduce the dimensionality of the bath space after it is separated from the reactive DOF, in order to reveal the complexity of the reaction dynamics. The profile of the analytic potential energy surface (PES) function constructed with CASPT2 calculations [35] is schematically shown in Fig. 3.2.

The quasi-classical trajectory study of this system revealed that the reactive trajectories of this system can be classified into four categories which were named Path 1–4. Along Path 1, the trajectories pass through three stationary points, the collinear saddle (denoted by the symbol

Is), the *trans* minimum (Tm), and the *trans* saddle (Ts). The initial stage of this reaction, where the nearly collinear approach of the $O(^1D)$ atom to N_2O takes place, can be regarded as a motion along a bath mode direction of Is. The system then falls into Tm following the reactive direction of Is. Since the large energy difference between Is and the reactant is mostly released along the bath direction, the bath mode oscillation at Is is expected to have a large amplitude. Therefore the bath modes are subject to large nonlinear couplings. It is not at all trivial to what extent we can reduce the dimensionality of the system.

The analyses of the motion around Is are interesting from the viewpoint of product energy disposal, which provide important information for clarifying the chemical reaction dynamics. Traditionally it has been believed that the deeper the potential well of the reaction intermediate becomes, the more statistically the product states distribute, since the long residence time in the well allows the considerable energy mixing [97]. However, Path 1 of the reaction (4.1) shows nearly equal excitation of two NO vibrations despite its short residence time [35]. Of the two NO products, the one originating in $O(^1D)$ is called "new NO" and the other from the reactant N_2O is called "old NO." At the initial stage of the reaction, the new NO part has an infinite nuclear distance whereas the old NO has almost the same distance as in the product. Thus, the equal vibrational energy of the products indicates that an efficient energy transfer has taken place from the new NO to the old despite the short residence time. This is in clear contrast to the traditional picture [97] mentioned above. As will be shown in Sec. 4.2, the characteristic energy exchange along Path 1 occurs when the trajectory is passing by the collinear saddle point (Is). Thus, careful analysis of the phase space around Is is quite crucial for understanding the underlying mechanism of the efficient energy exchange.

4.2 NORMAL FORM THEORY FOR PATH 1 TRAJECTORIES

In this section we first perform numerical simulations of Path 1 trajectories and describe their properties in Sec. 4.2.1. Then we describe the procedure and the results of the normal form (NF) calculation. The NF procedure consists of the following two steps. First, in Sec. 4.2.2, the Hamiltonian is expanded as the Taylor series around the collinear saddle point (Is). The error of the expansion can serve as a measure of how close the system is to the stationary point. By using this measure, we find that the excitation of the old NO vibration begins when the system comes close to Is. This means that the analysis of the dynamics in the vicinity of Is is crucial for understanding the energy transfer from the new NO to the old NO. Second, in Sec. 4.2.3, we

perform a NF transformation to represent the Hamiltonian in a simpler form where the coupling terms are eliminated as much as possible. This transformation is constructed as a perturbation series. The convergence of the series is checked by the energy difference[45] between the true Hamiltonian H and the transformed Hamiltonian $\bar{H}$ along each trajectory. If the difference is small along the reaction trajectories, we consider that the transformed Hamiltonian $\bar{H}$ is a sufficient approximation for analyzing the dynamics of the reaction.

4.2.1 Description of trajectories

Throughout the chapter, we adopt the nuclear masses of $^{18}O(^1D) + {}^{14}N^{14}N^{16}O$ for which the experiment[18] and the calculation[35] have been done. We fix the initial rovibrational energy of N_2O to zero and the impact parameter b [see Fig. 4.1(a) for the definition] is confined to zero. This makes the total angular momentum of the system zero. We have confirmed that freezing the initial rovibrational motion of N_2O does not change the product vibrational distribution significantly. As will be shown below, we find significant vibrational excitation of the old NO for the motion with $b = 0$. Therefore the analysis of the motion with $b = 0$ is an important step for understanding the energy exchange in this system.

The numerical simulation of the trajectories is performed by using the Cartesian components of three Jacobi vectors $\boldsymbol{r}_0, \boldsymbol{r}_1, \boldsymbol{r}_2$. The vector $\boldsymbol{r}_0 = (x_0, y_0)$ goes from the mass-center of NO to that of N′O′, $\boldsymbol{r}_1 = (x_1, y_1)$ goes from N to O, and $\boldsymbol{r}_2 = (x_2, y_2)$ goes from N′ to O′. In these variables, the Hamiltonian takes the following form:

$$H = \sum_{\ell=0}^{2} \frac{1}{2m_\ell} \left({p_{x_\ell}}^2 + {p_{y_\ell}}^2 \right) + V, \tag{4.2}$$

where p_{x_ℓ} and p_{y_ℓ} $(\ell = 0, 1, 2)$ are the conjugate momenta to x_ℓ and y_ℓ, respectively. V is the global PES function which we recently constructed based on the CASPT2 calculations, and

$$m_0 = \frac{(m_{\mathrm{N}} + m_{\mathrm{O}})(m_{\mathrm{N}'} + m_{\mathrm{O}'})}{m_{\mathrm{N}} + m_{\mathrm{O}} + m_{\mathrm{N}'} + m_{\mathrm{O}'}}, \tag{4.3}$$

$$m_1 = \frac{m_{\mathrm{N}} m_{\mathrm{O}}}{m_{\mathrm{N}} + m_{\mathrm{O}}}, \tag{4.4}$$

$$m_2 = \frac{m_{\mathrm{N}'} m_{\mathrm{O}'}}{m_{\mathrm{N}'} + m_{\mathrm{O}'}}, \tag{4.5}$$

with m_{O}, m_{N}, $m_{\mathrm{N}'}$, and $m_{\mathrm{O}'}$ being the nuclear masses of $\mathrm{O}, \mathrm{N}, \mathrm{N}'$, and O', respectively. In the following trajectory simulations, the equations of motion for the Jacobi vectors are numerically integrated by fourth-order Runge-Kutta method with variable time steps.[62]

To describe the trajectories, we plot the time evolution of Jacobi coordinates $(r_0, r_1, r_2, \chi_1, \chi_2)$ as defined in Fig. 4.1(b). We denote the internuclear distances of NO and N′O′ moieties as r_1

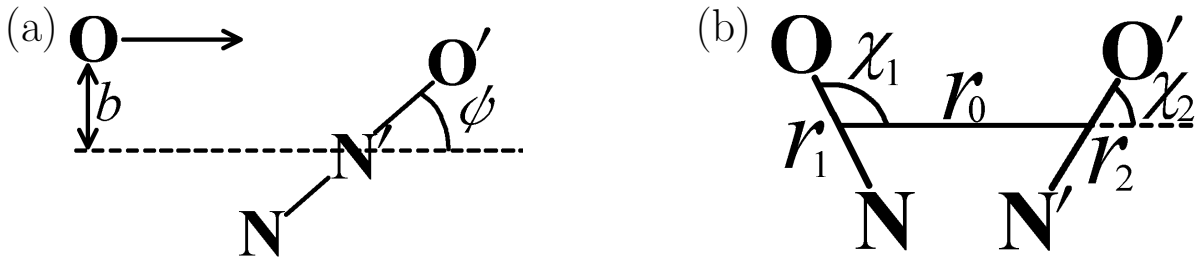

Figure 4.1: Definition of the parameters used in this paper. (a) Impact parameter b and the initial orientation ψ of N_2O. (b) Jacobi coordinates.

and r_2, respectively. The distance between the mass-centers of the two NO's is denoted by r_0. χ_1 and χ_2 are the angles between the line connecting the mass centers of NO's and the nuclear axes of NO and N′O′, respectively. These Jacobi coordinates will also be used as the starting coordinates for the normal form calculation in Sec. 4.2.3. For zero total angular momentum, the Hamiltonian takes the following form:

$$H = \sum_{\ell=1}^{2} \left[\frac{1}{2m_\ell} {p_{r_\ell}}^2 + \left(\frac{1}{2m_\ell {r_\ell}^2} + \frac{1}{2m_0 {r_0}^2} \right) {p_{\chi_\ell}}^2 \right] + \frac{1}{2m_0} {p_{r_0}}^2 + \frac{1}{m_0 {r_0}^2} p_{\chi_1} p_{\chi_2} + V(r_0, r_1, r_2, \chi_1, \chi_2), \tag{4.6}$$

where $p_{r_0}, p_{r_1}, p_{r_2}, p_{\chi_1}$, and p_{χ_2} are the conjugate momenta to r_0, r_1, r_2, χ_1, and χ_2, respectively. The derivation of this expression is given in Sec. 4.5.

The time evolution of the Jacobi coordinates is shown in the upper panels of Fig. 4.2(a)-(d) for four different initial orientations ψ of N_2O, where ψ is defined in Fig. 4.1(a). The initial conditions are generated as follows: At $t = 0$, the O(^{1}D) atom is placed in the distance of 8 Å from the mass-center of N_2O with the impact parameter $b = 0$ and the translational energy 20.9 kJ/mol $= 3.47 \times 10^{-20}$ J, which corresponds to the experimental condition of Ref. 18. N_2O is placed with the orientation $\psi = 0,\ 5,\ 10,$ and 13° for (a), (b), (c), and (d) of Fig. 4.2, respectively, with fixed rovibrational energy. Note that, for $b = 0$, trajectories of Path 1 cover the range of $|\psi| \approx$ 0-15° (See Fig. 3.7), and that there is a symmetry with respect to the reflection $\psi \mapsto -\psi$ so that we have only to consider the trajectories with $\psi =$ 0-15°. The trajectory of $\psi = 0$ has an exactly collinear configuration and thus experiences no force along the bending direction because of the symmetry. Therefore it remains in the collinear configuration ($\chi_1 = \pi$, $\chi_2 = 0$) for all the time and never falls into the *trans* region. In other words, collinear configurations form an invariant set in the phase space. After the normal form calculation, we will see in Sec. 4.3 that this invariant set is a subset of the NHIM, as long as

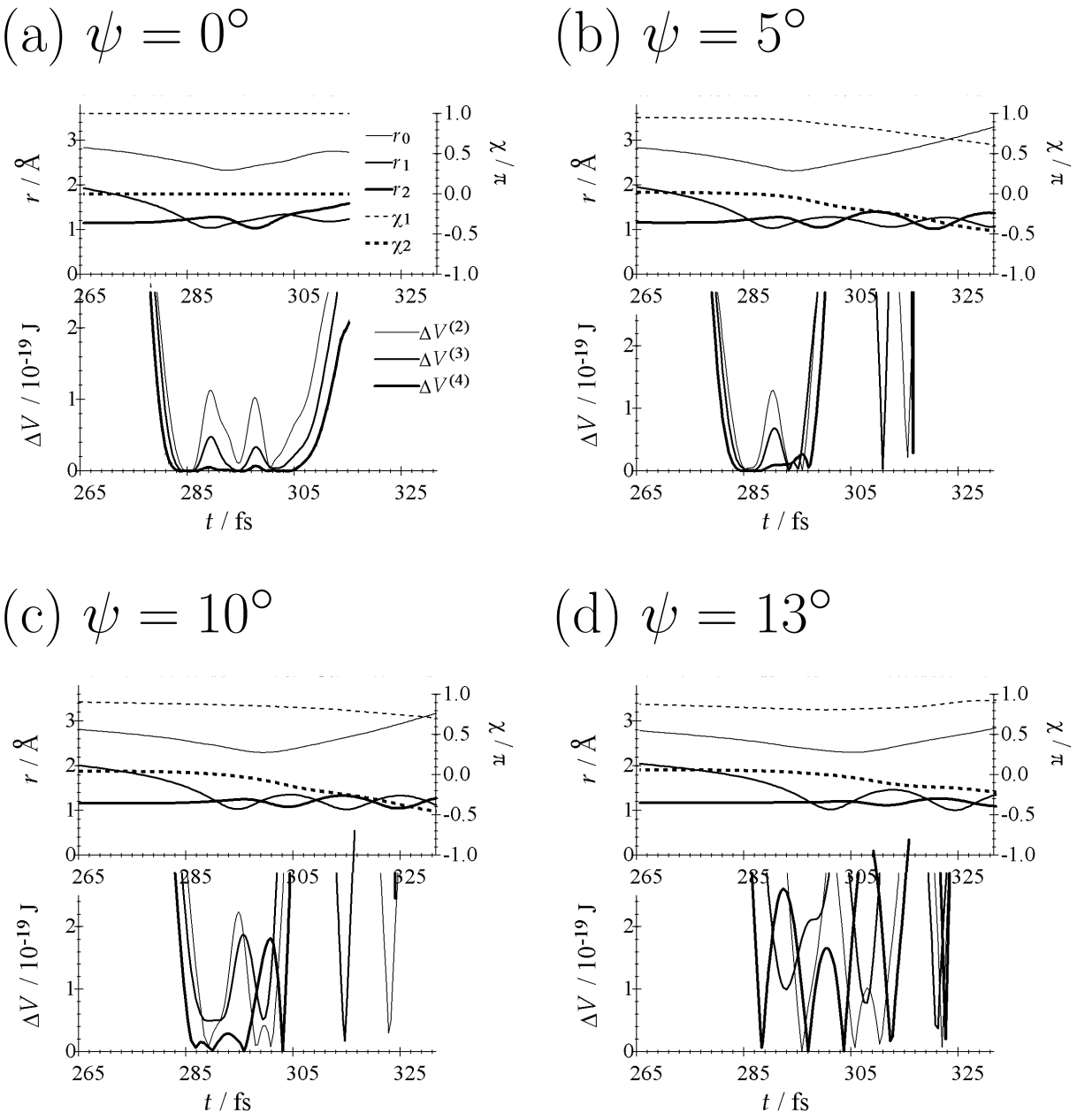

Figure 4.2: Time evolution of Jacobi coordinates and the residual error of Taylor expansion of the potential energy shown for four different initial conditions of ψ. Upper panels: Time evolution of r_0(thin solid line), r_1(medium solid line), r_2(thick solid line), χ_1(thin dotted line), and χ_2(thick dotted line). Lower panels: Residual error of Taylor expansion up to the 2nd (thin line), 3rd (medium line), and 4th order (thick line).

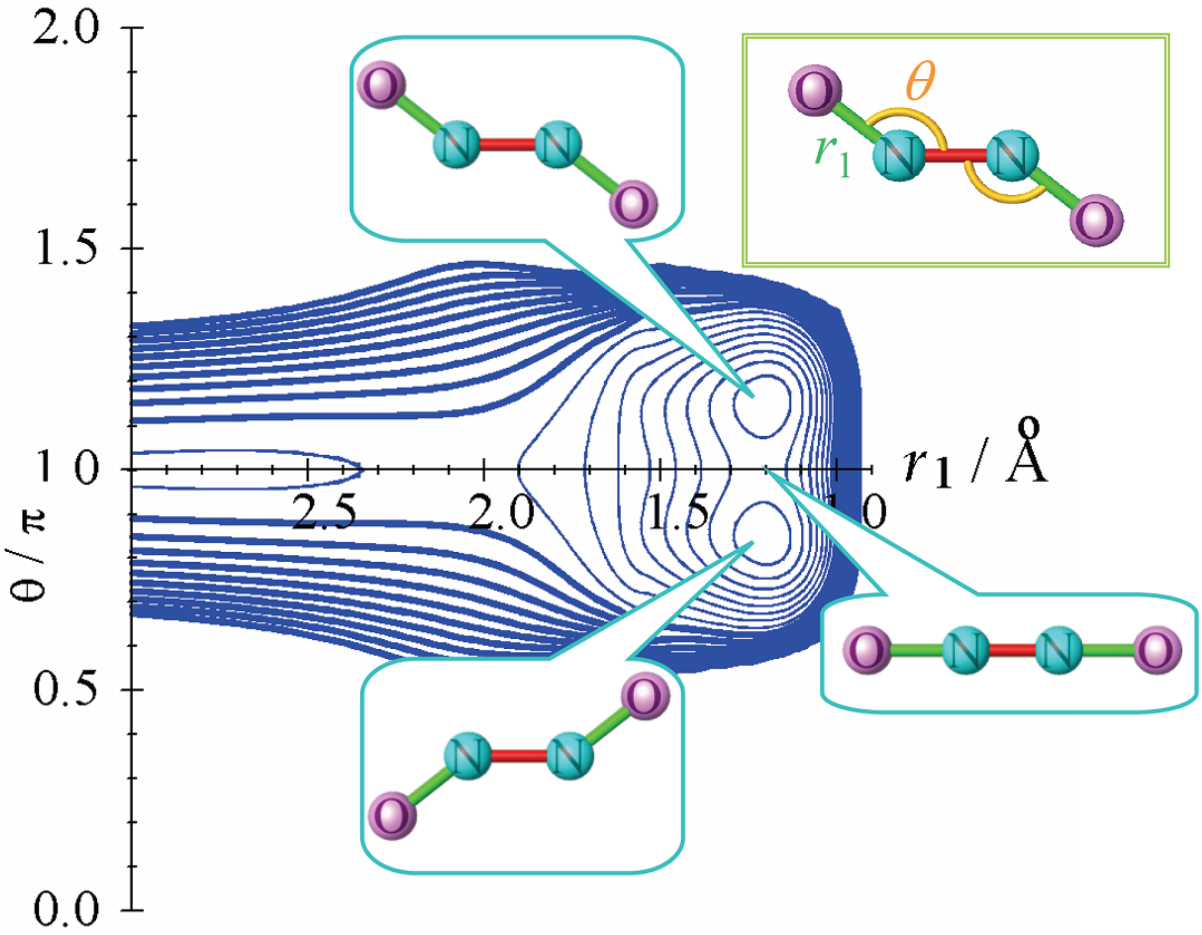

Figure 4.3: A contour plot of the potential as a function of the O-N distance r_1 (the vertical axis) and the bond angle $\theta = \angle\mathrm{ONN'} = \angle\mathrm{NN'O'}$ (the horizontal axis). Contours are spaced with 0.3 kJ/mol. Thin (thick) lines denote the value of the potential lower (higher) than that of the reactant $\mathrm{O}(^1\mathrm{D}) + \mathrm{N_2O}$. The left part of the figure corresponds to the reactant. The N-N′ and N′-O′ distances are fixed to 1.14 Å and 1.18 Å, respectively, which correspond to the equilibrium values at the reactants ($\mathrm{O} + \mathrm{NN'O'}$). The two minima correspond to the *trans*-minima (Tm) and the saddle point between them corresponds to the collinear saddle point (Is).

the system is in the vicinity of the saddle point, where the NHIM exists. The other trajectories of Path 1, that is, the trajectories with $\psi \neq 0$ start with near-collinear configurations ($\chi_1 \approx \pi$, $\chi_2 \approx 0$). After they pass by the regions near the collinear saddle, they fall into *trans*-type configurations ($\chi_1 < \pi$, $\chi_2 < 0$). Thus, in the early stage of the reaction, that is, when the system is in near-collinear configurations, the motion can be well approximated by the motion for $\psi = 0$.

4.2.2 Taylor expansion of the Hamiltonian around the collinear saddle point

Here we perform the Taylor expansion of the Hamiltonian (4.6) around the collinear saddle point (Is). This saddle point connects two *trans*-shaped minima (Tm):

$$\mathrm{O}\diagdown\mathrm{N}-\mathrm{N}\diagdown\mathrm{O} \;\leftrightharpoons\; \mathrm{O}\diagup\mathrm{N}-\mathrm{N}\diagup\mathrm{O}. \tag{4.7}$$

These two minimum configurations can be distinguished from each other in the planar system, although only one of them is shown in Fig. 3.2. Figure 4.3 shows the contour plot of the potential as a function of the O-N distance (r_1) and the bond angle $\angle\mathrm{ONN}'$ with the system restricted to *trans* geometries. As was shown in Chap. 3, trajectories go downhill along a bath mode direction of Is until they pass by the region near Is, and then fall into either Tm following the reactive mode at Is.

After the polynomial expansion up to the nth order, the potential takes the following form:

$$\begin{aligned} V &\approx V^{(n)} \\ &= V^{\mathrm{st}} + \sum_{2\le\sum_\ell j_\ell\le n} v_{\boldsymbol{j}}(\delta r_0)^{j_1}(\delta r_1)^{j_2}(\delta r_2)^{j_3}(\delta\chi_1)^{j_4}(\delta\chi_2)^{j_5}. \end{aligned} \tag{4.8}$$

Here, $V^{(n)}$ is the nth order approximation to the potential energy V. The suffix "st" means the potential energy at the stationary point, δ means the deviation from the value at the stationary point. The components of the integer vector $\boldsymbol{j} = (j_1, j_2, j_3, j_4, j_5)$ are the exponents in the polynomial expansion. $v_{\boldsymbol{j}}$'s are the expansion coefficients. In Eq. (4.8), the summation in j_ℓ covers all the zero or positive values of j_ℓ satisfying $2 \le \sum_{\ell=1}^{5} j_\ell \le n$. Here, we have calculated the expansion coefficients up to fourth-order. To obtain the expansion coefficients, we calculated the Lagrange's interpolation polynomial[62] with potential energy values at grid points around Is, while the analytic expansion form for the kinetic term can be obtained straightforwardly.

In the lower panels of Fig. 4.2(a)-(d), the error $\Delta V^{(n)} = V^{(n)} - V$ of the nth order polynomial approximation for the potential is shown for each initial condition. If the error is small, it means that the system is in the vicinity of the saddle point. In order to judge whether the error is small or not, it must be compared with the typical energy per one degree of freedom, which is of the order of 10^{-19} J for this system. For the trajectory of $\psi = 0$ [Fig. 4.2(a)], the error $\Delta V^{(4)}$ is one order of magnitude smaller than this value in the time range of $t \approx$280-305 fs. For $\psi = 5^\circ$ and 10°, the time range for $\Delta V^{(4)} \lesssim 10^{-20}$ is $t \approx$283-293 fs, and $t \approx$287-291 fs, respectively. Thus, the trajectories with $\psi \le 10^\circ$ come sufficiently close to the collinear saddle point. The

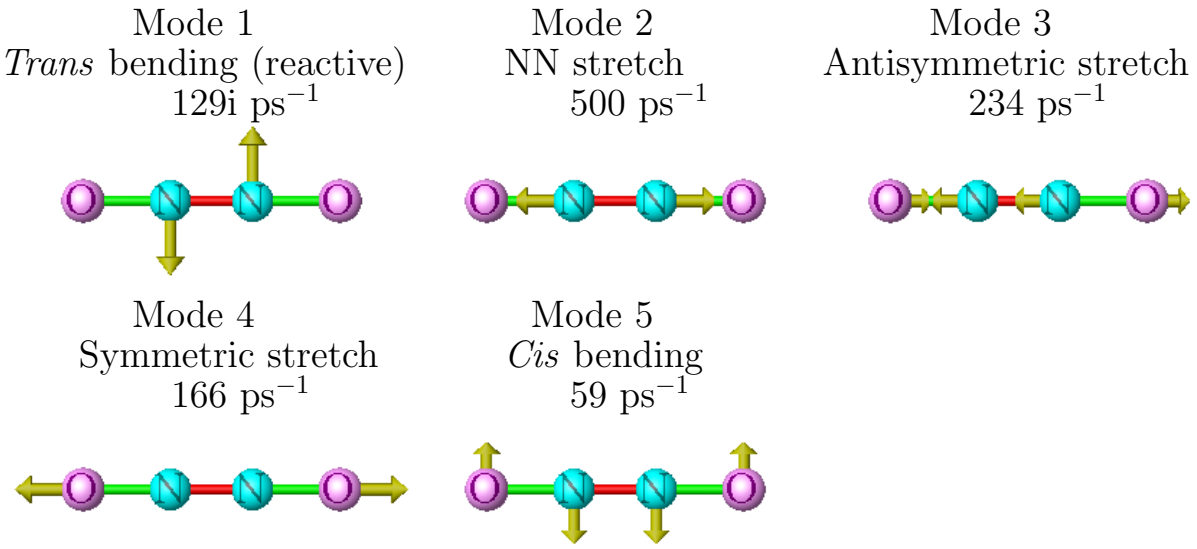

Figure 4.4: Normal modes at the collinear saddle point.

trajectories with $\psi \leq 10°$ cover 2/3 of the whole Path 1 trajectories, since the trajectories of Path 1 cover ψ = 0-15° as stated in Sec. 4.2.1. This means that a significant proportion of the Path 1 trajectories approach the collinear saddle point. Moreover, the excitation of the old NO, r_2, begins when the system comes close to the saddle point. This is revealed by the fact that the excitation of r_2 (i.e., the vibration of the old NO) starts when the errors for $\Delta V^{(4)}$ are small (i.e., when the system is close to the collinear saddle Is). These facts validate the analysis of the collinear saddle for the purpose of understanding the energy exchange from the new to the old NO vibration. Thus, we focus below on the dynamics in the vicinity of Is.

4.2.3 Normal form calculation

Here we perform the NF calculation on the fourth-order PES [Eq. (4.8)]. First, by diagonalizing the harmonic part of the Hamiltonian obtained by the Taylor expansion at Is, we transform the Jacobi coordinates to normal mode coordinates $q_1^{\mathrm{r}}, \ldots, q_5^{\mathrm{r}}$, which are expressed as linear combinations of the original Jacobi coordinates

$$q_\ell^{\mathrm{r}} = c_{\ell,1}\delta r_0 + c_{\ell,2}\delta r_1 + c_{\ell,3}\delta r_2 + c_{\ell,4}\delta\chi_1 + c_{\ell,5}\delta\chi_2, \tag{4.9}$$

where $c_{\ell,m}$ ($\ell, m = 1, \ldots, 5$) are the coefficients of the linear transformation. Thus the quadratic part of the Hamiltonian becomes

$$\begin{aligned} H =& \frac{\lambda}{2}\left\{\left(p_1^{\mathrm{r}}\right)^2 - \left(q_1^{\mathrm{r}}\right)^2\right\} + \sum_{\ell=2}^{5} \frac{\omega_\ell}{2}\left\{\left(p_\ell^{\mathrm{r}}\right)^2 + \left(q_\ell^{\mathrm{r}}\right)^2\right\} \\ &+ \sum_{\sum_\ell (j_\ell + k_\ell) \geq 3} a^{\mathrm{r}}_{\boldsymbol{jk}} \prod_{\ell=1}^{5} \left(q_\ell^{\mathrm{r}}\right)^{j_\ell} \left(p_\ell^{\mathrm{r}}\right)^{k_\ell} . \end{aligned} \tag{4.10}$$

In this equation, $i\lambda$ is the imaginary frequency of the reactive mode, ω_ℓ's ($\ell = 2, \ldots, 5$) are the (real) frequencies of the bath modes, and p_ℓ^{r}'s ($\ell = 1, \ldots, 5$) are the conjugate momenta of q_ℓ^{r}'s. The integer vectors $\boldsymbol{j} = (j_1, j_2, j_3, j_4, j_5)$ and $\boldsymbol{k} = (k_1, k_2, k_3, k_4, k_5)$ denote the set of exponents of q_ℓ^{r}'s and p_ℓ^{r}'s, and $a^{\mathrm{r}}_{\boldsymbol{jk}}$'s are the coefficients in the polynomial expression. We have defined mode 1 as the reactive mode and the bath modes are numbered in the decreasing order of their frequencies. The displacements and the frequencies of the normal modes at the collinear saddle point are shown in Fig. 4.4. We further introduce the following coordinates (complex for the bath modes) for convenience in the later calculation:

$$q_1^{\mathrm{c}} = \frac{q_1^{\mathrm{r}} + p_1^{\mathrm{r}}}{2^{1/2}}, \qquad p_1^{\mathrm{c}} = \frac{p_1^{\mathrm{r}} - q_1^{\mathrm{r}}}{2^{1/2}}, \tag{4.11}$$

$$q_\ell^{\mathrm{c}} = \frac{q_\ell^{\mathrm{r}} - \mathrm{i}p_\ell^{\mathrm{r}}}{2^{1/2}}, \qquad p_\ell^{\mathrm{c}} = \frac{p_\ell^{\mathrm{r}} - \mathrm{i}q_\ell^{\mathrm{r}}}{2^{1/2}}, \qquad (\ell = 2, \ldots, 5). \tag{4.12}$$

In these coordinates, the Hamiltonian becomes

$$\begin{aligned} H =& \lambda q_1^{\mathrm{c}} p_1^{\mathrm{c}} + \sum_{\ell=2}^{5} \mathrm{i}\omega_\ell q_\ell^{\mathrm{c}} p_\ell^{\mathrm{c}} \\ &+ \sum_{\sum_\ell (j_\ell + k_\ell) \geq 3} a^{\mathrm{c}}_{\boldsymbol{jk}} \prod_{\ell=1}^{5} \left(q_\ell^{\mathrm{c}}\right)^{j_\ell} \left(p_\ell^{\mathrm{c}}\right)^{k_\ell} , \end{aligned} \tag{4.13}$$

where the coefficients $a^{\mathrm{c}}_{\boldsymbol{jk}}$'s are calculated by substituting Eqs. (4.11) and (4.12) into Eq. (4.10). The action variables for the harmonic approximation are defined as follows:

$$I_1 = q_1^{\mathrm{c}} p_1^{\mathrm{c}} = \frac{1}{2}\left\{\left(p_1^{\mathrm{r}}\right)^2 - \left(q_1^{\mathrm{r}}\right)^2\right\}, \tag{4.14}$$

$$I_\ell = \mathrm{i}q_\ell^{\mathrm{c}} p_\ell^{\mathrm{c}} = \frac{1}{2}\left\{\left(p_\ell^{\mathrm{r}}\right)^2 + \left(q_\ell^{\mathrm{r}}\right)^2\right\}, \qquad (\ell = 2, \ldots, 5). \tag{4.15}$$

After the above prescription, we transform the Hamiltonian using a new set of variables $(\bar{\boldsymbol{q}}^{\mathrm{c}}, \bar{\boldsymbol{p}}^{\mathrm{c}})$, which are called NF coordinates, to reduce the number of the coupling terms in the Hamiltonian when expressed in these new coordinates. This transformation is constructed as

a perturbation from the original variables $(\boldsymbol{q}^{\mathrm{c}}, \boldsymbol{p}^{\mathrm{c}})$ and expressed in polynomial series:

$$\bar{q}_m^{\mathrm{c}} = q_m^{\mathrm{c}} + \sum_{\sum_\ell (j_\ell + k_\ell) \geq 3} f_{m,\boldsymbol{jk}}^{\mathrm{c}} \prod_{\ell=1}^{5} (q_\ell^{\mathrm{c}})^{j_\ell} (p_\ell^{\mathrm{c}})^{k_\ell}, \tag{4.16}$$

$$\bar{p}_m^{\mathrm{c}} = p_m^{\mathrm{c}} + \sum_{\sum_\ell (j_\ell + k_\ell) \geq 3} g_{m,\boldsymbol{jk}}^{\mathrm{c}} \prod_{\ell=1}^{5} (q_\ell^{\mathrm{c}})^{j_\ell} (p_\ell^{\mathrm{c}})^{k_\ell}, \tag{4.17}$$

where $f_{m,\boldsymbol{jk}}^{\mathrm{c}}$'s and $g_{m,\boldsymbol{jk}}^{\mathrm{c}}$'s are the coefficients of the polynomials. Real-valued NF coordinates $(\bar{\boldsymbol{q}}^{\mathrm{r}}, \bar{\boldsymbol{p}}^{\mathrm{r}})$ are defined by

$$\bar{q}_1^{\mathrm{r}} = \frac{\bar{q}_1^{\mathrm{c}} - \bar{p}_1^{\mathrm{c}}}{2^{1/2}}, \qquad \bar{p}_1^{\mathrm{r}} = \frac{\bar{p}_1^{\mathrm{c}} + \bar{q}_1^{\mathrm{c}}}{2^{1/2}}, \tag{4.18}$$

$$\bar{q}_\ell^{\mathrm{r}} = \frac{\bar{q}_\ell^{\mathrm{c}} + \mathrm{i}\bar{p}_\ell^{\mathrm{c}}}{2^{1/2}}, \qquad \bar{p}_\ell^{\mathrm{r}} = \frac{\bar{p}_\ell^{\mathrm{c}} + \mathrm{i}\bar{q}_\ell^{\mathrm{c}}}{2^{1/2}}, \qquad (\ell = 2, \ldots, 5). \tag{4.19}$$

When we put Eqs. (4.11), (4.12), (4.18), and (4.19) into Eqs. (4.16) and (4.17), we obtain the relations of real-valued coordinates:

$$\bar{q}_m^{\mathrm{r}} = q_m^{\mathrm{r}} + \sum_{\sum_\ell (j_\ell + k_\ell) \geq 3} f_{m,\boldsymbol{jk}}^{\mathrm{r}} \prod_{\ell=1}^{5} (q_\ell^{\mathrm{r}})^{j_\ell} (p_\ell^{\mathrm{r}})^{k_\ell}, \tag{4.20}$$

$$\bar{p}_m^{\mathrm{r}} = p_m^{\mathrm{r}} + \sum_{\sum_\ell (j_\ell + k_\ell) \geq 3} g_{m,\boldsymbol{jk}}^{\mathrm{r}} \prod_{\ell=1}^{5} (q_\ell^{\mathrm{r}})^{j_\ell} (p_\ell^{\mathrm{r}})^{k_\ell}, \tag{4.21}$$

where the coefficients $f_{\ell,\boldsymbol{jk}}^{\mathrm{r}}$'s and $g_{\ell,\boldsymbol{jk}}^{\mathrm{r}}$'s can be calculated from $f_{\ell,\boldsymbol{jk}}^{\mathrm{c}}$'s and $g_{\ell,\boldsymbol{jk}}^{\mathrm{c}}$'s. The summations are taken only for the terms with even $|\boldsymbol{k}| \equiv \sum_{\ell=1}^{5} k_\ell$ in Eq. (4.20) and odd $|\boldsymbol{k}|$ in Eq. (4.21) because of time-reversal symmetry. Details of the NF transformation are given in Sec. 4.6 and also in literatures.[42–44, 48]

After the NF transformation, the Hamiltonian is expressed in the polynomial of $(\bar{\boldsymbol{q}}^{\mathrm{c}}, \bar{\boldsymbol{p}}^{\mathrm{c}})$. This new Hamiltonian is denoted as $\bar{H}(\bar{\boldsymbol{q}}^{\mathrm{c}}, \bar{\boldsymbol{p}}^{\mathrm{c}})$. In the Hamiltonian, the off-diagonal terms, that is, terms with different powers of $\bar{q}_\ell^{\mathrm{c}}$ and $\bar{p}_\ell^{\mathrm{c}}$, denote couplings among the modes. This can be seen as follows. If all the off-diagonal terms are eliminated from the Hamiltonian through the NF transformation, that is, if the transformed Hamiltonian $\bar{H}$ takes the following form,

$$\begin{aligned} &\bar{H}(\bar{\boldsymbol{q}}^{\mathrm{c}}, \bar{\boldsymbol{p}}^{\mathrm{c}}) \\ &= \lambda \bar{q}_1^{\mathrm{c}} \bar{p}_1^{\mathrm{c}} + \sum_{\ell=2}^{5} \mathrm{i}\omega_\ell \bar{q}_\ell^{\mathrm{c}} \bar{p}_\ell^{\mathrm{c}} + \sum_{\sum_\ell j_\ell \geq 2} \bar{a}_{\boldsymbol{j}}^{\mathrm{c}} \prod_{\ell=1}^{5} (\bar{q}_\ell^{\mathrm{c}} \bar{p}_\ell^{\mathrm{c}})^{j_\ell}, \end{aligned} \tag{4.22}$$

where $\bar{a}_{\boldsymbol{j}}^{\mathrm{c}}$'s are the coefficients of the polynomial, then all of the new action variables $\bar{I}_1 = \bar{q}_1^{\mathrm{c}} \bar{p}_1^{\mathrm{c}}$, and $\bar{I}_\ell = \mathrm{i}\bar{q}_\ell^{\mathrm{c}} \bar{p}_\ell^{\mathrm{c}}$ $(\ell = 2, \ldots, 5)$ are constants of motion and the system is fully integrable. The

Hamiltonian $\bar{H}$ of the form (4.22) is called a full normal form (corresponding to a classical analog of Dunham Hamiltonian in molecular spectroscopy). In many occasions, however, elimination of certain coupling terms results in divergence of the perturbation series and thus the transformation cannot be constructed. Such coupling terms should be included in the NF Hamiltonian $\bar{H}$. Which terms can be eliminated and which terms should be included in $\bar{H}$ must be determined based on convergence of the transformed Hamiltonian.

In this chapter we use the energy error[45] $\Delta E^{(n)} = |\bar{H}^{(n)} - H|$ as a criterion of the convergence, where $\bar{H}^{(n)}$ is the NF Hamiltonian up to the nth order and H is the true Hamiltonian. We have found that the terms listed in Table 4.1 should be kept in the transformed Hamiltonian, since their elimination results in a larger error $\Delta E^{(4)}$ than the error $\Delta E^{(2)}$ of the harmonic approximation. The transformed Hamiltonian takes the following form:

$$\begin{aligned}\bar{H} =& \lambda \bar{q}_1^{\mathrm{c}} \bar{p}_1^{\mathrm{c}} + \sum_{\ell=2}^{5} \mathrm{i}\omega_\ell \bar{q}_\ell^{\mathrm{c}} \bar{p}_\ell^{\mathrm{c}} + \sum_{\sum_\ell j_\ell \geq 2} \bar{a}^{\mathrm{c}}_{\boldsymbol{j}} \prod_{\ell=1}^{5} (\bar{q}_\ell^{\mathrm{c}} \bar{p}_\ell^{\mathrm{c}})^{j_\ell} \\ &+ \sum_{\boldsymbol{d}} \sum_{(\boldsymbol{j}-\boldsymbol{k}) \propto \boldsymbol{d}} \bar{a}^{\mathrm{c}}_{\boldsymbol{jk}} \prod_{\ell=1}^{5} (\bar{q}_\ell^{\mathrm{c}})^{j_\ell} (\bar{p}_\ell^{\mathrm{c}})^{k_\ell} , \end{aligned} \tag{4.23}$$

where $\bar{a}^{\mathrm{c}}_{\boldsymbol{j}}$'s and $\bar{a}^{\mathrm{c}}_{\boldsymbol{jk}}$'s are the coefficients of the diagonal and the off-diagonal terms, respectively, and the integer vector $\boldsymbol{d}$ covers all the terms listed in Table 4.1. The Hamiltonian of the form (4.23) is called Partial Normal Form (PNF) in contrast to the full NF (4.22). Note that, even with the off-diagonal terms, the form (4.23) is still much simpler than the original form (4.13). Namely, a fourth-order polynomial with 10 variables has 1001 terms, whereas there are only 12 types (listed in Table 4.1) of coupling terms in Eq. (4.23).

In observing the terms listed in Table 4.1, we note the following facts. First, all of the terms listed in Table 4.1 have zero in their first component, which means that the PNF Hamiltonian contains only those terms with $j_1 = k_1$. Therefore $\bar{I}_1 = \bar{q}_1^{\mathrm{c}} \bar{p}_1^{\mathrm{c}}$ is a local constant of motion. This means that the motion along mode 1 is separable from the others. Similar situations are found in former studies.[36–44,46,47,98] It is attributed to the fact that there can be no resonance between imaginary and real frequencies.[99] Second, terms which contain both positive and negative $(j_\ell - k_\ell)$ like $0:1:0:-3:0$ can be understood in view of "resonance" effect. Namely, the harmonic frequencies for mode 2 and 4 are nearly in the ratio of 3:1 and thus the terms with $(j_2 - k_2) : (j_4 - k_4) = 1 : -3$ can give rise to small divisors in the NF process. Therefore we excluded the corresponding terms from the generating function (see Sec. 4.6). Third, Table 4.1 also contains those terms for which all $(j_\ell - k_\ell)$'s are nonnegative, such as $0:0:1:0:0$ and $0:0:2:1:0$. These are the terms which are not of the "resonance" type but cannot be

Table 4.1: Types of the terms which cannot be eliminated from the NF Hamiltonian. j_ℓ and k_ℓ are the exponents of $\bar{q}_\ell^{\rm c}$ and $\bar{p}_\ell^{\rm c}$ in $\bar{H}$ [See Eq. (4.23)].

(j_1-k_1) :	(j_2-k_2) :	(j_3-k_3) :	(j_4-k_4) :	(j_5-k_5)
0	1	0	-3	0
0	0	1	-1	0
0	1	-1	-2	0
0	0	0	0	2
0	0	0	2	-2
0	0	1	0	0
0	0	1	1	0
0	1	-2	0	0
0	0	1	-2	0
0	0	0	1	0
0	0	2	-1	0
0	0	2	1	0

eliminated from the PNF Hamiltonian. To the best of our knowledge, no literature has given an explanation to the existence of such terms. We consider that the values of the actions for mode 3 and 4 are so large that they cannot be eliminated by perturbation.

4.3 ANALYSES OF THE DYNAMICS

4.3.1 Evaluation of the couplings

First, we analyze the time development of the vibrational energy of each of the PNF coordinates. The upper panels of Fig. 4.5 show the values of $\omega_\ell \bar{I}_\ell$, that is, a rough estimation of the vibrational energy of each mode, calculated along the trajectories shown in Fig. 4.2. The lower panels of the same figure show the energy errors of the harmonic (thin solid lines) and the PNF (thick solid lines) Hamiltonian, respectively. There the trajectories are calculated by using the original Hamiltonian as in Fig. 4.2. Then, the PNF actions $\bar{I}_\ell = \bar{q}_\ell^{\rm c}\bar{p}_\ell^{\rm c}$ and the PNF Hamiltonian $\bar{H}(\bar{\boldsymbol{q}}^{\rm c}, \bar{\boldsymbol{p}}^{\rm c})$ are calculated from original Jacobi coordinates $(r_0, r_1, r_2, \chi_1, \chi_2)$ using the transformation given by Eqs. (4.9), (4.11), (4.12), (4.16), and (4.17). The PNF Hamiltonian and actions are calculated up to the fourth order of polynomial. Here we can see that, for $\psi \leq 10°$, the PNF calculation shows convergence for the time region in which trajectories are in the vicinity of the saddle point (when compared with Fig. 4.2). Moreover, the action value for mode 1 is nearly constant, as can be predicted from the form of the PNF Hamiltonian

(4.23) and Table 4.1. On the other hand, the actions of mode 3 and 4 decrease at earlier times (e.g., 280-290 fs for $\bar{I}_3$ and 280-295 fs for $\bar{I}_4$ at $\psi = 0$) with nonconstant decrease rates and increase at later times (e.g., $t > 290$ fs for $\bar{I}_3$ and $t > 295$ fs for $\bar{I}_4$ at $\psi = 0$) . Their time evolutions cannot be simply interpreted based on resonances (between modes 3 and 4), which have the effect of decreasing some of the actions and increasing others at the same time. On the contrary, the simultaneous decrease of $\bar{I}_3$ and $\bar{I}_4$ implies that non-resonance type terms, that is, the terms for which all $(j_\ell - k_\ell)$'s are nonnegative in Table 4.1, play important roles for the changes of these actions.

Now, we will discuss, in terms of the NHIM, that only a part of the degrees of freedom contribute to the efficient energy transfer, and construct an effective Hamiltonian to describe the basic mechanism of the energy transfer. The NHIM is defined in terms of $(\bar{\boldsymbol{q}}^{\mathrm{c}}, \bar{\boldsymbol{p}}^{\mathrm{c}})$ as

$$\begin{aligned}\mathcal{M}_{\mathrm{NHIM}} =&\{(\bar{p}_1^c, \cdots, \bar{p}_5^c, \bar{q}_1^c, \cdots, \bar{q}_5^c) \mid \bar{p}_1^c = \bar{q}_1^c = 0; \\ &\bar{H}(\bar{I}_1 = 0, \bar{q}_2^{\mathrm{c}}, \bar{q}_3^{\mathrm{c}}, \bar{q}_4^{\mathrm{c}}, \bar{q}_5^{\mathrm{c}}, \bar{p}_2^{\mathrm{c}}, \bar{p}_3^{\mathrm{c}}, \bar{p}_4^{\mathrm{c}}, \bar{p}_5^{\mathrm{c}}) = E\},\end{aligned} \tag{4.24}$$

at a given energy E. Because the reactive degree of freedom is decoupled from the bath space in the $(\bar{\boldsymbol{q}}^{\mathrm{c}}, \bar{\boldsymbol{p}}^{\mathrm{c}})$ coordinate system, the NHIM forms an invariant set. Normal hyperbolicity implies that the degree of freedom normal to it (i.e., the reactive mode) is hyperbolic while the degrees of freedom tangent to it (i.e., the bath modes) are elliptic, or in general, are weakly hyperbolic compared with the normal hyperbolicity.

The system approaches the collinear saddle (Is) in a perpendicular direction to the reactive degree of freedom at Is before falling into one of the two *trans*-shaped minima (see Fig. 4.3). Therefore, the dynamics near Is, where PNF theory is valid, can be well represented as that on the NHIM. More precisely, the "approaching" trajectory with $\psi = 0$ form an invariant set with the constantly zero actions of modes 1 and 5, which are "bending" motions (See Fig. 4.4). This invariant set of the collinear configurations given by $\bar{q}_1^c = \bar{p}_1^c = \bar{q}_5^c = \bar{p}_5^c = 0$ is a subset of the NHIM ($\bar{q}_1^c = \bar{p}_1^c = 0$), which exists in the vicinity of the saddle, where PNF works. Note that the invariance of the collinear configurations is due to their symmetry whereas that of the NHIM is due to the topological feature of rank-1 saddle where no resonance takes place among one reactive mode and the bath modes.

Note that the trajectories with $\psi \leq 10^\circ$ have qualitatively similar properties to each other as seen in the plots of the Jacobi coordinates (Fig. 4.2) and the PNF actions (Fig. 4.5). This can be understood based on the property of the NHIM as follows. The behavior of trajectories near the NHIM is decomposed into the motion along it and that normal to it. Then, the similarity of the trajectories with $\psi \leq 10^\circ$ is attributed to this decomposition of the dynamics near the

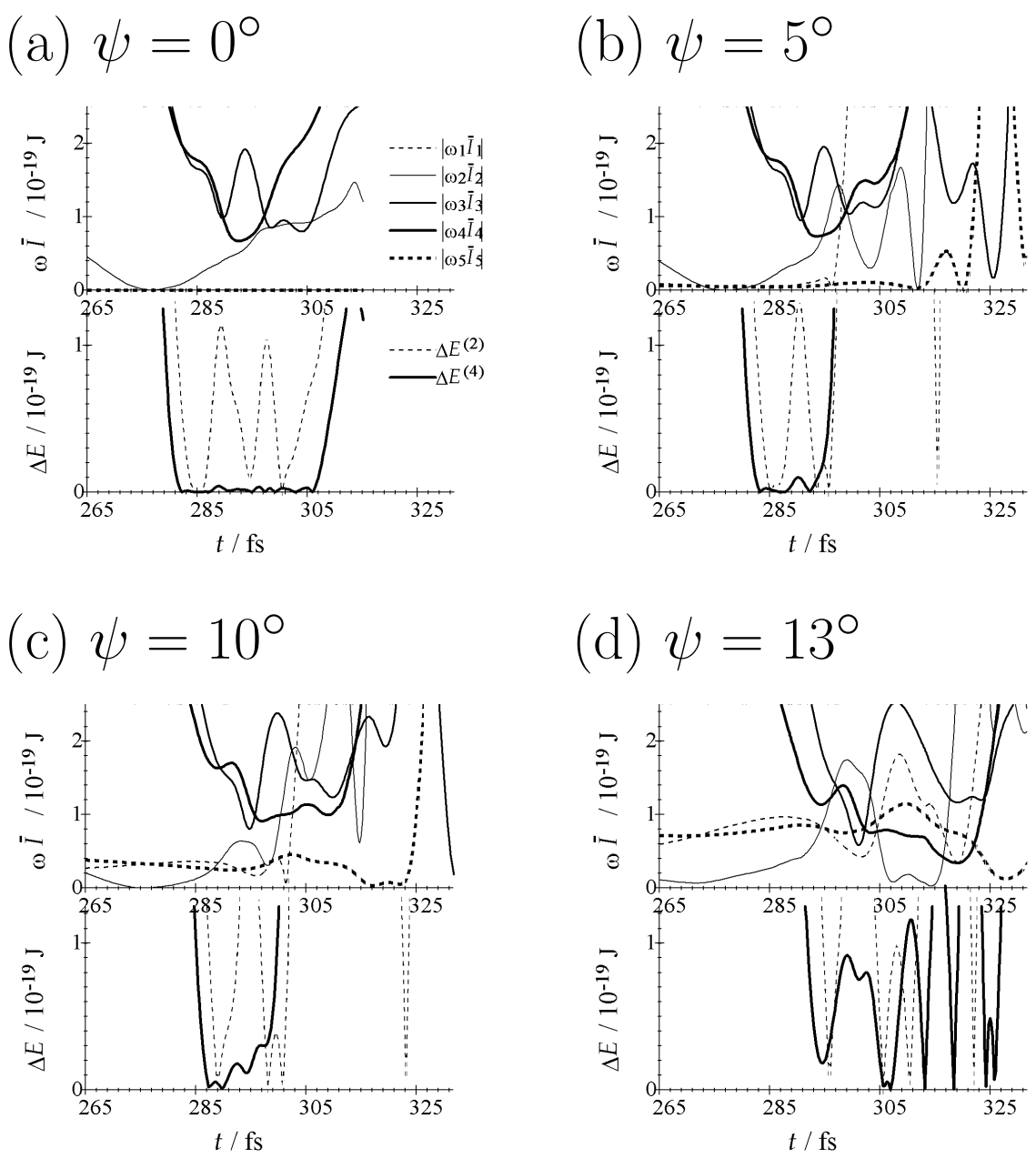

Figure 4.5: Results of PNF calculation shown for four initial conditions which are the same as Fig. 4.2. Upper panels: Time evolution of the action variables multiplied by the corresponding harmonic frequencies. The values for mode 1, 2, 3, 4, and 5 are shown by thin dotted, thin solid, medium solid, thick solid, and thick dotted lines, respectively. Lower panels: Energy errors. Thin solid line depicts the difference $\Delta E^{(2)}$ between the true Hamiltonian and the harmonic approximation. Thick solid line depicts the difference $\Delta E^{(4)}$ between the true Hamiltonian and fourth-order PNF Hamiltonian.

NHIM. We can judge whether they stay near the NHIM or not by Fig. 4.2 and Fig. 4.5, and confirm that these trajectories behave similarly to the one with $\psi = 0$ near the NHIM. Thus, the motion of the bath modes, which includes the vibrations of the new and old NO bonds, can be understood by the motions in the NHIM. Therefore, we now focus on the case of $\psi = 0$ to extract the underlying mechanism of why energy transfer takes place quite efficiently despite of the lack of the long residence inside the potential well.

Based on the above discussions, we can treat the system locally as an effective 3-DOF (degrees of freedom) system with an effective Hamiltonian given by

$$\begin{aligned} &H^{\rm eff}(\bar{q}_2^{\rm c}, \bar{q}_3^{\rm c}, \bar{q}_4^{\rm c}, \bar{p}_2^{\rm c}, \bar{p}_3^{\rm c}, \bar{p}_4^{\rm c}) = \\ &\bar{H}(\bar{q}_1^{\rm c} = 0, \bar{q}_2^{\rm c}, \bar{q}_3^{\rm c}, \bar{q}_4^{\rm c}, \bar{q}_5^{\rm c} = 0, \bar{p}_1^{\rm c} = 0, \bar{p}_2^{\rm c}, \bar{p}_3^{\rm c}, \bar{p}_4^{\rm c}, \bar{p}_5^{\rm c} = 0), \end{aligned} \tag{4.25}$$

when the system is in the neighborhood of the collinear saddle Is. The dynamics of $H^{\rm eff}$ takes place in a subspace of the NHIM.

We further simplify the above Hamiltonian by taking into account the coupling terms listed in Table 4.1. In order to assess their effects, we have plotted, in Fig. 4.6, the values of these terms along the trajectory of $\psi = 0$. Here the non-resonance type terms which include modes 3 and/or 4, such as "0 : 0 : 1 : 0 : 0," "0 : 0 : 2 : 1 : 0," *etc*, show large values. On the other hand, among the coupling terms including mode 2, only the "0 : 1 : -2 : 0 : 0" term has nonnegligible value, but it is still smaller than the coupling terms between modes 3 and 4. Thus, modes 3 and 4 have large anharmonicity and are strongly coupled with each other, whereas mode 2 is coupled only with mode 3 through one term. Therefore we can gain more insight into the dynamics by making the following separation of the Hamiltonian:

$$\begin{aligned} &H^{\rm eff}(\bar{q}_2^{\rm c}, \bar{q}_3^{\rm c}, \bar{q}_4^{\rm c}, \bar{p}_2^{\rm c}, \bar{p}_3^{\rm c}, \bar{p}_4^{\rm c}) \\ =&\bar{H}_{34}(\bar{q}_3^{\rm c}, \bar{q}_4^{\rm c}, \bar{p}_3^{\rm c}, \bar{p}_4^{\rm c}) + \omega_2 \bar{I}_2 + \sum \bar{a}^{\rm c}_{\boldsymbol{jk}} \prod_{\ell=2}^{4} \left(\bar{q}_\ell^{\rm c}\right)^{j_\ell} \left(\bar{p}_\ell^{\rm c}\right)^{k_\ell}, \end{aligned} \tag{4.26}$$

where

$$\bar{H}_{34}(\bar{q}_3^{\rm c}, \bar{q}_4^{\rm c}, \bar{p}_3^{\rm c}, \bar{p}_4^{\rm c}) = H^{\rm eff}(\bar{q}_2^{\rm c} = 0, \bar{q}_3^{\rm c}, \bar{q}_4^{\rm c}, \bar{p}_2^{\rm c} = 0, \bar{p}_3^{\rm c}, \bar{p}_4^{\rm c}). \tag{4.27}$$

In Eq. (4.26), the first term can be interpreted as Hamiltonian of a 2-DOF subsystem consisting of modes 3 and 4, the second term is harmonic energy of mode 2, and the third term contains all the other terms which can be interpreted as the coupling between the 2-DOF subsystem and mode 2. Figure 4.7 shows the values of $\bar{H}_{34}$ and $\omega_2 \bar{I}_2$ as functions of time. We have obtained

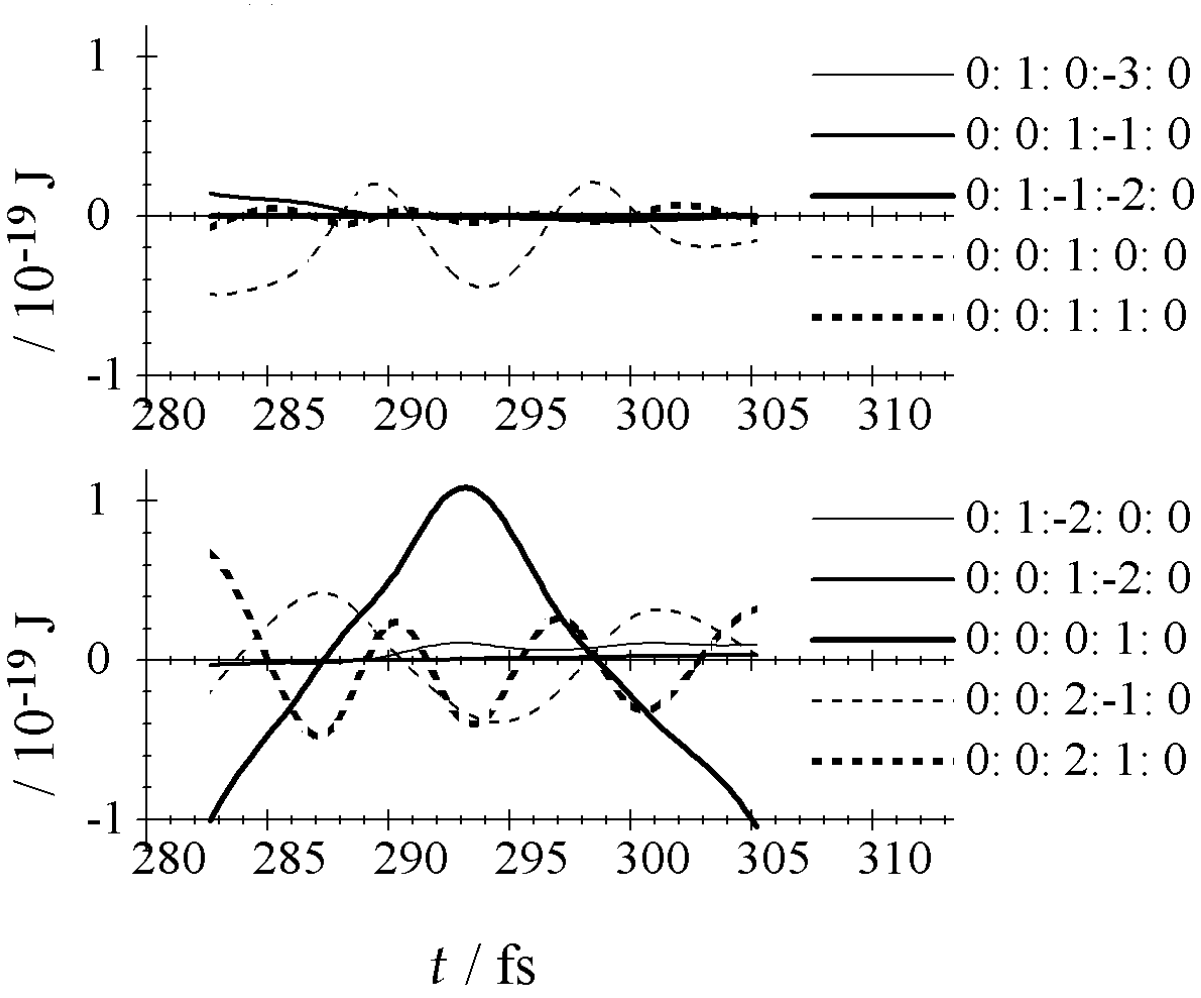

Figure 4.6: Values of the coupling terms in NF Hamiltonian as functions of time calculated for the trajectory with $\psi = 0$.

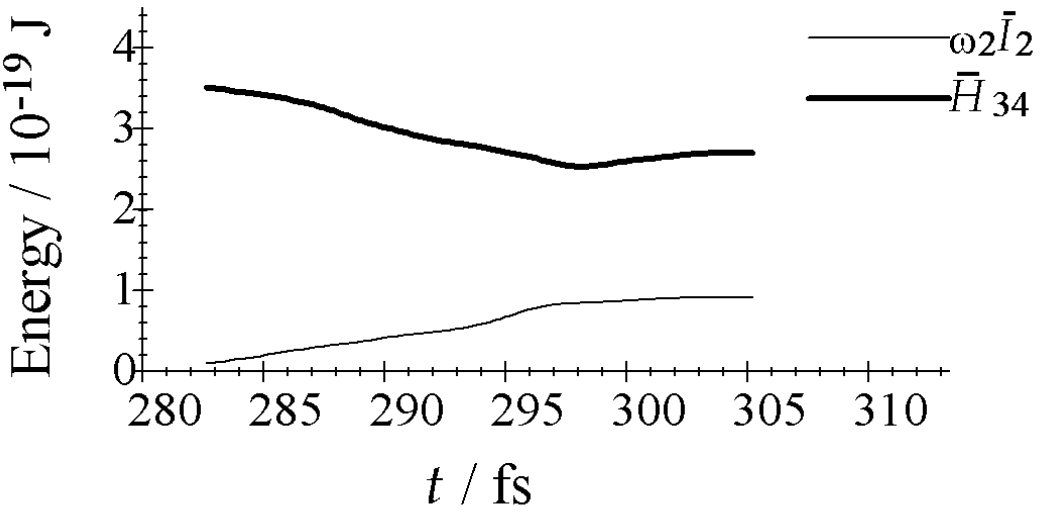

Figure 4.7: Values of the energy $\bar{H}_{34}$ of 2-DOF subsystem and the harmonic energy $\omega_2 \bar{I}_2$ of mode 2 (see text for more detailed definition). They are calculated for the trajectory with $\psi = 0$ and shown as functions of time t.

a monotonic decrease of $\bar{H}_{34}$ in contrast to the increase of $\bar{I}_2$. This is consistent with the idea presented above, that is, the coupling between mode 2 and the 2-DOF subsystem is due to only one resonance, the "0 : 1 : -2 : 0 : 0" term.

Now the dynamics of the system has been decomposed into that of mode 2 and that of the 2-DOF subsystem consisting of modes 3 and 4. In the next subsection, we look deeply into this 2-DOF subsystem.

4.3.2 Dynamics of the 2-DOF subsystem

Figure 4.8(a) shows the Poincaré surface of section (SOS) of the 2-DOF Hamiltonian $\bar{H}_{34}$ for $\bar{q}_4^{\rm r} = 0$, $\bar{p}_4^{\rm r} > 0$ with the horizontal and vertical axes being $\bar{q}_3^{\rm r}$ and $\bar{p}_3^{\rm r}$, respectively. The value of the Hamiltonian $\bar{H}_{34}$, i.e., the energy of these trajectories, is chosen as follows: After calculating the trajectory of $\psi = 0$ by the original Hamiltonian up to $t = 283$ fs, we transform the Jacobi coordinates at $t = 283$ fs by Eqs. (4.9), (4.11), (4.12), (4.16), (4.17), and (4.19), to $(\bar{\boldsymbol{q}}^{\rm r}, \bar{\boldsymbol{p}}^{\rm r})$. The resulting values are indicated in the caption of Fig. 4.8(b). Substituting their values into the Hamiltonian $\bar{H}_{34}$, we obtain $\bar{H}_{34} = 3.5010 \times 10^{-19}$ J relative to the top of the saddle.

In Fig. 4.8(a), we can see the existence of regular tori in the outer region, whereas the inner region shows irregular behavior. To find which region corresponds to the actual reaction trajectories, we have plotted, in Fig. 4.8(b), the SOS for five trajectories. The initial conditions of these five trajectories are chosen as follows. First, we calculate the trajectory with $\psi = 0$ using the original Hamiltonian up to five different times t =283, 290, 295, 300, and 305 fs.

The values of the Jacobi coordinates and their conjugate momenta at these five instances are transformed to the values of $(\bar{\boldsymbol{q}}^{\rm r}, \bar{\boldsymbol{p}}^{\rm r})$ to give the five initial conditions $(\bar{q}_3^{\rm r}, \bar{q}_4^{\rm r}, \bar{p}_3^{\rm r}, \bar{p}_4^{\rm r})$. Then, we perform the 2-DOF trajectory calculations and plot the SOS in Fig. 4.8(b). The five 2-DOF trajectories have different values of $\bar{H}_{34}$ because of the coupling with mode 2. Since the trajectory stays near the saddle in the time interval 283 fs$\lesssim t \lesssim$ 305 fs [see Fig. 4.5(a)], we can see from these plots which part of the section corresponds to the actual reaction trajectories.

In Fig. 4.8(b), the system first appears in the intermediate region between the center and the outermost ellipse. This is because the reaction trajectories start with an elongation of the new NO bond, which corresponds to simultaneous excitation of the symmetric and antisymmetric stretches. At early times, the system is found in the region of regular torus structure. Then the torus shrinks as the time passes, due to the coupling with mode 2, and finally enters into the inner irregular region after $t = 290$ fs. The tori found in the early time period are topologically the same as those of the harmonic case ($(\bar{q}_3^{\rm r})^2 + (\bar{p}_3^{\rm r})^2 =$ const.) although they are distorted. Strictly speaking, their shapes are distorted from the true circle. We should also note that the coordinates used in Fig. 4.8 are the PNF coordinates, whose main parts are the normal mode coordinates but they are not exactly the same. However, bifurcation into the local modes [83–86] or other types of periodic orbits [87–92] does not occur for this system (at least in the region corresponding to the reaction trajectories). This means that the normal mode picture is qualitatively conserved for the reaction trajectories in spite of its high energy. Hereafter, we refer to this motion as "distorted normal mode."

So far we have limited our attention to the trajectory of $\psi = 0$, which is collinear and thus contained in the NHIM. This is based on the idea that the deviation from $\psi = 0$ mainly results in the displacement in the direction of the reactive mode (mode 1), and that it has little effect on the bath mode dynamics. However, its effect on the bath modes is not exactly zero and thus it is worth investigating whether it is really negligible. This is performed by taking the initial value of $(\bar{q}_3^{\rm r}, \bar{q}_4^{\rm r}, \bar{p}_3^{\rm r}, \bar{p}_4^{\rm r})$ from trajectories with $\psi \neq 0$. Figure 4.9 shows similar plots to that in Fig. 4.8(b), where initial values are chosen from the values of the Jacobi coordinates at $t = 285, 290$ fs for $\psi = 5°$, and $t = 290$ fs for $\psi = 10°$, respectively. Here again, we can see the distorted normal mode type structure.

The chaotic motion in the inner region does not appear for these trajectories. This is because their residence times in the vicinity of the saddle point is finite, whereas the collinear trajectory ($\psi = 0$) remains in the NHIM all the time. Their residence times become shorter as their deviation from the NHIM is larger. This is due to the fact that we have narrower time

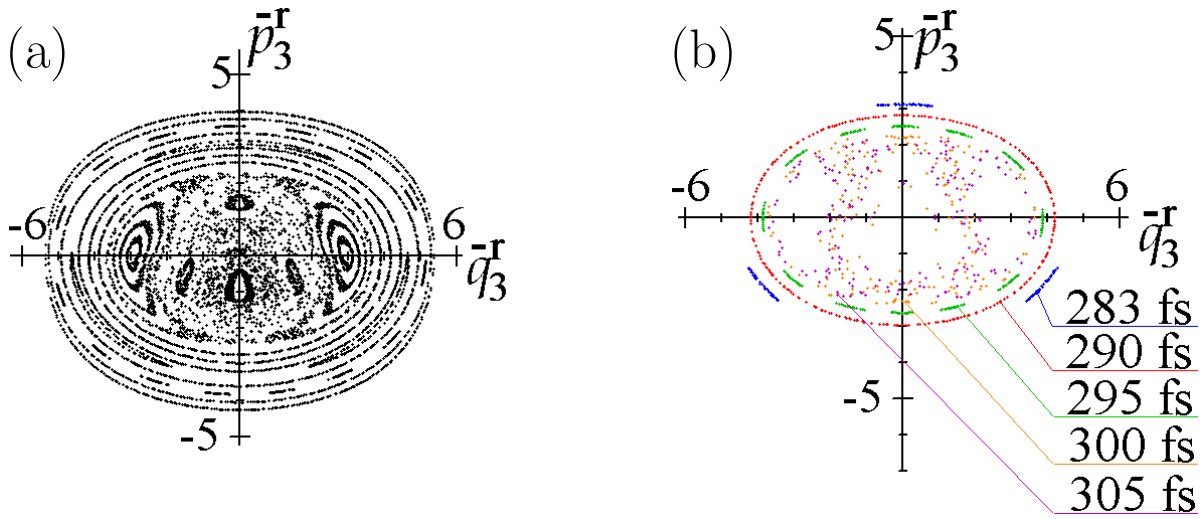

Figure 4.8: Poincaré surface of section for the 2-DOF subsystem consisting of modes 3 and 4 calculated with the polynomial Hamiltonian $\bar{H}_{34}$. (a) Total Poincaré surface of section with $\bar{q}_4^r = 0$ and $\bar{p}_4^r > 0$ plotted with $\bar{q}_3^r$ and $\bar{p}_3^r$. The unit is 10^{-17} kg$^{1/2}$ms$^{-1/2}$. The energy is $\bar{H}_{34} = 3.5010 \times 10^{-19}$ J, which corresponds to the value of $(\bar{q}_3^r, \bar{q}_4^r, \bar{p}_3^r, \bar{p}_4^r)$ at $t = 283$ fs for the actual reaction trajectory with $\psi = 0$. (b) Poincaré surface of section is drawn for five different initial values of $(\bar{q}_3^r, \bar{q}_4^r, \bar{p}_3^r, \bar{p}_4^r)$. Blue:$(\bar{q}_3^r, \bar{q}_4^r, \bar{p}_3^r, \bar{p}_4^r) = (3.70912, -4.12055, 1.39117, -2.40706)$, which corresponds to the values at $t = 283$ fs for $\psi = 0$. Red:$(\bar{q}_3^r, \bar{q}_4^r, \bar{p}_3^r, \bar{p}_4^r) = (-0.74253, -2.24372, -2.84153, 2.42701)$, which corresponds to the values at $t = 290$ fs for $\psi = 0$. Green:$(\bar{q}_3^r, \bar{q}_4^r, \bar{p}_3^r, \bar{p}_4^r) = (-3.51209, 2.00635, 1.34369, 2.30668)$, which corresponds to the values at $t = 295$ fs for $\psi = 0$. Orange:$(\bar{q}_3^r, \bar{q}_4^r, \bar{p}_3^r, \bar{p}_4^r) = (1.57224, 4.38929, 2.35114, -0.30151)$, which corresponds to the values at $t = 300$ fs for $\psi = 0$. Purple:$(\bar{q}_3^r, \bar{q}_4^r, \bar{p}_3^r, \bar{p}_4^r) = (2.51367, 3.27718, -1.11494, -3.95697)$, which corresponds to the value at $t = 305$ fs for $\psi = 0$.

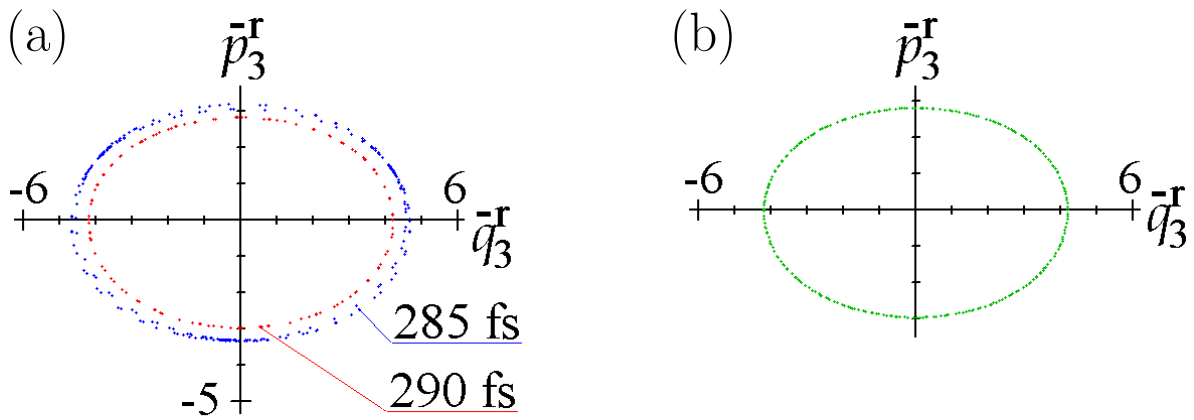

Figure 4.9: Poincaré surface of section for the 2-DOF subsystem consisting of modes 3 and 4 calculated with the polynomial Hamiltonian $\bar{H}_{34}$. The initial values are as follows: (a) Outer ellipse:$(\bar{q}_3^r, \bar{q}_4^r, \bar{p}_3^r, \bar{p}_4^r) = (3.76265, -4.33988, 0.66964, -1.68103)$, which corresponds to the values at $t = 285$ fs for $\psi = 5°$. Inner ellipse: $(\bar{q}_3^r, \bar{q}_4^r, \bar{p}_3^r, \bar{p}_4^r) = (0.78110, -3.21763, -2.81286, 2.02043)$, which corresponds to the values at $t = 290$ fs for $\psi = 5°$. (b) $(\bar{q}_3^r, \bar{q}_4^r, \bar{p}_3^r, \bar{p}_4^r) = (3.65408, -4.39855, 0.38768, -0.78467)$, which corresponds to the value at $t = 290$ fs for $\psi = 10°$.

ranges for convergence of the NF calculations for $0 \leq \psi \lesssim 10°$, such as 283 fs $\lesssim t \lesssim$ 293 fs for $\psi = 5°$, and 287 fs $\lesssim t \lesssim$ 291 fs for $\psi = 10°$ [see Fig. 4.5(a)], respectively.

From Fig. 4.9, we can see that these trajectories do not have enough time to travel into the inner region while being in the vicinity of the saddle. Thus we can conclude that the distorted normal mode picture is not broken by the deviation from $\psi = 0$ and the non-collinear trajectories also have the distorted normal mode structure when they enter into the vicinity of the saddle point.

4.3.3 Mechanism of efficient energy transfer

Basic mechanism of the efficient energy transfer can be obtained using the distorted normal mode picture, which was found in Sec. 4.3.2. Here we propose a "beat" model for the excitation of the old NO vibration as follows: Qualitatively, the symmetric $(\bar{q}_4^r)$ and antisymmetric $(\bar{q}_3^r)$ coordinates can be expressed in the following equations:

$$\bar{q}_4^r \approx q_4^r \sim \frac{\delta r_1 + \delta r_2}{2^{1/2}}, \tag{4.28}$$

$$\bar{q}_3^r \approx q_3^r \sim \frac{\delta r_1 - \delta r_2}{2^{1/2}}, \tag{4.29}$$

where δr_1 and δr_2 are the deviation of the bond length of the new and old NO, respectively, from their equilibrium values. Since the normal mode picture is conserved with a little distortion, the time evolution of $\bar{q}_4^{\rm r}$ and $\bar{q}_3^{\rm r}$ are approximately described by simple trigonometric functions:

$$\bar{q}_4^{\rm r} \approx A\cos(\omega_4 t), \tag{4.30}$$

$$\bar{q}_3^{\rm r} \approx A\cos(\omega_3 t). \tag{4.31}$$

Thus, the vibrations of the new and old NO bonds are

$$\begin{aligned}\delta r_1 \sim & \frac{q_4^{\rm r}+q_3^{\rm r}}{2^{1/2}} \approx 2^{-1/2}A\left[\cos(\omega_4 t)+\cos(\omega_3 t)\right] \\ = & 2^{1/2}A\cos\left(\frac{\omega_4-\omega_3}{2}t\right)\cos\left(\frac{\omega_4+\omega_3}{2}t\right), \end{aligned} \tag{4.32}$$

$$\begin{aligned}\delta r_2 \sim & \frac{q_4^{\rm r}-q_3^{\rm r}}{2^{1/2}} \approx 2^{-1/2}A\left[\cos(\omega_4 t)-\cos(\omega_3 t)\right] \\ = & 2^{1/2}A\sin\left(\frac{\omega_4-\omega_3}{2}t\right)\sin\left(\frac{\omega_4+\omega_3}{2}t\right). \end{aligned} \tag{4.33}$$

The interpretation of the right hand sides are that they are oscillating with the mean frequency $(\omega_4+\omega_3)/2$ while their amplitudes vary with $2^{1/2}A\cos(\omega_4-\omega_3)t/2$ and $2^{1/2}A\sin(\omega_4-\omega_3)t/2$. This change of amplitudes is called "beat" and the frequency $(\omega_4-\omega_3)/2$ is called the beat frequency. Note that initially ($t=0$) the amplitude of the new NO vibration is at its maximum value and that of the old NO vibration is zero. At the time τ which satisfies

$$\frac{\omega_4-\omega_3}{2}\tau = \frac{\pi}{4}, \tag{4.34}$$

the two NO bonds are oscillating with the same amplitudes. Therefore, the time scale for the excitation of the old NO bond can be estimated by

$$\tau = \frac{\pi}{2(\omega_4-\omega_3)}. \tag{4.35}$$

If we use the values shown in Fig. 4.4, it becomes

$$\tau = \frac{\pi}{2(234\ \mathrm{ps}^{-1}-166\ \mathrm{ps}^{-1})} \approx 23\ \mathrm{fs}, \tag{4.36}$$

which is of the same order as the residence time in the vicinity of the collinear saddle point, as we can see in Fig. 4.2(a)-(d). This means that the residence time near the collinear saddle is sufficient to allow the excitation of the old NO vibration. Here, the important point is that the energy transfer takes place very fast, since the period of the beat is short. Even though the lifetime of the reaction intermediate is very short compared to complex-mode reactions

which often involve intermediates of ps order lifetimes, the time scale of the beat is comparable to the lifetime of the reaction intermediate and thus causes a significant excitation of the old bond. The short time scale of the beat derives from the relatively large difference between the frequencies of the symmetric and antisymmetric stretches. Thus, we conclude that the origin of the old NO excitation is the preservation of the normal mode picture in spite of the high energy and the relatively large difference between the frequencies of the symmetric and antisymmetric stretches.

Note also that the regularity is not strictly required for the "beat" model. Even in the case of chaos, it is possible that the system sees vague tori[100,101] and follows a similar orbit to that of the normal mode picture for some short time period, whereas it traverses in a wider region of the phase space for a longer time period. The "beat" model can, then, be applied for the dynamics of the system in a short time range. The important aspect is the existence of two different mechanisms for the energy transfer. One is the randomization by strong chaos, where the system travels around in the potential well. This is close to the traditional picture of the energy transfer, that is, the randomization after a long lifetime in a deep well. The other mechanism is the motion of the distorted normal mode type, where the system experiences only a part of the phase space but the motion is represented as a superposition of a few distorted normal modes. If the periods of the beats are short enough, efficient energy transfer takes place. In particular, this mechanism works not only in the well but also near the saddle. The present work shows the importance of the latter by showing that the "beat" mechanism explains the efficient energy exchange of the reaction of $O(^1D) + N_2O \rightarrow NO + NO$.

4.4 SUMMARY AND OUTLOOK

The dynamics of the short lifetime trajectories with near-collinear approach, which have been named "Path 1," of the reaction $O(^1D) + N_2O \rightarrow NO + NO$ was investigated for zero total angular momentum. This reaction was found to exhibit a significant energy transfer from the new to the old NO vibration in spite of its short lifetime.[18] To clarify the origin of this efficient energy exchange, analyses of the Path 1 trajectories were performed by using the normal form (NF) theory. First we performed fourth-order Taylor expansion of the potential energy around the collinear saddle point. By examining the time evolution of the Jacobi coordinates and the error of the expansion, we showed that a significant proportion of the trajectories came close to the saddle and that the excitation of the old NO vibration began in the vicinity of the saddle. We performed a coordinate transformation to PNF coordinates. In these coordinates, the

number of the coupling terms in Hamiltonian decreased drastically compared to the original coordinates, which simplified the analysis. By examining the remaining coupling terms, we found that the reactive mode was completely separable from the other modes. Moreover, the symmetric and antisymmetric stretching modes, which include the vibrations of the new and old NO bonds, were strongly coupled to each other, whereas the other two modes were only weakly coupled to these modes. Therefore we reduced the essence of the dynamics into the 2-DOF system consisting of the two stretching modes of the NO bonds.

Analyses of the 2-DOF subsystem revealed a distorted normal mode picture, which is topologically the same as the normal mode, in spite of their high energy above the saddle point. This offered the basic mechanism of the efficient energy transfer as a "beat" between the symmetric and the antisymmetric stretching modes. The period of the beat was of the order of 10 fs, due to the large difference between the frequencies of the symmetric and the antisymmetric stretching modes. Comparison of the period to the residence time near the collinear saddle revealed that the time scale of the beat was short enough to cause excitation of the old NO vibration. Thus we concluded that the origin of the efficient energy transfer from the new to the old NO vibration is the distorted normal mode structure and the large difference between the frequencies of the symmetric and the antisymmetric stretching modes.

The extraction of the essence of the efficient energy transfer was made possible by the power of the NF calculations. The NF calculations enable us to elucidate the coupling terms essential to the dynamics by making the Hamiltonian as simple as possible. For our system, a fourth-order polynomial with 10 variables has 1001 terms, whereas the number of the remaining couplings after the NF calculations are only 12 as is listed in Table 4.1. With the number of terms drastically reduced to 12 from 1001, we assessed which couplings play important roles in the dynamics by plotting the value of each term as in Fig. 4.6. Thus we succeeded in showing that the dynamics of this system is regular with the distorted normal mode structure well conserved.

Our PNF method[55] presented here is generally applicable to any systems of many degrees of freedom and provides us with an essential clue of the underlying geometrical structure of the multidimensional phase space. For example, chemical reactions; $O(^1D) + HCl$ [52–54], $O(^1D) + H_2O$ [30,31], and $H + NO_2$ [49–51], are also quite interesting systems because the PES have deep wells but the product state distributions deviate significantly from the statistical distributions. These require systematic scrutiny of the phase space in the region of potential well. Our dimension reduction by PNF will be of great help to capture the phase space properties of any stationary point. To be sure, it depends on the system to what extent we can

reduce the dimension of the system. Poincaré surface of section is a powerful tool only for the cases where the system can be reduced to a two-DOF system. However, even if the system can only be reduced to an $m(\geq 3)$-DOF system, this makes the analyses much simpler than the original $n(> m)$-DOF system. Moreover, it is a significant information by itself which modes are separated and which modes are strongly coupled to the other modes. This reveals a nonuniform character of the phase space highly contrasted to a simple statistical description where all the DOF are completely mixed. Thus, our PNF method is expected to capture the dynamical structure of the system and thereby shed light on the origin of complicated behavior in chemical reaction dynamics.

4.5 APPENDIX A: Derivation of the Hamiltonian (4.6)

Here we present the derivation of the Hamiltonian (4.6) starting from Eq. (4.2). First we introduce the polar coordinates for each Jacobi vector:

$$x_\ell = r_\ell \cos\phi_\ell, \tag{4.37}$$

$$y_\ell = r_\ell \sin\phi_\ell, \tag{4.38}$$

for $\ell = 0, 1, 2$. Then the Hamiltonian is expressed as

$$H = \sum_{\ell=0}^{2} \frac{1}{2m_\ell}\left({p_{r_\ell}}^2 + \frac{{p_{\phi_\ell}}^2}{{r_\ell}^2} \right) + V. \tag{4.39}$$

The Jacobi angles χ_1, χ_2 can be introduced by the following transformations:

$$\chi_1 = \phi_1 - \phi_0, \tag{4.40}$$

$$\chi_2 = \phi_2 - \phi_0, \tag{4.41}$$

$$\Theta = \phi_0. \tag{4.42}$$

To make the transformation canonical, the conjugate momenta to (χ_1, χ_2, Θ) are given as follows:

$$p_{\chi_1} = p_{\phi_1}, \tag{4.43}$$

$$p_{\chi_2} = p_{\phi_2}, \tag{4.44}$$

$$J = p_{\phi_0} + p_{\phi_1} + p_{\phi_2}, \tag{4.45}$$

where J is the conjugate momentum of Θ and has the physical meaning of the total angular momentum of the system. When we put these equations into Eq. (4.39), we obtain

$$H = \frac{1}{2m_0} {p_{r_0}}^2 + \sum_{\ell=1}^{2} \left[\frac{1}{2m_\ell} {p_{r_\ell}}^2 + \frac{1}{2m_\ell {r_\ell}^2} {p_{\chi_\ell}}^2 \right] + \frac{1}{2m_0 {r_0}^2} \left(J - p_{\chi_1} - p_{\chi_2} \right)^2 + V. \tag{4.46}$$

Here we make an important observation that the kinetic part of the Hamiltonian (4.46) does not contain Θ. Moreover, the potential energy V depends only on the internal coordinates $(r_0, r_1, r_2, \chi_1, \chi_2)$ and not on Θ. Therefore the time derivative of J is

$$\frac{d}{dt} J = -\frac{\partial H}{\partial \Theta} = 0, \tag{4.47}$$

which means the conservation of the total angular momentum. Thus we can regard the system as an effective 5-DOF system with five position coordinates $(r_0, r_1, r_2, \chi_1, \chi_2)$ and the Hamiltonian (4.46) with J being treated as a constant parameter. In the meantime, the time evolution of Θ is given by

$$\frac{d}{dt} \Theta = \frac{\partial H}{\partial J} = \frac{1}{m_0 {r_0}^2} \left(J - p_{\chi_1} - p_{\chi_2} \right). \tag{4.48}$$

The appearance of the internal coordinates such as p_{χ_1} in the equation of $\dfrac{d}{dt}\Theta$ is a consequence of the so-called "falling cat problem,"[102–104] that is, the system can rotate under the effect of the internal motion. In contrast, the effect of the rotational motion on the internal motion is only through constant J as seen in Eq. (4.46). Since the rotational motion is not our principal interest in this chapter, we treat the internal motion as a 5-DOF system given by Eq. (4.46). Substituting $J = 0$ into Eq. (4.46) yields Eq. (4.6).

4.6 APPENDIX B: Construction of the NF transformation

Here we describe briefly the construction of the NF transformation from the original (normal mode) coordinates $(\boldsymbol{q}^{\mathrm{c}}, \boldsymbol{p}^{\mathrm{c}})$ to the NF coordinates $(\bar{\boldsymbol{q}}^{\mathrm{c}}, \bar{\boldsymbol{p}}^{\mathrm{c}})$. We follow the formulation by Dragt and Finn.[105] We start by writing the Hamiltonian in a power series of a small parameter σ,

$$H(\boldsymbol{q}^{\mathrm{c}}, \boldsymbol{p}^{\mathrm{c}}, \sigma) = \sum_{n=0}^{\infty} \sigma^n H_n^{(0)}(\boldsymbol{q}^{\mathrm{c}}, \boldsymbol{p}^{\mathrm{c}}), \tag{4.49}$$

where $H_0^{(0)}$ is the harmonic part of the Hamiltonian [see Eq. (4.13)]:

$$H_0^{(0)}(\boldsymbol{q}^{\mathrm{c}}, \boldsymbol{p}^{\mathrm{c}}) = \lambda q_1^{\mathrm{c}} p_1^{\mathrm{c}} + \sum_{\ell=2}^{5} \mathrm{i}\omega_\ell q_\ell^{\mathrm{c}} p_\ell^{\mathrm{c}}. \tag{4.50}$$

To introduce a small parameter, we scale the coordinates $(\boldsymbol{q}^{\mathrm{c}}, \boldsymbol{p}^{\mathrm{c}}) \mapsto (\sigma\boldsymbol{q}^{\mathrm{c}}, \sigma\boldsymbol{p}^{\mathrm{c}})$ and $H \mapsto \sigma^{-2}H$. After the transformation is constructed, the parameter σ is set equal to 1. The canonical transformation $(\boldsymbol{q}^{\mathrm{c}}, \boldsymbol{p}^{\mathrm{c}}) \mapsto (\bar{\boldsymbol{q}}^{\mathrm{c}}, \bar{\boldsymbol{p}}^{\mathrm{c}})$ is constructed by successive operations of Lie transformations:

$$\bar{q}_\ell = \exp(-\sigma F_1)\exp(-\sigma^2 F_2)\cdots\exp(-\sigma^N F_N) q_\ell, \tag{4.51}$$

$$\bar{p}_\ell = \exp(-\sigma F_1)\exp(-\sigma^2 F_2)\cdots\exp(-\sigma^N F_N) p_\ell, \tag{4.52}$$

where N is the order of the perturbation and F_n $(n = 1, \ldots, N)$ is an operation of Poisson bracket with a function f_n:

$$F_n = \{\cdot, f_n\}. \tag{4.53}$$

Then, the transformation of the Hamiltonian $H(\boldsymbol{q}^{\mathrm{c}}, \boldsymbol{p}^{\mathrm{c}}, \sigma) \mapsto \bar{H}(\bar{\boldsymbol{q}}^{\mathrm{c}}, \bar{\boldsymbol{p}}^{\mathrm{c}}, \sigma)$ is given by

$$\bar{H} = \exp(\sigma^N F_N)\cdots\exp(\sigma^2 F_2)\exp(\sigma F_1) H. \tag{4.54}$$

If we define $\bar{H}^{(m)}(\bar{\boldsymbol{q}}^{\mathrm{c}}, \bar{\boldsymbol{p}}^{\mathrm{c}}, \sigma)$ and $\bar{H}_n^{(m)}(\bar{\boldsymbol{q}}^{\mathrm{c}}, \bar{\boldsymbol{p}}^{\mathrm{c}})$ by

$$\begin{aligned}\bar{H}^{(m)} &= \exp(\sigma^m F_m)\bar{H}^{(m-1)} \\ &= \exp(\sigma^m F_m)\cdots\exp(\sigma^2 F_2)\exp(\sigma F_1) H, \end{aligned}\tag{4.55}$$

$$\bar{H}^{(m)} = \sum_{n=0}^{\infty} \sigma^n \bar{H}_n^{(m)}, \tag{4.56}$$

we can readily obtain the following recursion formulae for $\bar{H}_n^{(m)}$

$$n < m \ : \ \bar{H}_n^{(m)} = \bar{H}_n^{(m-1)} \tag{4.57}$$

$$n = m \ : \ \bar{H}_m^{(m)} = \bar{H}_m^{(m-1)} + F_m \bar{H}_0^{(0)} \tag{4.58}$$

$$n > m \ : \ \bar{H}_n^{(m)} = \bar{H}_n^{(m-1)} + \sum_{s=1}^{\infty} \frac{(F_m)^s}{s!} \bar{H}_{n-sm}^{(m-1)}. \tag{4.59}$$

In the final Hamiltonian $\bar{H} = \bar{H}^{(N)} = \sum_{n=0}^{\infty} \sigma^n \bar{H}_n^{(N)}$, the terms of the order n is

$$\bar{H}_n^{(N)} = \bar{H}_n^{(N-1)} = \cdots = \bar{H}_n^{(n)} = \bar{H}_n^{(n-1)} + F_n \bar{H}_0^{(0)}, \tag{4.60}$$

because of Eqs. (4.57) and (4.58). Thus, F_n can be determined so that the function $\bar{H}_n^{(N)}$ has a "desired" form.

In the present case, $\bar{H}_n^{(n-1)}$ is expressed in the form of a polynomial:

$$\bar{H}_n^{(n-1)}(\boldsymbol{q}^{\mathrm{c}}, \boldsymbol{p}^{\mathrm{c}}) = \sum_{\sum_\ell (j_\ell + k_\ell) = n+2} \alpha_{\boldsymbol{jk}}^{(n)} \prod_{\ell=1}^{5} (q_\ell^{\mathrm{c}})^{j_\ell} \, (p_\ell^{\mathrm{c}})^{k_\ell} \,, \tag{4.61}$$

where $\alpha_{\boldsymbol{jk}}^{(n)}$ is the coefficient of the polynomial. Moreover, $F_n \bar{H}_0^{(0)} = \left\{ \bar{H}_0^{(0)}, f_n \right\}$ and $\bar{H}_0^{(0)} = H_0^{(0)}$ has the form of Eq. (4.50). Therefore, if we are to eliminate the terms with certain values of $(\boldsymbol{j}, \boldsymbol{k})$ from the final Hamiltonian $\bar{H}$, we set

$$f_n = \sum_{(\boldsymbol{j}, \boldsymbol{k})} \frac{\alpha_{\boldsymbol{jk}}}{\gamma_{\boldsymbol{jk}}} \prod_{\ell=1}^{5} (q_\ell^{\mathrm{c}})^{j_\ell} \, (p_\ell^{\mathrm{c}})^{k_\ell} \,, \tag{4.62}$$

where the divisor $\gamma_{\boldsymbol{jk}}$ is defined as follows:

$$\gamma_{\boldsymbol{jk}} = \lambda(j_1 - k_1) + \mathrm{i} \sum_\ell \omega_\ell (j_\ell - k_\ell). \tag{4.63}$$

To obtain a well-defined transformation, the range of the summation in Eq. (4.62) is determined so that the polynomial series converges. If we have $\gamma_{\boldsymbol{jk}} \approx 0$ for certain combinations of $(\boldsymbol{j}, \boldsymbol{k})$, then the corresponding coefficients of Eq. (4.62) take large values and cause divergence of the series. This is the notorious problem of small divisors.[106] This situation arises when the bath mode frequencies $\omega_2, \ldots, \omega_5$ are nearly in the ratio of integers and called the "resonance" effect. Such values of $(\boldsymbol{j}, \boldsymbol{k})$ cannot be included in the summation of Eq. (4.62) and therefore have to be kept in $\bar{H}$. In this chapter we investigate which values of $(\boldsymbol{j}, \boldsymbol{k})$ can or cannot be eliminated from $\bar{H}$, by checking the energy error as described in Sec. 4.2.3. After that process we obtain the results shown in Eq. (4.23) and Table 4.1.

Acknowledgements

The present thesis is a collection of the author's studies which have been carried out under the direction of Professor Okitsugu Kajimoto and Professor Yo Fujimura in Kyoto University during 1999-2005. The author wishes to express his sincere gratitude to Professor Okitsugu Kajimoto for his continuing guidance and generous support. The author's deepest gratitude is also to Professor Yo Fujimura for his kind and thorough instruction throughout this thesis.

The author also wishes to thank Professor Toshiyuki Takayanagi for providing his PES.[27–29] The collaboration with him was inevitable for all the calculational parts of this thesis. The author also appreciates Dr. Takefumi Yamashita for his large contribution in constructing our new PES and all the analyses made on it. His large help was also essential for this thesis. The author is also grateful to Professor Laurent Bonnet for his discussion on the results in Chapter 2 of this thesis.

The author also wishes to thank Dr. Koji Hotta who provided the opportunity to study the NF theory. The author is also grateful to Professor Tamiki Komatsuzaki for teaching him the NF theory and also for his continuing discussion and instructive comments on the study in Chapter 4 of this thesis. The author also wishes to express his sincere gratitude for Professor Mikito Toda and Dr. Chun-Biu Li for their instructive comments and collaborations concerning the NF theory. The author's gratitude is also to all the other members of Professor Komatsuzaki's and Professor Toda's laboratories for their helpful discussions. The author also wishes to express his deepest gratitude to Professor Turgay Uzer and Professor Charles Jaffé for their valuable instruction. The collaboration with them in Refs. 44 and 45 provided the author with large amount of knowledge and experiences in the NF theory. The author is also grateful to Professor Jesús Palacián and Professor Patricia Yanguas. The collaboration with them in Ref. 44 also provided the author with the knowledge of the NF theory.

The author also wishes to express his gratitude to Professor Hiroshi Tsurumaki and Dr. Hiroshi Akagi, whose support and advice as the author's predecessor were of great help throughout the research. The author is also grateful to Professor Yasuhiro Ohshima, Professor Kimihiko Hara and Professor Yosuke Yoshimura for their instructive discussions and encouragements.

The author also wishes to thank Mr. Hisashi Tamada and Mr. Yoshiyuki Imai for their great support throughout the research. Furthermore, the author's gratitude is to all the former and present members of the laboratory of physical chemistry in Kyoto University.

Finally, the author wishes to thank Hiroyuki and Kyoko Kawai, his parents, and Yui Kawai, his sister, for their support both in financial and mental aspects during ten years of his college life.

Bibliography

[1] F. Copleston, *A History of Philosophy, vol. I: Greece and Rome*, Bantam Doubleday Dell Publishing Group, New York (1962).

[2] L. I. Schiff, *Quantum Mechanics*, McGraw-Hill, New York (1968).

[3] H. Goldstein, *Classical Mechanics*, Addison-Wesley, Reading, MA (1980).

[4] S. A. Harich, D. Dai, C. C. Wang, X. Yang, S. D. Chao, and R. T. Skodje, *Nature*, **419**, 281 (2002).

[5] S. D. Chao, S. A. Harich, D. X. Dai, C. C. Wang, X. Yang, and R. T. Skodje, *J. Chem. Phys.*, **117**, 8341 (2002).

[6] R. D. Levine and R. B. Bernstein, *Molecular Reaction Dynamics and Chemical Reactivity*, Oxford University Press, New York (1987).

[7] J. I. Steinfeld, J. S. Francisco, and W. L. Hase, *Chemical Kinetics and Dynamics*, Prentice-Hall, New Jersey (1989).

[8] J. C. Polanyi, *Acc. Chem. Res.*, **5**, 161 (1972).

[9] S. Sato, *Bull. Chem. Soc. Japan*, **28**, 450 (1955).

[10] J. Wolfrum, *Ber. Bunsenges. physik. Chem.*, **81**, 114 (1977).

[11] B. A. Thrush, *Acc. Chem. Res.*, **14**, 116 (1981).

[12] J. R. Wiesenfeld, *Acc. Chem. Res.*, **15**, 110 (1982).

[13] K. Honma, Y. Fujimura, O. Kajimoto, and G. Inoue, *J. Chem. Phys.*, **88**, 4739 (1988).

[14] M. Brouard, S. P. Duxon, P. A. Enriquez, R. Sayos, and J. P. Simons, *J. Phys. Chem.*, **95**, 8169 (1991).

[15] M. Brouard, S. P. Duxon, P. A. Enriquez, and J. P. Simons, *J. Chem. Phys.*, **97**, 7414 (1992).

[16] X. Wang, H. Li, Q. Zhu, F. Kong, and H. Yu, *J. Chin. Chem. Soc.*, **42**, 399 (1995).

[17] H. Akagi, Y. Fujimura, and O. Kajimoto, *J. Chem. Soc., Faraday Trans.*, **94**, 1575 (1998).

[18] H. Akagi, Y. Fujimura, and O. Kajimoto, *J. Chem. Phys.*, **111**, 115 (1999).

[19] H. Tsurumaki, Y. Fujimura, and O. Kajimoto, *J. Chem. Phys.*, **111**, 592 (1999).

[20] P. J. Pisano, M. S. Westley, and P. L. Houston, *Chem. Phys. Lett.*, **318**, 385 (2000).

[21] G. Hancock and V. Haverd, *Phys. Chem. Chem. Phys.*, **5**, 2369 (2003).

[22] S. Kawai, Y. Fujimura, O. Kajimoto, and T. Takayanagi, *J. Chem. Phys.*, **120**, 6430 (2004).

[23] J. R. Hetzler, M. P. Casassa, and D. S. King, *J. Phys. Chem.*, **95**, 8086 (1991).

[24] E. A. Wade, J. I. Cline, K. T. Lorenz, C. Hayden, and D. W. Chandler, *J. Chem. Phys.*, **116**, 4755 (2002).

[25] I. Last, A. Aguilar, R. Sayós, M. González, and M. Gilibert, *J. Phys. Chem. A*, **101**, 1206 (1997).

[26] M. González, R. Valero, J. M. Anglada, and R. Sayós, *J. Chem. Phys.*, **115**, 7015 (2001).

[27] H. Akagi, A. Yokoyama, Y. Fujimura, and T. Takayanagi, *Chem. Phys. Lett.*, **324**, 423 (2000).

[28] T. Takayanagi and A. Wada, *Chem. Phys.*, **269**, 37 (2001).

[29] T. Takayanagi and H. Akagi, *Chem. Phys. Lett.*, **363**, 298 (2002).

[30] C. B. Cleveland and J. R. Wiesenfeld, *J. Chem. Phys.*, **96**, 248 (1992).

[31] D. G. Sauder, J. C. Stephenson, D. S. King, and M. P. Casassa, *J. Chem. Phys.*, **97**, 952 (1992).

[32] R. Sayós, C. Oliva, and M. González, *J. Chem. Phys.*, **113**, 6736 (2000).

[33] N. Goledstein, G. D. Greenblatt, and J. R. Wiesenfeld, *Chem. Phys. Lett.*, **96**, 410 (1983).

[34] T. Takayanagi, *Chem. Phys.*, **211**, 308 (2005).

[35] S. Kawai, Y. Fujimura, O. Kajimoto, and T. Yamashita, *J. Chem. Phys.*, **124**, 184315 (2006).

[36] T. Komatsuzaki and R. S. Berry, *J. Chem. Phys.*, **110**, 9160 (1999).

[37] T. Komatsuzaki and R. S. Berry, *Phys. Chem. Chem. Phys.*, **1**, 1387 (1999).

[38] T. Komatsuzaki and R. S. Berry, *J. Mol. Struct. (Theochem)*, **506**, 55 (2000).

[39] T. Komatsuzaki and R. S. Berry, *Proc. Nat. Acad. Sci. USA*, **98**, 7666 (2001).

[40] T. Komatsuzaki and R. S. Berry, *J. Chem. Phys.*, **115**, 4105 (2001).

[41] T. Komatsuzaki and R. S. Berry, *J. Phys. Chem. A*, **106**, 10945 (2002).

[42] T. Komatsuzaki and R. S. Berry, *Adv. Chem. Phys.*, **123**, 79 (2002).

[43] T. Uzer, C. Jaffé, J. Palacian, P. Yanguas, and S. Wiggins, *Nonlinearity*, **15**, 957 (2002).

[44] C. Jaffé, S. Kawai, J. Palacián, P. Yanguas, and T. Uzer, *Adv. Chem. Phys.*, **130**, 171 (2005).

[45] S. Kawai, C. Jaffé, and T. Uzer, *J. Phys. B: At. Mol. Opt. Phys.*, **38**, S261 (2005).

[46] C.-B. Li, Y. Matsunaga, M. Toda, and T. Komatsuzaki, *J. Chem. Phys.*, **123**, 184301 (2005).

[47] C.-B. Li, A. Shojiguchi, M. Toda, and T. Komatsuzaki, *Few-Body Systems*, **38**, 173 (2006).

[48] A. Deprit, *Cel. Mech.*, **1**, 12 (1969).

[49] D. G. Sauder and P. J. Dagdigian, *J. Chem. Phys.*, **92**, 2389 (1990).

[50] A. M. L. Irvine, I. W. M. Smith, R. P. Tuckett, and X.-F. Yang, *J. Chem. Phys.*, **93**, 3177 (1990).

[51] A. M. L. Irvine, I. W. M. Smith, and R. P. Tuckett, *J. Chem. Phys.*, **93**, 3187 (1990).

[52] A. C. Luntz, *J. Chem. Phys.*, **73**, 5393 (1980).

[53] E. J. Kruus, B. I. Niefer, and J. J. Sloan, *J. Chem. Phys.*, **88**, 985 (1987).

[54] C. R. Park and J. R. Wiesenfeld, *Chem. Phys. Lett.*, **163**, 230 (1989).

[55] S. Kawai, Y. Fujimura, O. Kajimoto, T. Yamashita, C.-B. Li, T. Komatsuzaki, and M.Toda, *Phys. Rev. A*, **75**, 022714 (2007).

[56] D. L. Baulch, R. A. Cox, R. F. Hampson, Jr., J. A. Kerr, J. Troe, and R. T. Watson, *J. Phys. Chem. Ref. Data*, **9**, 295 (1980).

[57] R. Atkinson, D. L. Baulch, R. A. Cox, R. F. Hampson, Jr., J. A. Kerr, and J. Troe, *J. Phys. Chem. Ref. Data*, **21**, 1125 (1992).

[58] H. Akagi, Y. Fujimura, and O. Kajimoto, *J. Chem. Phys.*, **110**, 7264 (1999).

[59] S. F. Adams, C. A. DeJoseph, Jr., C. C. Carter, T. A. Miller, and J. M. Williamson, *J. Phys. Chem. A*, **105**, 5977 (2001).

[60] G. D. Greenblatt and A. R. Ravishankara, *J. Geophys. Res.*, **95**, 3539 (1990).

[61] J. Luque and D. R. Crosley, *J. Chem. Phys.*, **112**, 9411 (2000).

[62] W. H. Press, S. A. Teukolsky, W. T. Vetterling, and B. P. Flannery, *Numerical Recipes in C*, Cambridge University Press, Cambridge (1992).

[63] A. R. W. McKellar, J. K. G. Watson, and B. J. Howard, *Mol. Phys.*, **86**, 273 (1995).

[64] Y. Fujimura, H. Tsurumaki, and O. Kajimoto, *Bull. Chem. Soc. Jpn.*, **75**, 2309 (2002).

[65] P. Felder, B.-M. Haas, and J. R. Huber, *Chem. Phys. Lett.*, **186**, 177 (1991).

[66] J. Danielak, U. Domin, R. Kępa, M. Rytel, and M. Zachwieja, *J. Mol. Spectrosc.*, **181**, 394 (1997).

[67] R. Altkorn and R. N. Zare, *Annu. Rev. Phys. Chem.*, **35**, 265 (1984).

[68] J. Luque and D. R. Crosley, *J. Chem. Phys.*, **111**, 7405 (1999).

[69] M. Islam, I. W. M. Smith, and J. W. Wiebrecht, *J. Phys. Chem.*, **98**, 9285 (1994).

[70] P. Pechukas and J. C. Light, *J. Chem. Phys.*, **42**, 3281 (1965).

[71] J. C. Light, *Disc. Faraday Soc.*, **44**, 14 (1967).

[72] M. Quack and J. Troe, *Ber. Bunsenges. Phys. Chem.*, **78**, 240 (1974).

[73] T. M. Ticich, T. R. Rizzo, H.-R. Dübal, and F. F. Crim, *J. Chem. Phys.*, **84**, 1508 (1986).

[74] P. Larregaray, L. Bonnet, and J. C. Rayez, *J. Chem. Phys.*, **114**, 3349 (2001).

[75] MOLPRO is a package of *ab initio* programs written by H.-J Werner and P. Knowles with contributions from J. Almlöf, R. D. Amos, A. Berning, L. D. Cooper, M. J. O. Deegan, A. J. Dobbyn, F. Eckert, S. T. Elbert, C. Hampel, R. Lindh, A. W. Lloyd, W. Meyer, A. Nicklass, K. Peterson, R. Pitzer, A. J. Stone, P. R. Taylor, M. E. Mura, P. Pulay, M. Schütz, H. Stoll, and T. Thorsteinsson.

[76] J. Ischtwan and M. A. Collins, *J. Chem. Phys.*, **100**, 8080 (1994).

[77] J. F. Castillo, M. A. Collins, F. J. Aoiz, and L. Bañares, *J. Chem. Phys.*, **118**, 7303 (2003).

[78] T. Ishida and G. C. Schatz, *Chem. Phys. Lett.*, **314**, 369 (1999).

[79] W. Eisfeld and K. Morokuma, *J. Chem. Phys.*, **113**, 5587 (2000).

[80] M. A. Vincent, I. H. Hillier, and L. Salsi, *Phys. Chem. Chem. Phys.*, **2**, 707 (2000).

[81] L. Krim and N. Lacome, *J. Phys. Chem. A*, **102**, 2289 (1998).

[82] T. Martínez, M. L. Hernández, J. M. Alvariño, F. J. Aoiz, and V. Sáez Rábanos, *J. Chem. Phys.*, **119**, 7871 (2003).

[83] C. Jaffé and P. Brumer, *J. Chem. Phys.*, **73**, 5646 (1980).

[84] E. L. Sibert III, W. P. Reinhardt, and J. T. Hynes, *J. Chem. Phys.*, **77**, 3583 (1982).

[85] E. L. Sibert III, J. T. Hynes, and W. P. Reinhardt, *J. Chem. Phys.*, **77**, 3595 (1982).

[86] M. S. Child and L. Halonen, *Adv. Chem. Phys.*, **57**, 1 (1984).

[87] L. Xiao and M. E. Kellman, *J. Chem. Phys.*, **93**, 5805 (1990).

[88] J. P. Rose and M. E. Kellman, *J. Chem. Phys.*, **105**, 10743 (1996).

[89] Z.-M. Lu and M. E. Kellman, *J. Chem. Phys.*, **107**, 1 (1997).

[90] J. Weiß, J. Hauschildt, S. Yu. Grebenshchikov, R. Düren, R. Schinke, J. Koput, S. Stamatiadis, and S. C. Farantos, *J. Chem. Phys.*, **112**, 77 (2000).

[91] M. Joyeux, D. Sugny, M. Lombardi, R. Jost, R. Schinke, S. Skokov, and J. Bowman, *J. Chem. Phys.*, **113**, 9610 (2000).

[92] T. Yamashita and S. Kato, *J. Chem. Phys.*, **119**, 4251 (2003).

[93] T. Komatsuzaki and R. S. Berry, *Adv. Chem. Phys.*, **130**, 143 (2005).

[94] C.-B. Li, A. Shojiguchi, M. Toda, and T. Komatsuzaki, *Phys. Rev. Lett.*, **97**, 028302 (2006).

[95] M. Toda, T. Komatsuzaki, T. Konishi, R.S. Berry, and S.A. Rice, eds., *Geometrical Structures of Phase Space in Multidimensional Chaos: Applications to Chemical Reaction Dynamics in Complex Systems* Adv. Chem. Phys. **130A,130B** (2005) and references therein.

[96] S. Wiggins, *Normally Hyperbolic Invariant Manifolds in Dynamical Systems*, Springer-Verlag, New York (1991).

[97] R. D. Levine, *Molecular Reaction Dynamics*, Cambridge Univ. Press, New York (2005).

[98] H. Waalkens, A. Burbanks, and S. Wiggins, *J. Chem. Phys.*, **121**, 6207 (2004).

[99] J. Moser, *Comm. Pure Appl. Math.*, **11**, 257 (1958).

[100] R. B. Shirts and W. P. Reinhardt, *J. Chem. Phys.*, **77**, 5204 (1982).

[101] R. B. Shirts and W. P. Reinhardt, *J. Chem. Phys.*, **79**, 3173 (1983).

[102] A. Guichardet, *Ann. Inst. Henri Poincaré*, **40**, 329 (1984).

[103] R. G. Littlejohn and M. Reinsch, *Rev. Mod. Phys.*, **69**, 1 (1997).

[104] T. Yanao and K. Takatsuka, *Phys. Rev. A*, **68**, 032714 (2003).

[105] A. J. Dragt and J. M. Finn, *J. Math. Phys.*, **20**, 2649 (1979).

[106] V. I. Arnol'd, V. V. Kozlov, and A. I. Neishtadt, *Mathematical Aspects of Classical and Celestial Mechanics*, Springer-Verlag, New York (1988).